# A Study of the Electromagnetic Properties of the Dielectric Wall Accelerator

By

Adam J. Uselmann

A dissertation submitted in partial fulfillment of
the requirements for the degree of

Doctor of Philosophy
(Medical Physics)

at the
UNIVERSITY OF WISCONSIN-MADISON
2015

Date of final oral examination: 12/19/14

The dissertation is approved by the following members of the Final Oral Committee:
Thomas R. Mackie, Professor Emeritus, Medical Physics
Paul M. Deluca, Jr., Professor Emeritus, Medical Physics
Bhudatt R. Paliwal, Professor, Medical Physics
Michael W. Kissick, Assistant Professor, Medical Physics
Douglass L. Henderson, Professor, Engineering Physics

# Contents

# List of Figures

# List of Tables

# Acknowledgments

I would first like to thank my advisor, Professor Rock Mackie. The insight, support, encouragement, and innovative spirit you've offered have been a huge inspiration throughout my studies, and I look forward to what future collaborations will bring. I would also like to thank my committee, Professor Paul M. DeLuca, Jr., Professor Bhudatt Paliwal, Professor Douglass Henderson, and Professor Michael Kissick, for the opportunities, input, and advice that have been immensely valuable to me during my time as a student.

Thank you to Kevin Eliceiri, Bruce Thomadsen, and all of the other faculty members I've had the pleasure of learning from and collaborating with, for encouraging me to push forward my career as a researcher.

Thank you to Myles Sommerfeldt, Ed Neumeuller, Dan Schmidt, and everyone at Standard Imaging, Inc., for the opportunities, experience, and learning that resulted from my time working there as a student.

Thank you to all of the friends and colleagues I've made through my work here: Tye Gribb, for the Terrace chats that were a welcome break from thesis writing; Dave Westerly, for the wonderful opportunity to visit Colorado and for the incredibly useful discussions about the Dielectric Wall Accelerator; Charlie Wallace, Kara Hulce, Liz Zakszewski, and Bill Andrews, for the trivia, board games, and cookouts that have always been a great time; and Andreas Velten, Ben Cox, Surendra Prajapati, Gary Stange, Alexandra Schroeder, Brandon Walker, George Petry, and everyone in the Morgridge Institute for Research Medical Engineering group, for the companionship, help on projects, laughter, Library excursions,

blimp flights, cook-offs, side projects, and great conversations that made coming into work each day an adventure.

Thank you to my parents, grandparents, sisters, and extended family. Mom, your love and support have meant the world to me, and I couldn't have done this without you. Dad, you inspired my pursuit of science, technology, and medicine. I think of your love and sense of humor daily, and I wish you could be here today.

Finally, thank you to all of my friends outside of my work experience: Mark Chiarulli and Abby McGraw, Matthew and Wendy Franczak, and Chris Zimmerman, for the unwavering friendship, moral support, and hospitality; Chris Joutras, Nate Karls, Jamie Mclees, and all of the fine people I've met through playing music in Madison; and, last but not least, Ally Miller, for the companionship, understanding, encouragement, and laughter that have been absolutely crucial to completing this endeavor.

# Abstract

Proton and heavy-ion radiotherapy are powerful tools in cancer treatment, yet access to these modalities has been limited due to the large size and costs of the accelerators used and the facilities to house them. The dielectric wall accelerator (DWA) is a type of compact particle accelerator that can potentially bring proton and heavy ion therapy into more widespread clinical use at a significantly lower cost than existing devices. However, the technology pushes the limits of current materials and electronics, making the maximization of the efficiency of the design absolutely crucial. In this work, an investigation of the critical parameters of the device was performed using electromagnetic simulation and particle tracking tools, and novel geometric variations of the device were investigated in order to improve performance.

# Chapter 1

# Introduction

## 1.1 Proton Radiotherapy Overview and History

Proton radiotherapy was first proposed by Robert R. Wilson in 1946 [13], and the first treatment was carried out at Lawrence Berkeley Laboratory in 1954 [14]. Protons deliver the majority of their energy at the end of their range in what is known as the "Bragg peak", after which the dose drops off rapidly with depth. This is in contrast to photons, which deliver their maximum dose at a relatively shallow depth that drops off approximately exponentially with depth, providing significant dose beyond the depth of the target volume (Figure 1.1). These physical advantages of protons lead to more conformal dose distributions in many cases, which may allow for reduced normal tissue complications or maintaining similar normal tissue complication probability (NTCP) while delivering a higher target dose. The potentially high precision of proton dose distributions allows for the application of clinical techniques such as dose painting, where sub-volumes of the target are given additional dose [15].

Tumor coverage is achieved by modulating the range of the protons to create a spread-out Bragg peak (SOBP). This can be achieved by placing material of varying thickness within the beam (such as a modulator wheel), which can cause some slight defocusing and additional neutron dose, or by actively modulating the energy of the beam [14].

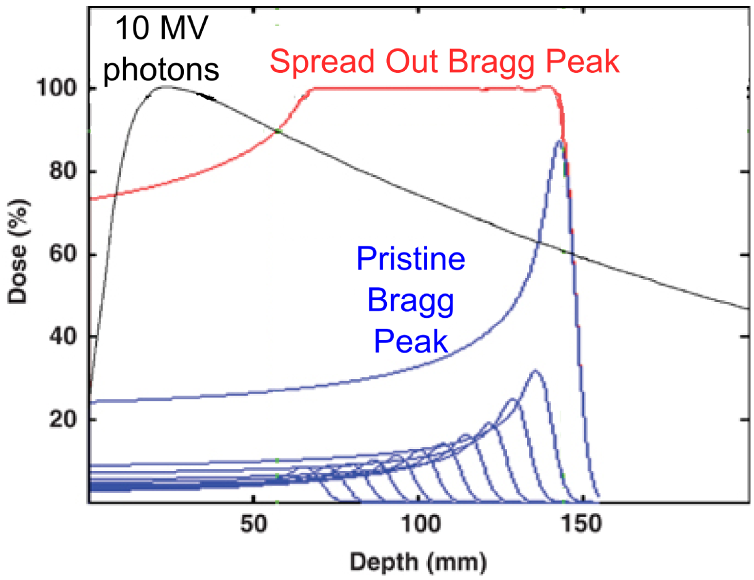

Figure 1.1: A comparison of the depth-dose curves of photons, protons, and the spread-out Bragg peak (SOBP) of protons. Image modified from Levin, 2005 [1].

Proton beam delivery is improved through the use of pencil beam scanning, in which a narrow beam of protons is scanned over the target volume to provide tumor coverage [16]. Scanning methods reduce secondary neutron dose to non-target regions by a factor of ten as compared to scattering methods [17]. Energy modulated pencil beams allow for delivery of highly conformal intensity modulated proton therapy (IMPT) [18] through methods such as three-dimensional intensity modulation [19], distal edge tracking [20], and distal gradient tracking [21]. The reduction in dose to healthy tissue through using these methods allows for significant escalation in tumor dose [22, 23, 24].

According to the Particle Therapy Co-Operative Group (PTCOG), as of March, 2013 there are 36 facilities performing proton or other particle therapy worldwide; note that seven of these facilities are limited to treating ocular tumors. Between facilities that are both in and out of operation currently, nearly 110,000 patients have been treated with proton therapy [25]. The majority of proton therapy facilities are very large and expensive, costing hundreds of millions of dollars to construct [26]. In order to overcome this obstacle, different compact proton accelerator technologies have been proposed and are at various stages of development. These technologies include the dielectric wall accelerator (DWA) [27], compact synchrocyclotrons [28], and wakefield accelerators [29]. The DWA is the subject of this thesis.

## 1.2 Implementations of Proton Radiotherapy

The vast majority of proton radiotherapy is currently performed with cyclotrons or synchrotrons, while carbon ion radiotherapy is performed exclusively with synchrotrons. A single accelerator will often provide a beam line with ports in multiple rooms, with each room often possessing a rotating isocentric gantry with large bending magnets for beam steering [28]. Synchrocyclotrons capable of accelerating protons to 250 MeV are available from vendors including Ion Beam Applications S. A. (IBA), Varian, and Mevion, and proton synchrotrons are commercially available from vendors including Hitachi and Optivus Technology [30]. Implementation of a multiple room proton radiotherapy facility remains costly, mostly due to the large footprint required, with prices on the order of 150 to 200 million dollars [31]. The most compact proton radiotherapy system currently in clinical use is the Mevion S250 250 MeV superconducting synchrocyclotron [32], which is mounted on a gantry that rotates about the patient and requires a footprint significantly larger than a traditional treatment room (Figure 1.2). Reduction of accelerator size to the point of fitting into a normal radiotherapy bunker would drastically reduce the cost of proton radiotherapy and is the design goal of the DWA.

## 1.3 Organization of Dissertation

This work will begin in Chapter 2 by discussing the function and individual components of the DWA, the current status of its development, and the simulation methods used throughout the rest of the thesis. Chapter 3 contains a study of the electromagnetic properties of individual transmission lines and their various parameters. Building off the work in Chapter 3, Chapter 4 will analyze the effects of stacking said transmission lines in a configuration suitable for producing accelerating gradients for ions. Chapter 5 builds on the stacked line

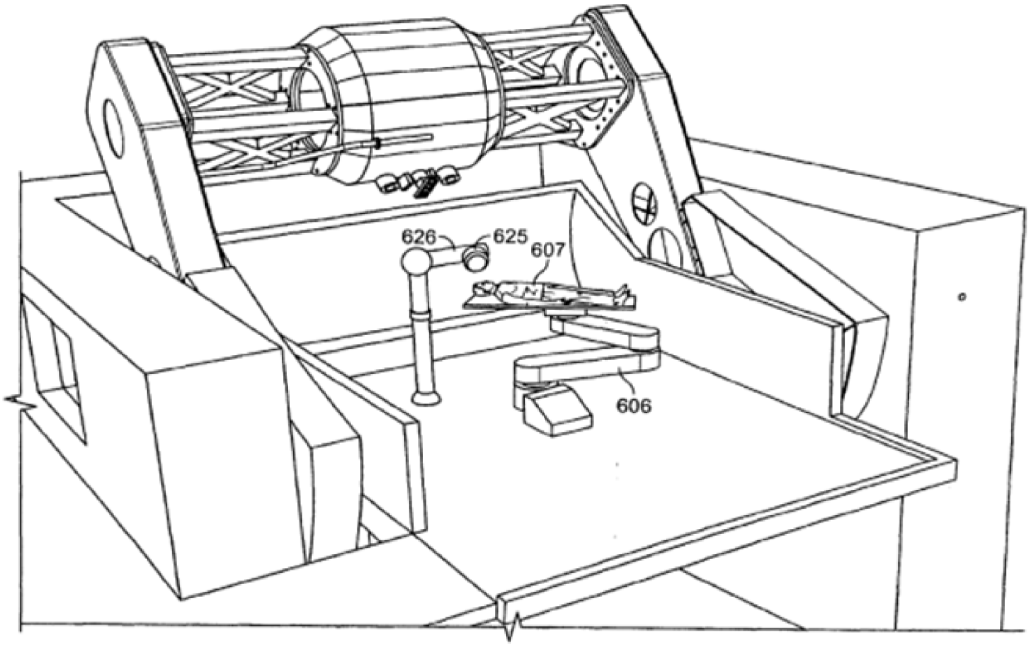

Figure 1.2: Schematic of the Mevion compact synchrocyclotron. Image from Gall, 2013 [2].

geometry with particle simulations of short scale accelerator geometries. Finally, Chapter 6 will investigate several variations of the transmission line geometry and assess different methods of pulse shaping.

# Chapter 2

# Background and Significance

## 2.1 Dielectric Wall Accelerator

The dielectric wall accelerator (DWA) may be broken down into several key components. The beamline portion consists of the ion injector and focusing elements, the dielectric beam pipe, and post-acceleration focusing elements. The power section consists of stacked transmission lines with a number of switches which control the firing of individual transmission lines or simultaneously fired sub-stacks of transmission lines, along with either high-voltage pulsing or charging components corresponding to two different regimes of operation: pulsed voltage injection or charged-discharge. The following section will describe each of these subsystems in detail.

### 2.1.1 Transmission Lines

The transmission line portion of the accelerator is central to the operation of the device. A number of geometric variations exist, but they share certain common characteristics. In most general terms, the transmission lines used in the DWA consist of stacked layers of alternating conducting and insulating materials, the conducting layers of which are connected by switches at some point along the line (often at one end). The closing of the switch results

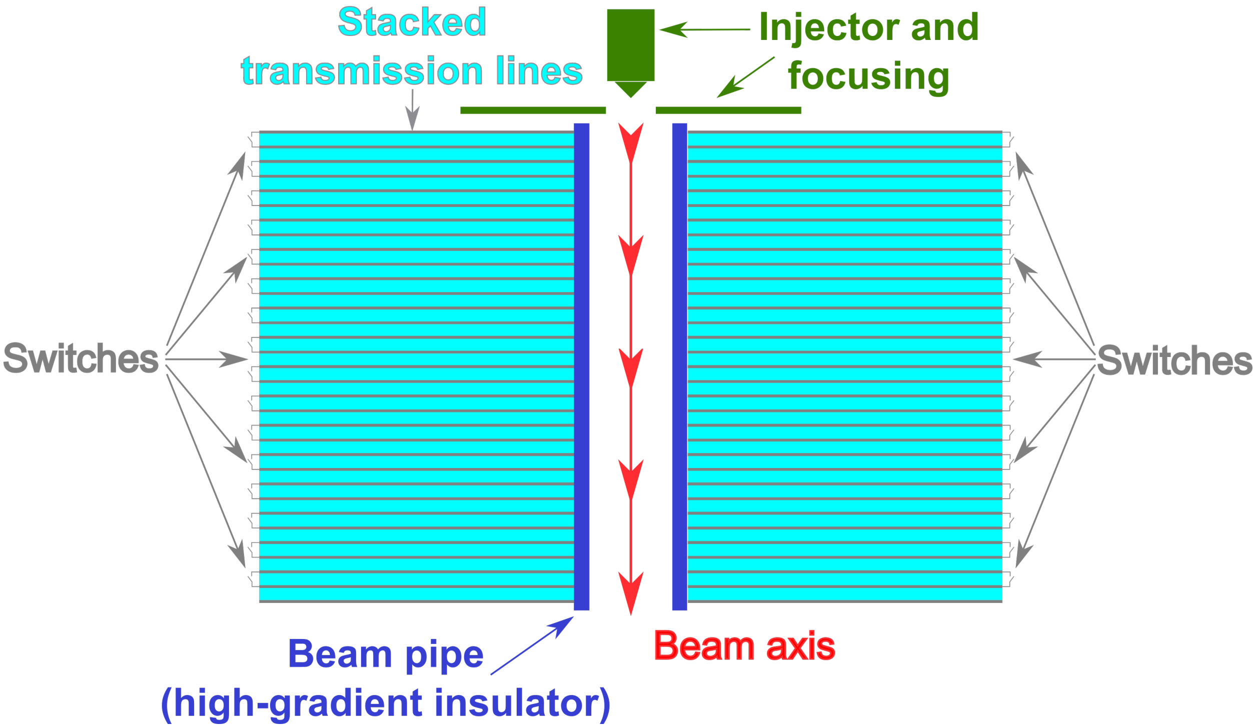

Figure 2.1: A schematic representation of a dielectric wall accelerator.

in an electromagnetic wave which propagates up the length of the line. When the pulse reaches the end of the transmission line, a strong electric field perpendicular to the plane of the transmission line is created. This is the field which ultimately accelerates the particles.

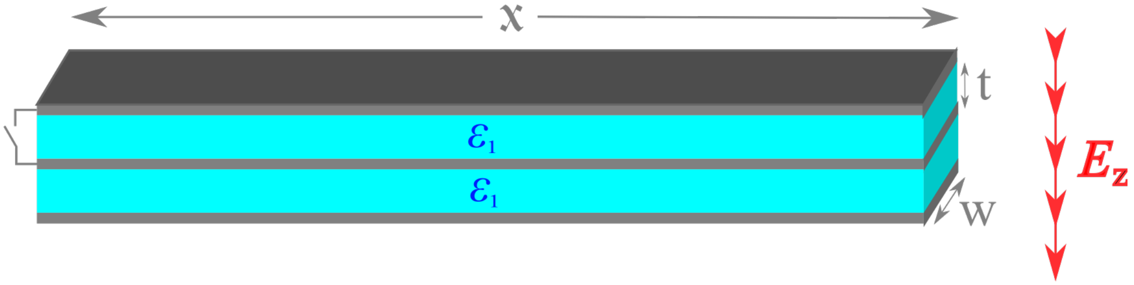

Figure 2.2: A schematic representation of an end-fired transmission line, also showing the axis of the generated electric field.

The time it takes the pulse to propagate up the length of an end-fired line is given by Equation 2.1:

$$t_{BL} = x\sqrt{\mu_0\,\epsilon_0\,\epsilon_1}, \tag{2.1}$$

where x is the length of the transmission line, $\mu_0$ is the magnetic permeability of free space,

$\epsilon_0$ is the permittivity of free space, and $\epsilon_1$ is the dielectric constant of the insulating material between the conducting layers of the lines. The gradient at the ends of the lines then lasts for twice the transit time of the line, as the wave front propagates back and forth along the length of the line, shown by Equation 2.2:

$$t_{duration} = 2x\sqrt{\mu_0\,\epsilon_0\,\epsilon_1}. \tag{2.2}$$

The pulse duration is thus proportional to the length of the line and the square root of the dielectric constant of the insulating layers[33]. In the context of the DWA, these pulses are on the order of nanoseconds. Fuller characterization of these pulses under various conditions is shown in Chapter 3. While these equations do not apply to some more complex variations of the transmission line geometry, such as transmission line transformers, they are illustrative of the behavior of the electric fields within layered conductors and insulators common in most geometries.

Transmission lines also possess a characteristic impedance based on their geometry. The impedance of a transmission line is given by twice the characteristic parallel plate impedance:

$$Z = 2Z_{0pp} = 2\frac{t}{w}\sqrt{\frac{\mu_0}{\epsilon_0\epsilon_1}}, \tag{2.3}$$

where $t$ is the thickness of the line and $w$ is the width of the line. Changes in impedance in transmission line networks generate a reflection related to the relative difference in impedances. The reflection coefficient is given by [34]:

$$\Gamma = \frac{Z_{load} - Z_{source}}{Z_{load} + Z_{source}}, \tag{2.4}$$

where $Z_{source}$ and $Z_{load}$ are the impedances of the input voltage and load, respectively. The transmitted and reflected voltages are then given by:

$$V_{transmitted} = \Gamma\, V_{source}, \tag{2.5}$$

$$V_{reflected} = (1 - \Gamma)\, V_{source}. \tag{2.6}$$

When a transmission line is terminated with an open connection (or extremely high impedance, i.e. $Z_{load} = 0$) between the conductive layers, $\Gamma$ is -1 and the voltage between the top and bottom layers is double that of the injected voltage. These impedance matching considerations are important in the context of the DWA for designing hardware implementations of the voltage inputs as well as being utilized for pulse shaping, which is discussed in Chapter 6.

In order to reduce the occurrence of dielectric breakdown in both the transmission line and the dielectric beam pipe, the desired pulse is short - a few to tens of nanoseconds. The breakdown field strength of a nanosecond pulse may be roughly an order of magnitude higher than that of a microsecond pulse [35, 36]. Due to this short pulse duration, sub-nanosecond switching of the transmission lines is required, as longer switching times will result in the rise time accounting for a significant portion of the pulse duration. A discussion of switching methods meeting this criteria is continued in Section 2.1.3.

Also related to the rise time of the pulse is the dielectric constant of the insulating material (as will be shown in Section 3.1.1). In short, increasing the dielectric constant also increases the rise time of the pulse. Thus, the desired insulator possesses a small dielectric constant while having an extremely high dielectric strength. Good candidates fitting these parameters are polyimides, a family of polymers traditionally used in many types of electronics. Several varieties of polyimide are available under the Kapton® trademark from DuPont. Kapton® films have a dielectric constant of 2.7 to 3.5, with dielectric strengths over 150 MV/m [37]. Additionally, the lossiness of Kapton® is very low - Blumleins up to 48 meters long have been constructed that exhibit losses of only a few percent relative to 9 meter long Blumleins [38]. Thus, for the purposes of the DWA where the desired line length is under 2 meters, the dielectric losses are minimal.

A full simulation study and discussion of the impact of various geometry, electrical, and material variations on the performance of the transmission lines in the DWA may be found in Chapter 3.

### 2.1.2 Beam pipe/High-Gradient Insulator

The beam pipe is a long, hollow cylinder which extends up the length of the accelerator and surrounds the particles as they're accelerated. The interior of the beam pipe is under vacuum for this purpose. Since the accelerating fields are generated outside of the beam pipe, the pipe cannot be a solid conductor (which would electromagnetically shield the interior of the beam pipe - hence the "dielectric wall" portion of the moniker "dielectric wall accelerator"). However, the high gradients generated by the accelerator when operated at high voltages cause dielectric breakdown in the most insulators.

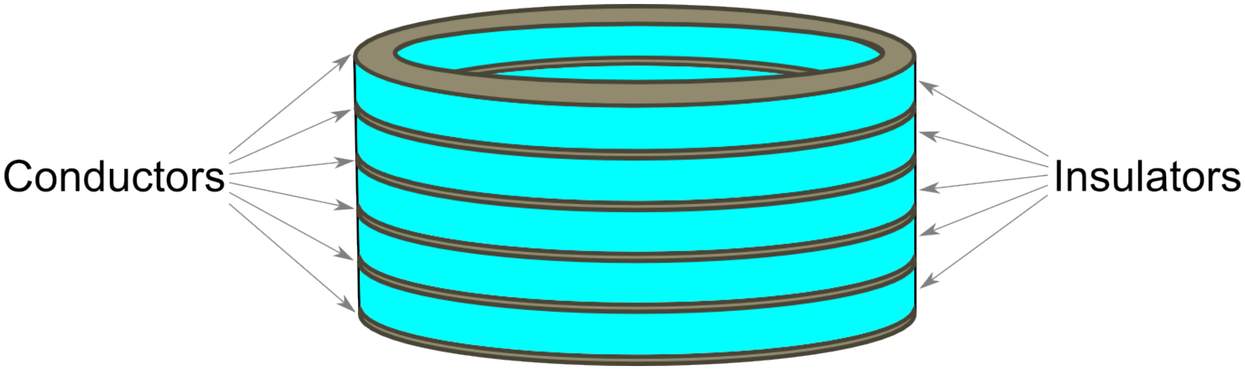

Figure 2.3: Schematic of a beam pipe consisting of a cylindrical stack of high gradient insulator.

The mechanism of dielectric breakdown of particular concern is surface flashover, in which electrons are emitted from the dielectric and traverse its surface through multiple collisions, ionizing adsorbed gasses in the dielectric and generating an arcing electron avalanche which eventually results in total breakdown [39]. While several approaches to increasing the surface breakdown strength of vacuum dielectrics have been investigated, of particular interest in the context of the DWA is high-gradient insulator (HGI) technology [4]. First developed at Lawrence Livermore National Laboratory, an HGI consists of several layers of insulating material interleaved with conductive layers [36]. The beam pipe of the DWA may then be constructed of stacks of cylindrical rings of this material, as shown in Figure 2.3.

Compared to traditional insulators, HGI breaks down at voltage gradients up to 4 times higher than traditional insulators, depending on the specific geometry of the HGI [40, 36]. For pulses under 10 nanoseconds, gradients over 100 MV/m have been achieved before failure [35]. There are two proposed theories of the mechanism behind the increased dielectric strength of HGI materials. In the first, emitted electrons are intercepted by the conducting layers before colliding with the insulator and generating further secondary electrons [41]. In the second, the conducting layers produce equipotential field lines which sweep the electrons away from the surface of the HGI [3]. In practice, both phenomena likely occur, with some electrons being re-absorbed and some being repelled, with trajectories similar to those shown in Figure 2.4. In both cases, the emitted electrons are most often emitted from the triple point of the HGI, where the insulator, conductor, and vacuum intersect [40]. The optimal thicknesses of the insulators and conductors may be optimized to either of these theories - in the case of the Elizando approach, the conductive layers are quite thin relative to the thickness of the insulating layers, while the Leopold approach calls for insulators and conductors of equal thickness. Experiments show that an insulator to conductor thickness of roughly 100:1 yields the highest gradient before surface flashover [4].

In tests of several HGI geometries of varying conductor and insulator thickness, one interesting result is that in all geometries, even after several flashover events and clearly apparent material damage, the HGI samples exhibit a slow degradation in insulator strength rather than a rapid reduction in strength typical of conventional vacuum insulators [4]. This slow degradation is likely due to the vaporization and subsequent deposition of the metal in the conducting layers, resulting in conductive paths along the surface of the insulator [35].

### 2.1.3 Switching Mechanisms

The switching component of the accelerator must be extremely fast, while capable of holding off or injecting very high voltages. Also, the timing jitter of the switches must be extremely

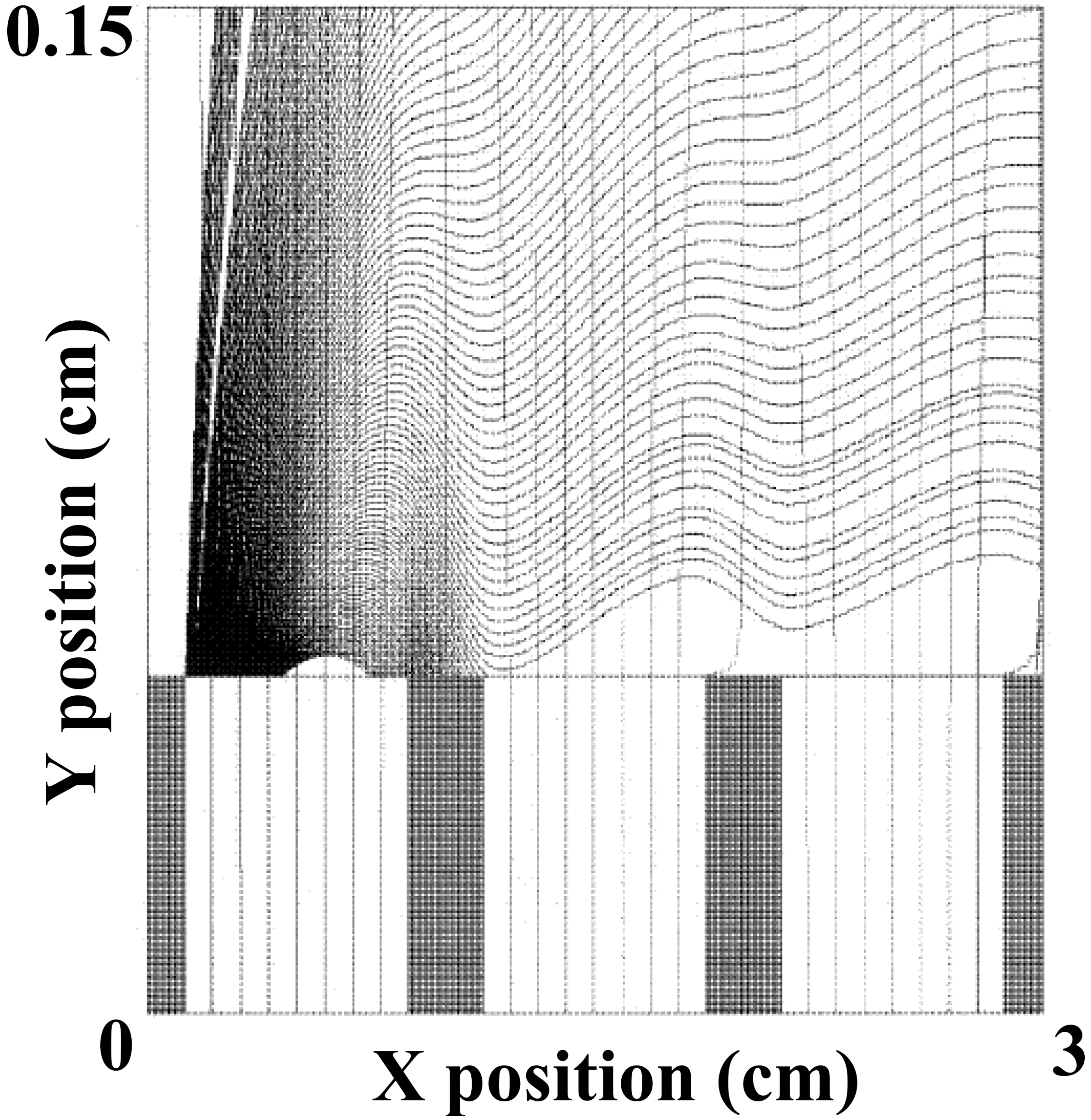

Figure 2.4: Simulated trajectories of electrons generated at the insulator surface in an HGI with an insulator to conductor thickness ratio of 3 to 1. The vertical axis is magnified by a factor of 20. Image adapted from Leopold, 2007 [3].

low in order to match the ion pulse as it travels down the beam pipe. Due to these requirements, the switching module of the DWA is one of the major limiting factors in scaling the DWA to clinically useful energies in a compact manner. Traditionally, switching has been achieved by charging the central conducting layer of the transmission lines relative to the outer layers (or vice versa), followed by closing the switch connecting the conducting layers

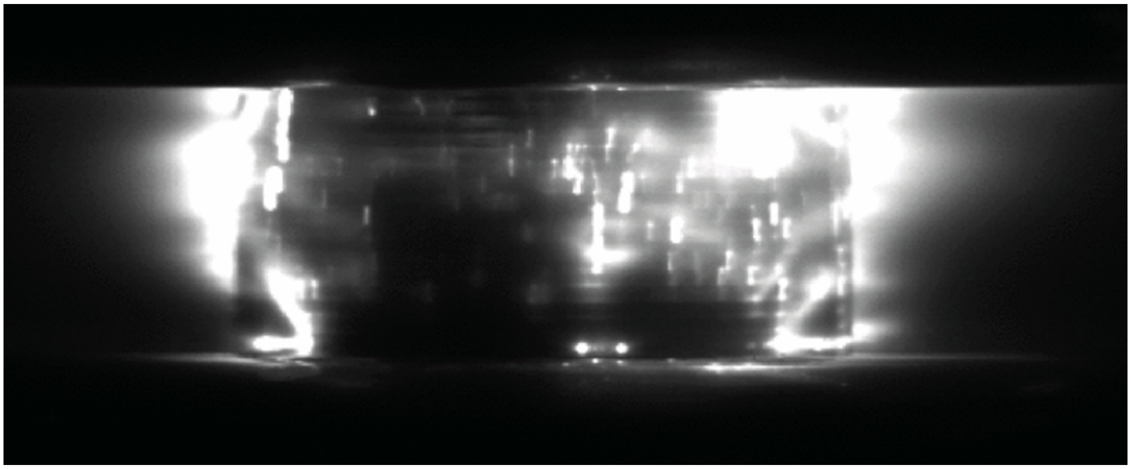

Figure 2.5: High-gradient insulator undergoing surface flashover. The sample is 10.15 mm in height and underwent the flashover event at 19.7 MV/m. The field was created by a Marx generator with a pulse length of 100 ns. Image from Harris, 2007 [4].

[9]. However, another approach using an ultra-fast high voltage injection in place of the switch appears to be a viable alternative, as simulations in Chapter 3 will show.

### Charged-Discharge Mode

One embodiment of the device operates by charging one or more of the plates in a given transmission line and holding off the voltage from neighboring plates using an open switch. The closing of the switch causes current to flow between the plates and forms an electromagnetic pulse that travels the length of the line. Once the pulse reaches the end of the transmission line, an electric field perpendicular to the plane of the line is generated and used to accelerate particles. For this mode of operation the primary switching mechanism of interest has been optical switching, in which an optically transparent semiconductor acts as a strong insulator under normal conditions, but rapidly becomes conductive when illuminated by a laser pulse [42]. Initial efforts utilized GaAs as the semiconductor material, having a bulk dielectric breakdown strength of 20 MeV/m [43]. However, more recent approaches have utilized SiC, which despite having a larger band gap and lower electron mobility than GaAs, possesses an extremely high breakdown strength of 300 MV/m [44]. A schematic of a SiC switch in simplest form is shown in Figure 2.6.

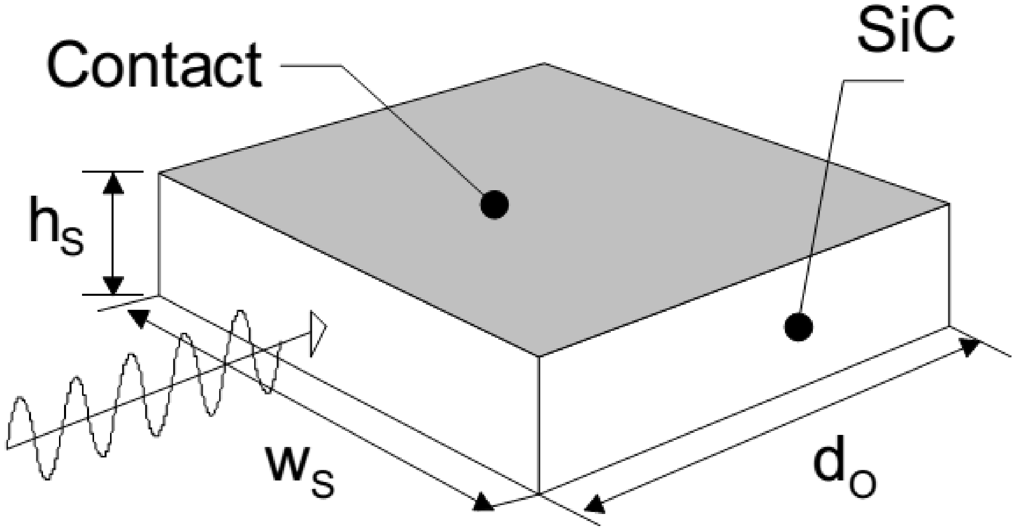

Figure 2.6: A schematic of a SiC optical switch, where $h_s$ and $w_s$ are the height and width of the switch, respectively, and $d_o$ is the optical absorption depth of the triggering laser. Image from Nunnally, 2005 [5].

In practice, however, these SiC switches have been found to fail at much lower voltages than those expected by their bulk breakdown strength. Extremely high current "filaments," despite triggering with uniform optical irradiation, have been observed using infrared imaging on GaAs switches [45], and large (˜10x) field enhancement effects have been observed at the edges of the electrodes in SiC switches [5], resulting in failure at field strengths approximately an order of magnitude lower than the bulk breakdown strength [6]. An image of these failed switches may be seen in Figure 2.7. Various methods have been attempted to increase the hold-off strength of the optically triggered switches, including using curved electrode surfaces [42], customizing the optical input using light guides [46], and surrounding the SiC with a resilient non-photoconductive material such as synthetic diamond [47]. As of the time of writing, the gains of using these methods have not been published.

### Pulsed Injected Voltage

In another embodiment of the device, a very short voltage pulse (on the order of a few nanoseconds) is injected into a transmission line. The sudden voltage difference between two

Figure 2.7: Several failed optical switches consisting of 1 cm x 1 cm SiC layers with 1 mm thickness. Failure occurred at an average field strength of 30 MV/m; field enhancement effects at the edges of the electrodes pushed the field strength to approximately 350 MV/m, causing their failure. Image from Caporaso, 2009 [6].

of the lines creates an electromagnetic pulse that rapidly propagates towards the beam axis as current flows between the two lines. This pulse injection can be accomplished in a number of ways. High voltage thyratrons, such as an EEV CX 2025X deuterium thyratron, have been used for voltage injection, though their relatively high jitter (on the order of nanoseconds) and significant rise times make them less suitable for DWA applications [38]. A high-voltage source held off by an ultra-fast solid-state transistor or MOSFET operated as a closing switch may be employed. This method is limited by the speed and voltage hold-off characteristics of the switch, which heavily influence the efficiency of a particle acceleration and strength of the accelerating gradient, respectively. Operating in this regime, the switch needs to hold off high voltages for the relatively long durations between pulses, and traditional switches with these temporal and hold-off capabilities do not currently exist.

An alternative method of voltage injection consists of a circuit utilizing drift step recovery diodes (DSRDs) operating as rapidly opening switches in order to incite a very short (˜0.1 to 3 ns) voltage pulse of very high strength [8, 48]. Using this method, critical sections of the accelerator are only exposed to high gradients for a few nanoseconds during the pulse, and the likelihood of dielectric breakdown is greatly reduced. First developed in Russia in

1981 [49], present-day DSRDs are capable of switching times of 0.1 to 0.5 ns (at a slew rate of $10^{12}$ V/s), with jitter on the order of 10 ps, allowing for operation up to 10 MHz [50]. DSRD based circuits have been used to generate ultra-fast high voltage pulses [7]. DSRDs themselves consist of a stack of several p-n junction diodes, with the number of layers corresponding to the voltage standoff of the diode [8]. In general, a DSRD based pulse generating circuit requires a second, slower switch (such as a MOSFET) to control the charging voltage and undergoes the following stages (see Figures 2.8 and 2.9):

1. The switch governing the charging voltage is closed, causing the DSRD to develop current in the forward direction while in series with an LC circuit and parallel to the load. Charge is accumulated near the physical interfaces of the p-n junctions within the diode. This charging time must be short (and thus the LC time constant must be small), else the charge will diffuse through the bulk material of the semiconductor layers and later inhibit electron mobility during the discharge and cause deleterious effects in the pulse.

2. After a short period (˜50-200 ns, depending on the LC time constant), the charging voltage switch is opened. A second closing switch to provide a reverse bias voltage in series with an inductor may [51] or may not [8] be used to deplete the charge on the DSRD more rapidly. The DSRD remains conductive in the reverse direction as long as the charge accumulated in step 1 is present.

3. Once all the charge accumulated in step 1 is depleted, the resistivity of the DSRD very sharply increases, effectively acting as an opening switch with an opening time on the order of hundreds of picoseconds. Since the current suddenly stops, the inductors discharge into the load extremely rapidly. This can be understood intuitively by considering that when the current ceases, the magnetic field of the inductor goes to zero extremely rapidly, generating an electric field in the circuit in accordance with Faraday's law ($\nabla \times \vec{E} = -\frac{\partial B}{\partial t}$), which along with Lenz's law, produces an electromotive

force of $\varepsilon = -L\frac{dI}{dt}$. Thus the stored energy of the inductors (given by $W = \frac{1}{2}LI^2$ ) is very quickly diverted into the load [52].

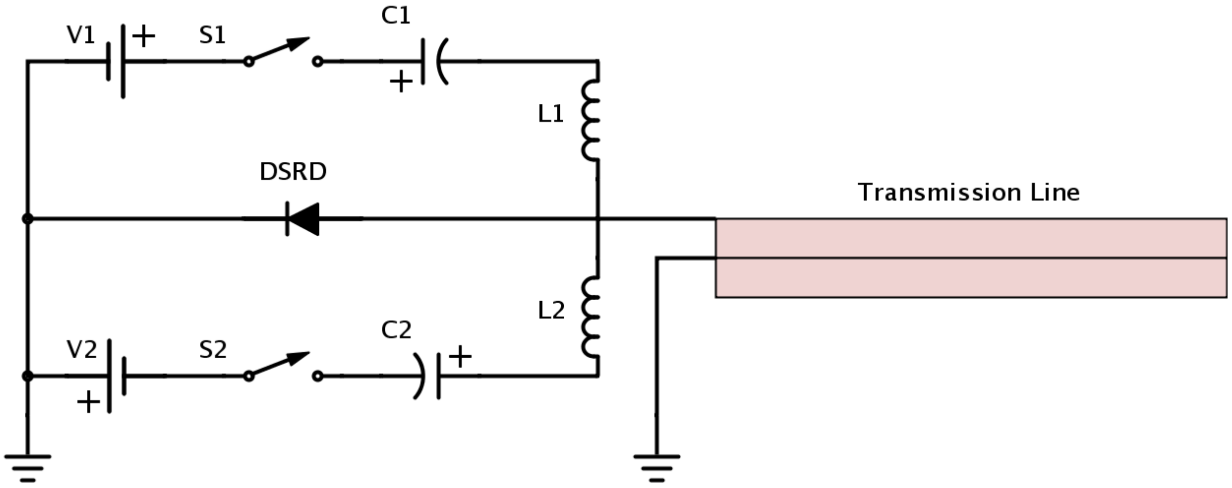

Figure 2.8: Circuit representing a DSRD-based voltage injection into a transmission line. Circuit design adapted from Efanov, 1997 and Artz, 2009 [7, 8].

### 2.1.4 Particle Injector

A number of different particle sources and injector structures may be used in a DWA. Options include duoplasmatron, used in the proton therapy synchrotron at Loma Linda [53] and in DWA prototypes built by Compact Particle Acceleration Corporation (CPAC) [9], and electron cyclotron resonance (ECR) ion sources, used in the Heidelberg medical synchrotron [54]. Both classes of devices are capable of creating and initially accelerating protons as well as heavier ions such as carbon. Following ion production, ion beams may be initially accelerated by a radio frequency quadrupole (RFQ) accelerator (or induction cells [6]) prior to injection into the main accelerator, and focusing elements such as einzel lenses are often used for beam optics throughout the injector [9, 55, 6]. One study stated that the injection requirements for proton therapy require the ion beam to exit with an energy of 1 MeV or higher and a temporal pulse width of <300 ps for efficient acceleration by short accelerating pulses, while the beam radius must be <3 mm with an emittance <8 mm-mrad, and the

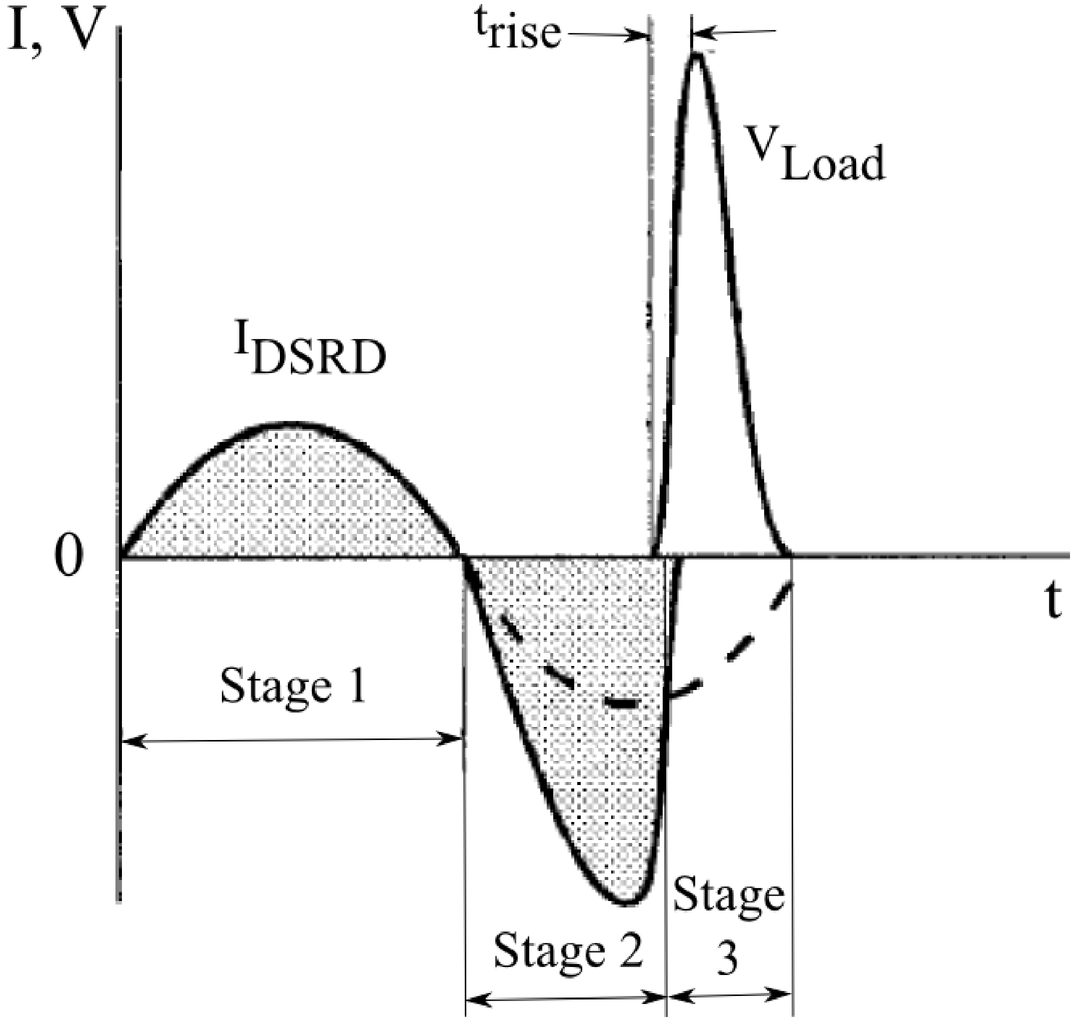

Figure 2.9: Current in the DSRD (shaded area) and voltage output to the load (unshaded area) when operating a DSRD as an opening switch. Image modified from Efanov, 1997 [7].

repetition rate must be adjustable from a single shot up to 10 Hz with charges of 3 to 30 pC per pulse [56]. At 10 Hz and 30 pC per pulse, the beam current would average to be 0.3 nA; a higher repetition rate or charge per pulse may be needed to reach the 0.5 to 1 nA current necessary to treat at 2 Gy/min [57].

## 2.2 Existing Prototype Dielectric Wall Accelerators

The origins of the DWA can be traced to linear induction accelerators first developed at Lawrence Radiation Laboratory in Livermore, CA (now Lawrence Livermore National Lab) in the 1960s as a part of the Astron fusion experiment [58]. While capable of high beam currents (hundreds of A), the Astron linacs created average gradients less than 1 MV/m and required bulky ferromagnetic cores [59]. Modern induction linacs are capable of generating multiple kA electron beams, but still possess the drawback of limited gradients; the DWA concept was thus conceived from the goal of increasing the gradient in these linear induction accelerators [60].

A short-scale text accelerator based on DWA principles was constructed at Lawrence Livermore National Lab in the late 2000s. This device, named First Article System Test (F.A.S.T.), consists of a short stack of Blumlein transmission lines abutted against an HGI beam pipe with a 4 cm bore (Figure 2.10). Protons were generated by a gated spark discharge source and initially accelerated to 250 keV by a 5-cell induction injector [6]. Optical SiC switches were illuminated and triggered by a single split laser pulse. The insulating layers of the Blumleins were constructed of FR-4 dielectric (with a dielectric constant between 4 and 5, depending on frequency [61]), and possessed an impedance of 40 Ω. Thus, the lines rang for several cycles due to reflections. To measure the properties of the accelerated beam, a Thomson spectrometer was located downstream from the injector and accelerator. Proton energies were measured when the pulse from the Blumleins was both synchronized to accelerate and decelerate the particles, as well as when the lines were not fired at all. When synchronized with the accelerating portion of the pulse, an energy gain of about 40 keV (working out to 1.6 MeV/m) was found at the highest switching voltages. However, these accleration tests were limited by the switches failing at much lower voltages than expected, as discussed in Section 2.1.3 [62].

An engineering prototype DWA system for accelerating protons has been built by the Compact Particle Acceleration Corporation (CPAC)(Figure2.11 [9]. The proton injection

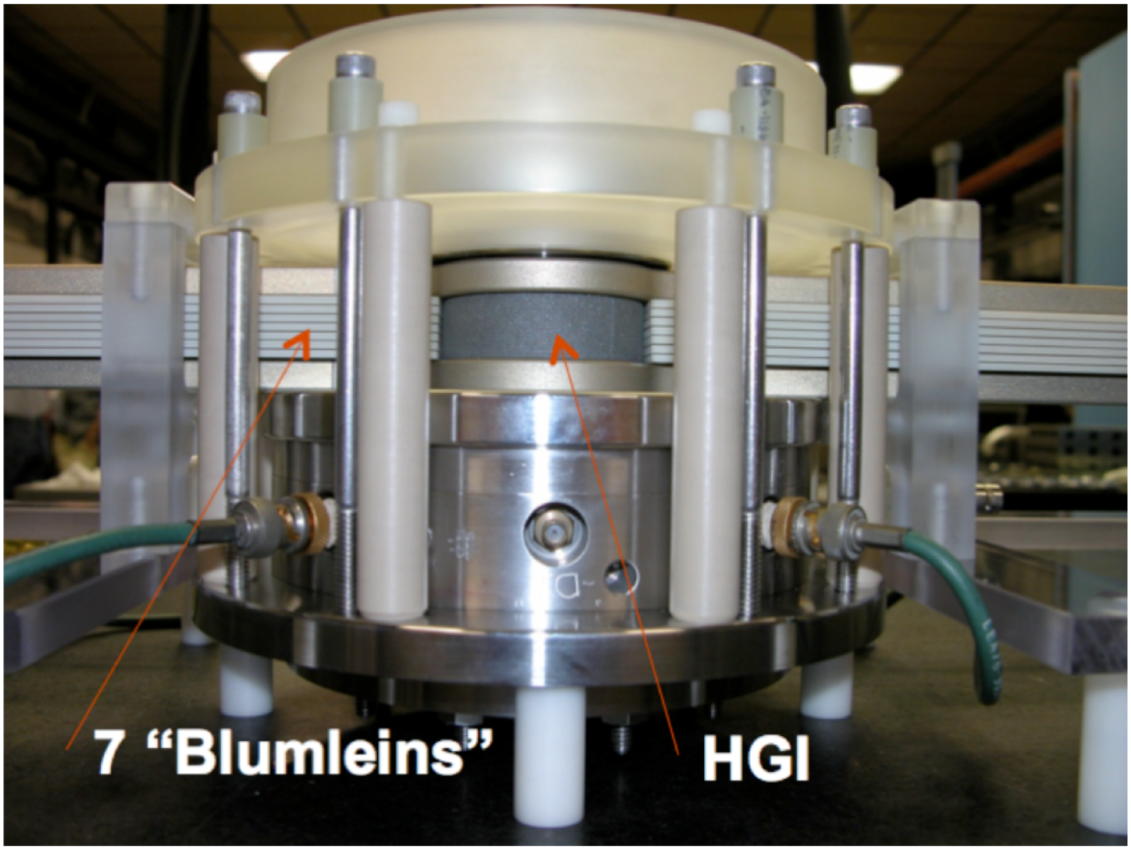

Figure 2.10: Photograph of the F.A.S.T. setup, consisting of a 2.5 cm high HGI beam pipe with a 4 cm bore and two stacks of 7 “Blumleins” on either side of the HGI. Image from Caporaso, 2009 [6].

system of this prototype consists of a duoplasmatron ion source which emits protons at 35 keV, followed by a “kicker” which deflects the beam such that only single 2.35 ns bunches (corresponding to a single rf cycle in the subsequent RFQ) are accepted to the next stage of the accelerator. Finally, an RFQ linac accelerates the protons to 2 MeV before entering the DWA portion of the device [56]. The DWA portion of the system consists of a 10 cm HGI beam pipe and two matched 3 cm stacks of 15 Blumleins; each Blumlein is 60 cm long, 2 cm wide, and 2 mm thick (Figure 2.12). This system, as described, achieved energy gains of nearly 80 keV [9], while later iterations of the prototype have achieved gradients of 15 MeV/m [63]. An alternate geometry, utilizing 24 dipole lines per layer, was also investigated by CPAC [63].

Finally, a group at the Institute of Fluid Physics (IFP) in China is developing a DWA

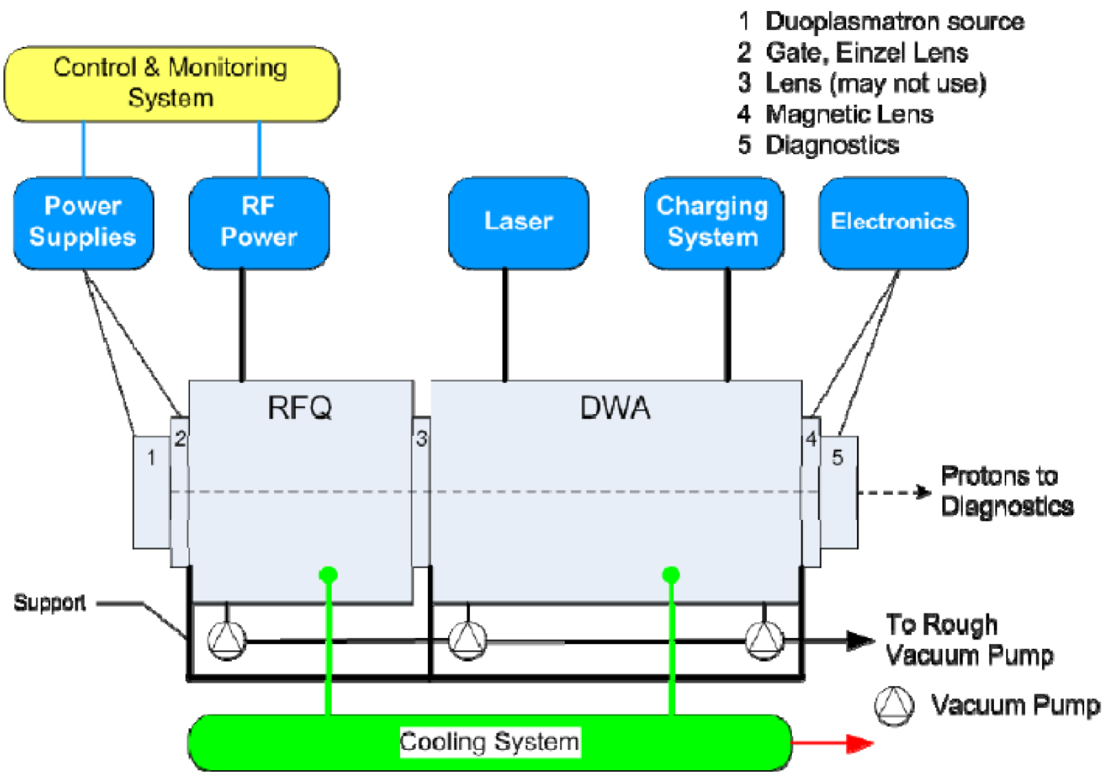

Figure 2.11: Block diagram of the engineering prototype built at CPAC. Image from Zografos, 2011 [9].

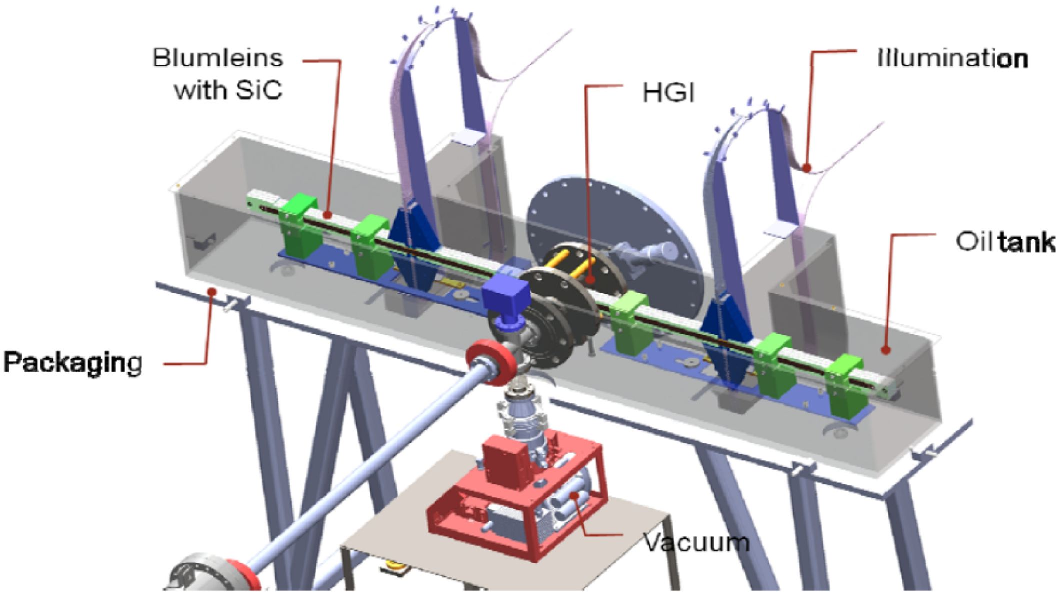

Figure 2.12: Rendering of the prototype DWA built by CPAC. Image from Zografos, 2011 [9].

prototype [64, 65]. The group aims to develop a 1 MeV DWA utilizing parallel plate Blumlein transmission lines triggered by optical switches and an HGI beam pipe, with a goal gradient of 20 MeV/m; beam transport studies of the device have been published [64]. Beam transport studies for a 10 MeV version of the device have also been published [66]. At Peking University, a 40 keV proton injector has been built for the proposed device, with researchers expecting to commission the combined injector and DWA in the near future [65].

## 2.3 Other Applications of Dielectric Wall Accelerator Technology

In addition to use for radiotherapy, the DWA architecture has potential to be useful in several other fields. One application is package screening for homeland security applications. Researchers at Lawrence Livermore National Lab have proposed using a DWA for versatile package testing using multiple accelerated ion species in order to detect nuclear and multi-component liquid threats [67].

Another potential application is in particle-induced X-ray emission spectroscopy (PIXE). PIXE is a multi-elemental analysis technique which is performed by irradiating a sample with a proton beam with a typical energy of about 2 to 3 MeV or an He ion beam of about 4 to 5 MeV. This irradiation causes K- or L-shell electrons to be knocked out, causing a de-excitation of a higher shell electron and emitting a characteristic x-ray. These x-ray emission peaks are then resolved using Si(Li) or similar detectors [68]. The compact structure and multi-ion capabilities of the DWA make it appealing for this application, as these energies could feasibly be achieved in tens of centimeters. This could allow for benchtop elemental analysis that could be incorporated in a system such as the sequential tissue erosion imaging (SETI) device developed at UW-Madison [10] and allow for combined imaging of optical and atomic composition (see Figure 2.14). Helium gas may be blown over the sample to minimize perturbation of the ion beam in atmospheric conditions.

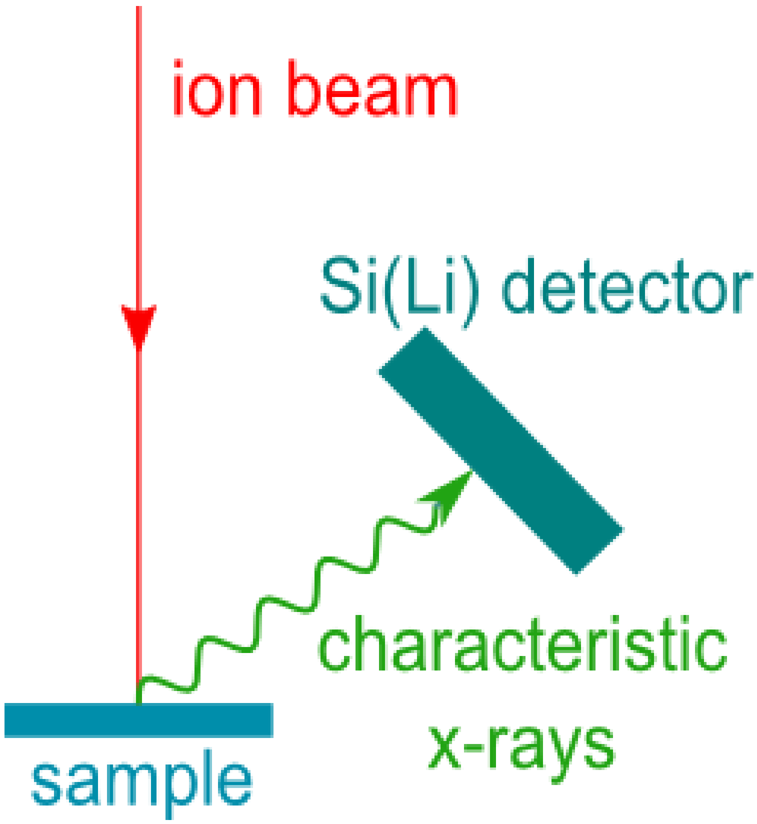

Figure 2.13: A schematic drawing of the PIXE process.

## 2.4 Electromagnetic and Particle Simulation Methods

### 2.4.1 Finite Element Electromagnetic Simulation Methods

While various software was used to simulate the electromagnetic fields in the following simulations, they all use finite element analysis to solve Maxwell's equations on a grid-discretized representation of the geometry being simulated:

$$\begin{aligned}
\nabla \cdot \vec{E} &= \frac{\rho}{\epsilon_0}, \\
\nabla \cdot \vec{B} &= 0, \\
\nabla \times \vec{E} &= -\frac{\partial B}{\partial t}, and \\
\nabla \times \vec{B} &= \mu_0 \vec{J} + \mu_0 \epsilon_0 \frac{\partial E}{\partial t}.
\end{aligned}$$

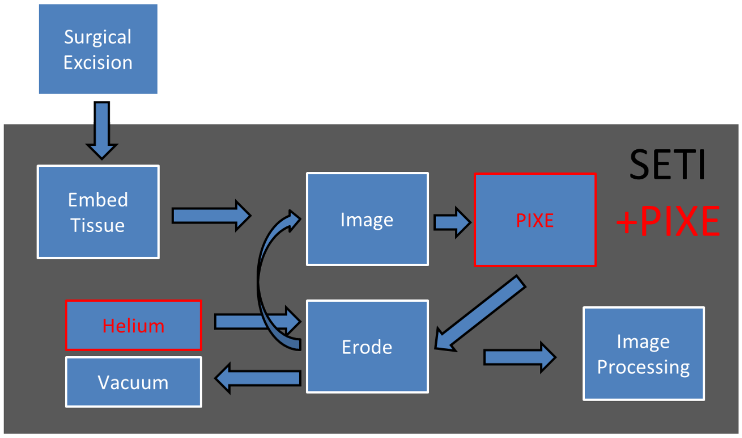

Figure 2.14: Block diagram of a combined SETI-PIXE system. Image modified from Bredfeldt, 2014 [10].

The finite difference time domain (FDTD) method was first proposed by Yee in 1966 [69]. This method is implemented in a number of software packages, including XFdtd (Remcom, Inc.), used in portions of this research. The finite integration technique (FIT) is a very similar time-domain method developed to efficiently solve Maxwell's equations in their integral form, rather than finite differences as used in FDTD. This distinction allows for simpler representations of some geometry features in FIT, such as thin sheets. The method was first developed by Weiland in 1977 [70, 71] and is used in CST Microwave Studio, the software utilized for the majority of simulations in this work. Time-domain methods are conducive to simulating the properties of the DWA, as modeling the sequential triggering of transmission line stacks and the travel of a particle bunch are not well suited to frequency domain methods.

Both methods discretize the geometry of the simulation into a finite mesh. The electric and magnetic fields are then updated in an alternating fashion at subsequent time steps on grids that are offset from each other (generally by half the cell size - see Figure 2.15). The grid resolution determines the maximum time step required for stability of the simulation. The simulation may be run for an arbitrary number of time steps, and the full 3D fields at each time step may be stored for analysis [11].

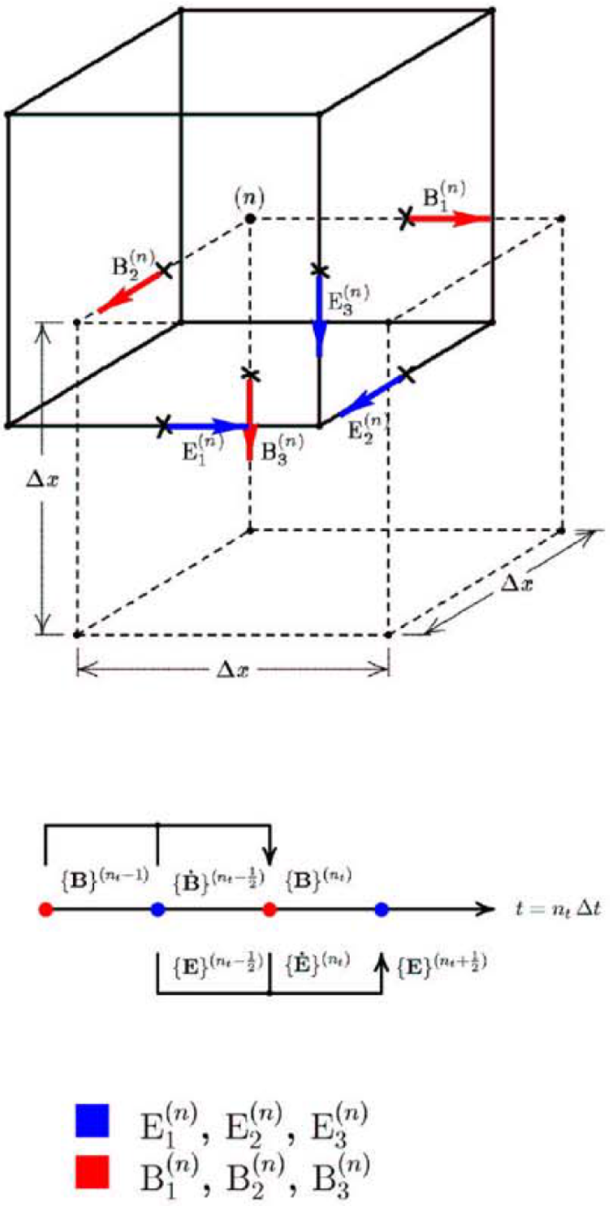

Figure 2.15: Schematic of the offset grid method used in the finite integration technique. Image from Marklein, 1999 [11].

### 2.4.2 Particle In Cell Method

The particle-in-cell (PIC) method is a particle tracking technique which is capable of incorporating the electromagnetic fields generated by both transient external sources and geometries as well as those generated by a distribution of charged particles. This method is better suited to simulating the DWA, as simpler tracking methods often consider only static external fields.

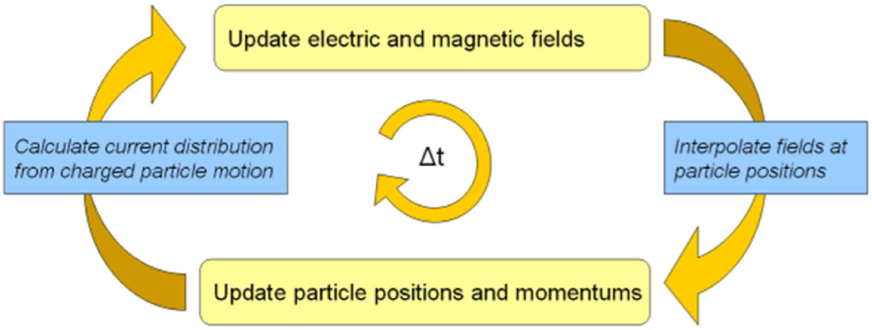

Figure 2.16: Block diagram of the particle-in-cell method utilized by CST Microwave Studio. Image from CST, 2014 [12]

A PIC solver is offered as a part of CST Microwave Studio (CST, Inc.) and was used for simulations found in Chapter 5. Their implementation of PIC tracks particles in continuous phase space, independent of the calculation mesh of the external fields (such as those caused by the transmission lines of the DWA). The method calculates the electromagnetic fields at a given time step on the calculation mesh, linearly interpolates those fields to the position of each particle, updates the particle positions and momenta based on those fields, and updates the electromagnetic fields accordingly (see Figure 2.16). The PIC model incorporates space charge, a variety of different emission models for particle sources, sheets that are variably transparent to particles for modeling beam windows, and export of the full 3D trajectories of each particle [12], making it a powerful tool in the analysis of accelerator performance.

# Chapter 3

# Transmission Line Characterization

## 3.1 Single Transmission Line Simulations

In order to understand the operation of the device as a whole, we must first understand the behavior of individual transmission lines. A number of geometric, material, and electrical properties impact the performance characteristics of the bulk accelerator. Through simulation, we can vary these parameters to determine their impact on the performance of the device. When considering individual line performance, the temporal properties of the generated pulse are key. In one spatial dimension, these properties include pulse duration, shape, and magnitudes both immediately at the end of the line and height along the beam axis. Expanding to two and three dimensions, the behavior of the generated pulse along the rest of the beam axis is equally important, as the particle bunch must necessarily pass through these regions. The behavior of the field in the transverse plane, parallel to the transmission lines, is also important for the uniformity of the accelerated particle bunch.

### 3.1.1 Voltages and Electric Fields Generated

The simplest transmission line geometry simulated here consists of three conducting layers separated by thicker layers of insulating material. The following section will investigate how the variation of the various parameters of this simple line impact the ultimate accelerating pulse seen at the beam axis. These parameters include both the geometric dimensions and electrical properties of the line.

A reference transmission line was modeled and simulated as a reference point to parameter changes. The model utilizes annealed copper as a conductor and lossy polyimide as the insulating material. The insulating layers are each 1 mm thick, the copper layers are 0.1 mm thick, and the length and width of the line is 40 cm by 10 cm. An excitation pulse representing a 10 kV injected voltage in the shape of a smooth step function with a 0.5 nanosecond rise time was provided to a discrete edge port to model the switching of the line. Use of an edge port to model a switch or injected voltage is represented in the literature with good agreement with experiment [63]. The method of using a smooth step function as the excitation source is accurate for the first modeled pulse: however, the interactions between the reflected pulses and the port are not representative of the actual behavior of such a system, and later pulses will be inaccurate. The rationale for using this simplified injection pulse is to well characterize and isolate the behavior of the transmission lines themselves and exclude the impact of any specific switch or pulse. As such, only the first pulse is shown in Figure 3.1. Shown is the voltage difference between the top and bottom copper plates at the end of the transmission line. The pulse duration is in good agreement with that calculated from Equation 2.2, which is 4.99 ns. The magnitude of the output voltage pulse is roughly double that of the injected pulse, as expected.

The voltage pulse shown in Figure 3.1 illustrates the voltage at the end of the transmission line, not the accelerating field at the beam axis. The electromagnetic fields that radiate from the end of the line are what ultimately accelerate the particles. The accelerating gradient is the Z component of the electric field some distance from the end of the transmission line and has a shape very similar to the voltage output of the line. The X, Y, and Z components of the electric fields 1 cm from the end of the benchmark line are shown in Figure 3.2. Note that the X and Y components of the field are much smaller than the Z component, and in

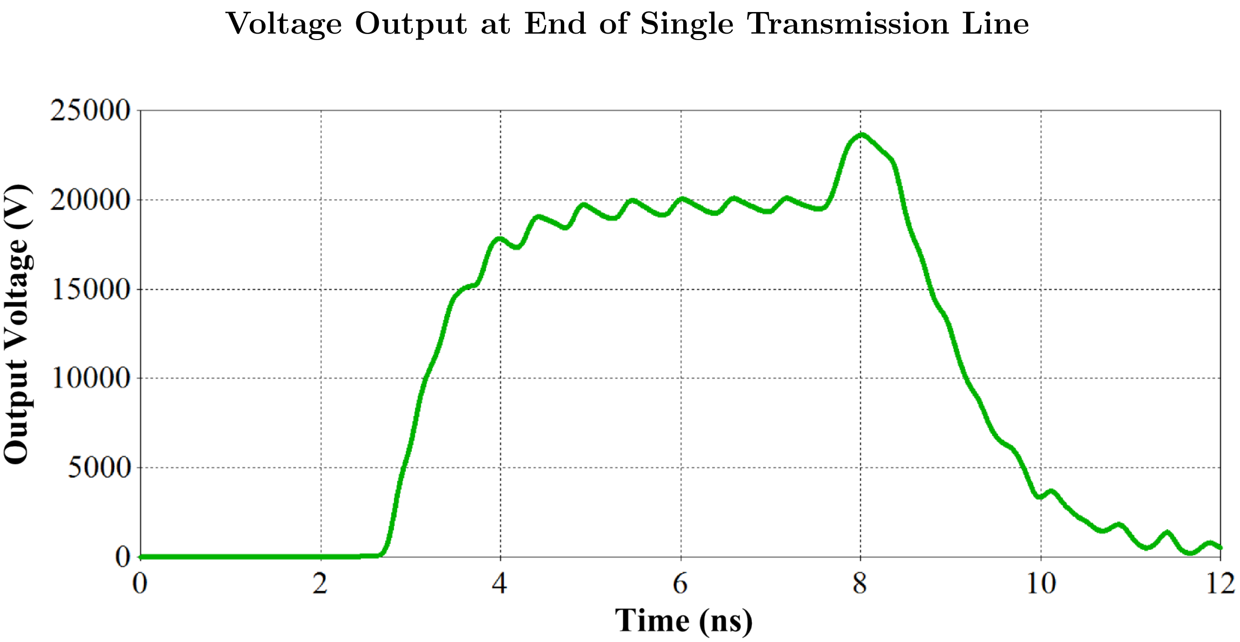

Figure 3.1: Simulated voltage output for a single transmission line receiving a 10 kV injected voltage pulse. Note the doubling of the injected voltage.

particular, the X component has a magnitude of nearly 10 kV/m. These significant fields may be canceled out through the addition of an opposed line, as shown in Section 3.2.

The propagation of the fields into space may be visualized by taking a 2D slice of the solved 3D fields. Each spatial component of the field may be plotted, as can the absolute value of the electric field. These fields are available at each time step of the simulation and may be displayed as an animation. This type of visualization helps to illustrate a number of behaviors in the lines. Looking at Figure 3.3, it is apparent that the magnitude of the accelerating field falls off rapidly from the end of the line (an effect further investigated in Section 3.2). Furthermore, the fields have a significant magnitude at points above and below the plane of the transmission line along the beam axis. The behavior of these fields will be important to consider and characterize as well, as will be discussed in Section 3.1.2.

Similarly, we can look at the fields in the XY plane of the beam axis in qualitative terms. We can see that the fields generate a region of high electric field in the Z axis that is maximized at the center of the line in both directions. Again, note the large fields at regions above and below the line - this indicates that the fields of a single line have a large impact

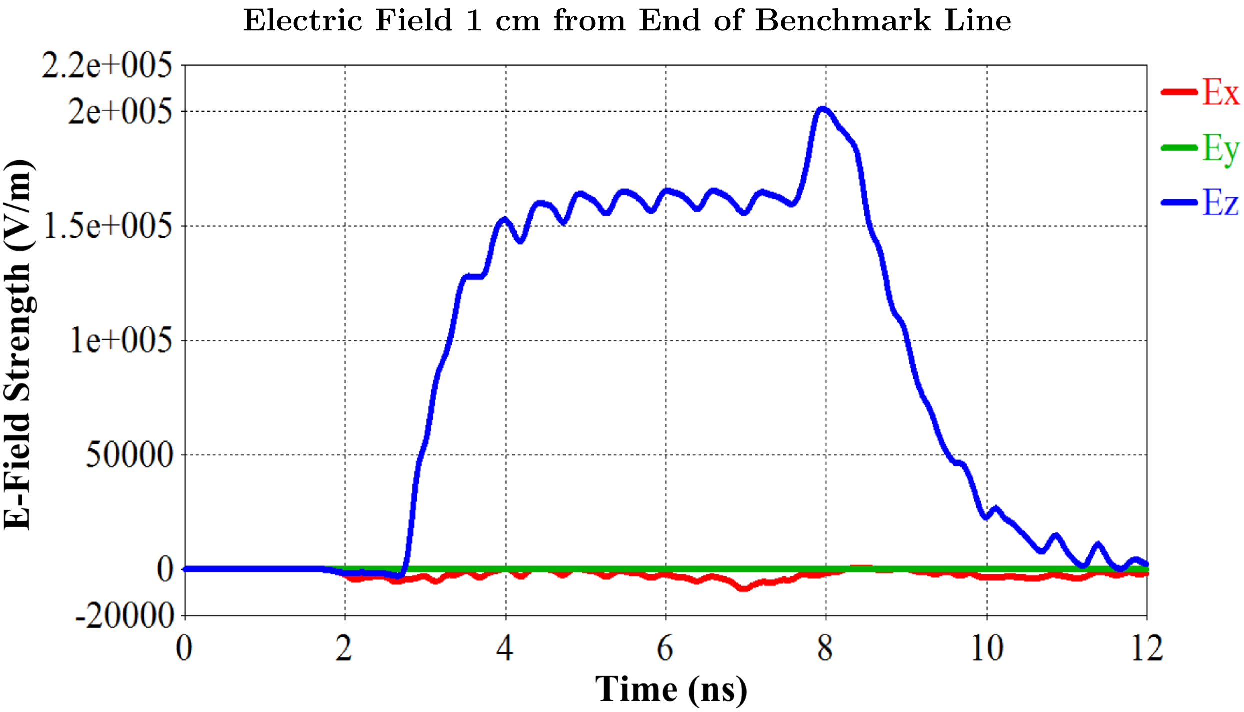

Figure 3.2: Accelerating and transverse gradients 1 cm from the end of the benchmark transmission line.

on the effective gradient at other points along the accelerator, an effect further discussed in Section 3.1.2.

### 3.1.2 Axial Analysis

The above analyses considered the fields produced by the transmission line in the same plane as the line itself. However, it is important to realize that the lines induce strong electric fields above and below this plane as well. Figure 3.5 shows the fields at a moment in time during the pulse (at t = 7 ns) along an axis perpendicular to the plane of the line, corresponding to the beam axis. In other words, the x-axis of the Figure 3.5 is the beam axis. Examining the fields as such gives insight into the influence each transmission line has upon the entirety of the beam pipe, rather than single points adjacent to the beam pipe. The following figures show the fields at a single point in time, during the peak of the pulse; however, the fields are available at each time point of the simulation and may be animated to illustrate the

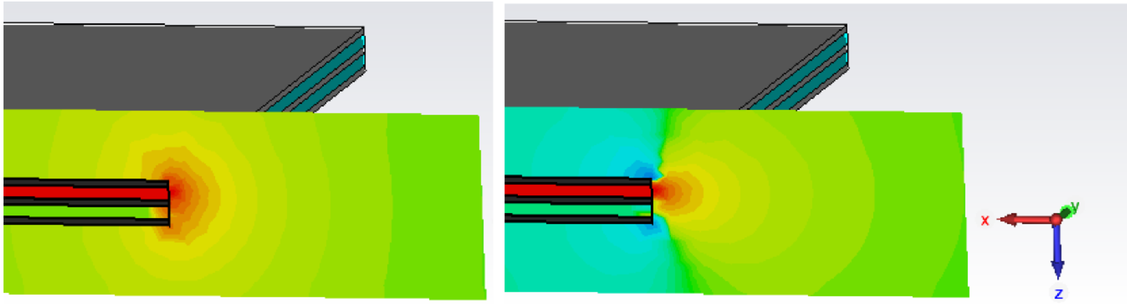

Figure 3.3: Cutplane in XZ showing the absolute value (left) and Z component (right) of the electric field generated by a transmission line during a pulse.

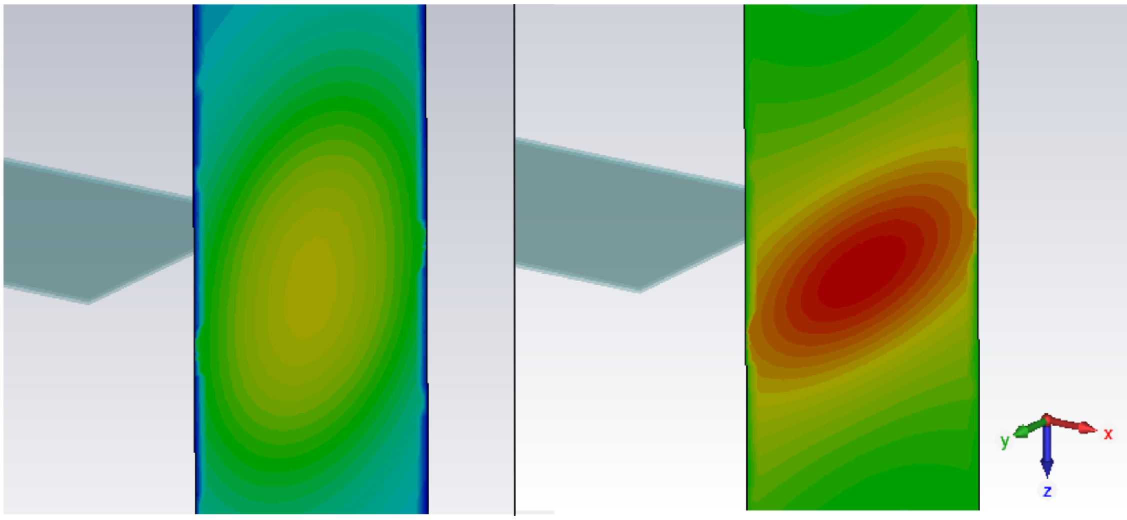

Figure 3.4: Cutplane in XY showing the absolute value (left) and Z component (right) of the electric field 5 cm from the end of a transmission line during a pulse.

temporal properties of the axial fields.

A number of observations may be made through examining Figure 3.5. First, the X component of the field is nearly as large as the accelerating gradient, pointing away from the end of the line (the negative X direction) above its plane, and in the positive X direction below the line. These large transverse fields, significantly larger than the 10 kV fields seen in the transmission line plane shown in Section 3.1.1, would certainly push the ions off of a straight trajectory through the accelerator. These fields may be effectively canceled out with the addition of another, matched line in the X direction, as discussed in 3.2. The Y component of the field at the beam axis is negligible, as the geometry around the curve is symmetric in

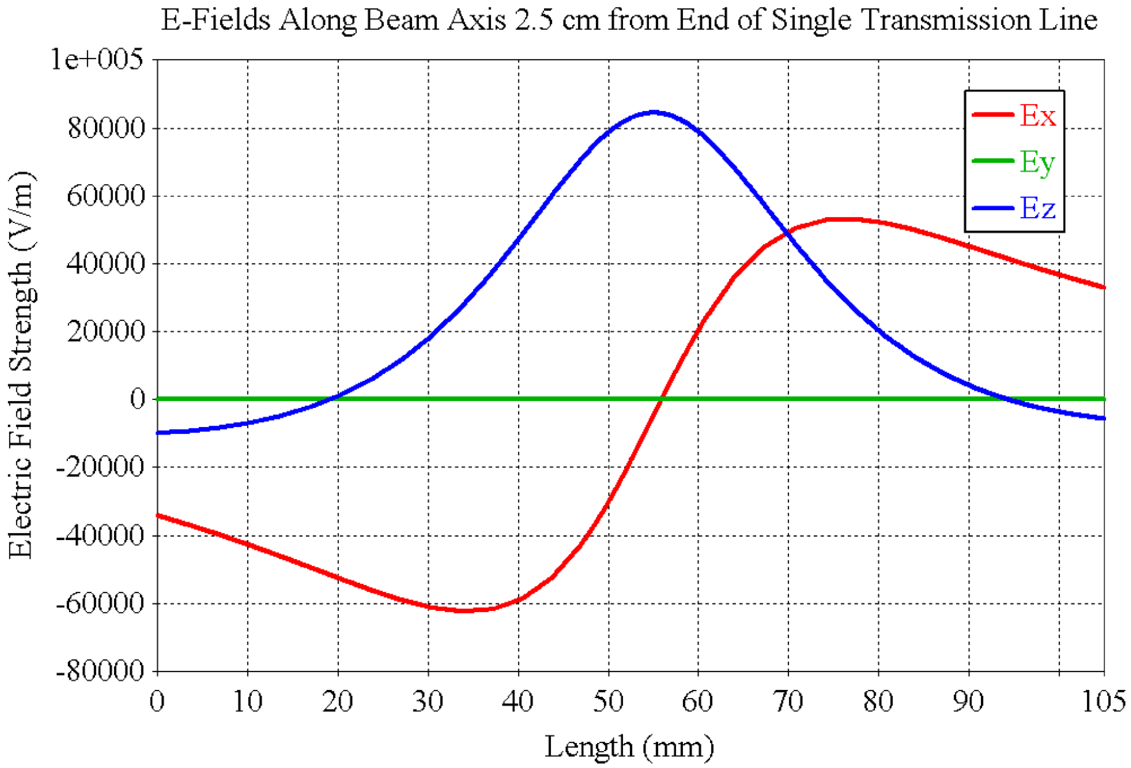

Figure 3.5: Electric fields generated by a single transmission line along the axis 2.5 cm from the end of the line during the peak of the pulse.

the Y plane. Finally, the Z component of the electric field becomes negative some distance above and below the line. This creates an "axial parasitic" effect not previously discussed in the DWA literature (Figure 3.6). The effect emphasizes a number of design considerations. Poor timing when triggering lines will actively decelerate the particle bunch, requiring an extremely precise firing schedule. Excessive ringing in the accelerator will cause deleterious effects to the gradient, even far from the ringing lines. Finally, the duration of the pulse must be well suited to the particle bunch dwell time; if the pulse is much longer than the time the particles spend next to a given set of lines, the negative tails of the axial gradients will hinder the possible gradients of neighboring lines. The magnitude of the negative lines is exacerbated by stacking, which is shown in Chapter 4.

The behavior of the axial gradient as you move from the end of the line is shown in Figure 3.7. Moving further from the ends of the lines, the peak strength of the gradient rapidly falls

**Accelerating and Decelerating Axial Gradients Produced By Single Transmission Line**

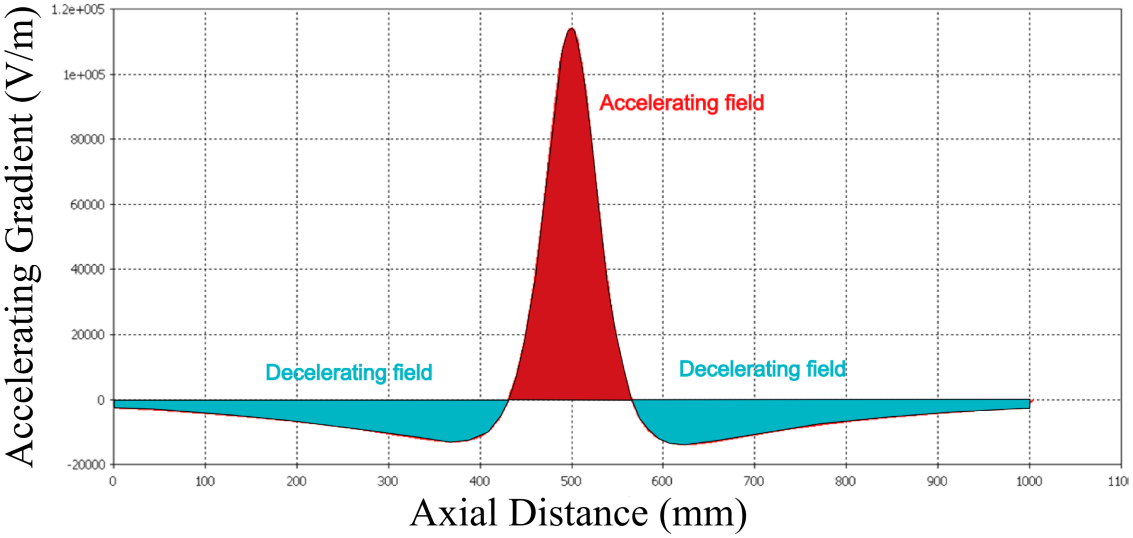

Figure 3.6: A illustration of the axial parasitic effect induced by a transmission line.

off, dropping by a factor of two simply by moving 4 mm (from 0.6 cm to 1 cm) from the line terminus, emphasizing the need to minimize the radius of the beam pipe bore as much as possible. The nearer axes, however, create a narrower region of acceleration spatially along the beam axis, with a negative region larger in magnitude. This negative region still occurs at a distance along the axis several times the width of the transmission line; for example, at 1 cm from the end of the line, the axial gradient does not become negative until about 2 cm above and below the line. A further effect of the shape of these axial pulses is that adjacent lines increase the gradient, allowing for fields on the beam axis to be much greater when the lines are stacked. This will be further discussed in Chapter 4.

It is also useful to inspect the X and Y components of the fields away from the central axis. However, these fields are changed significantly by the addition of a matched line, and their behavior will be further discussed in Section 3.2.2.

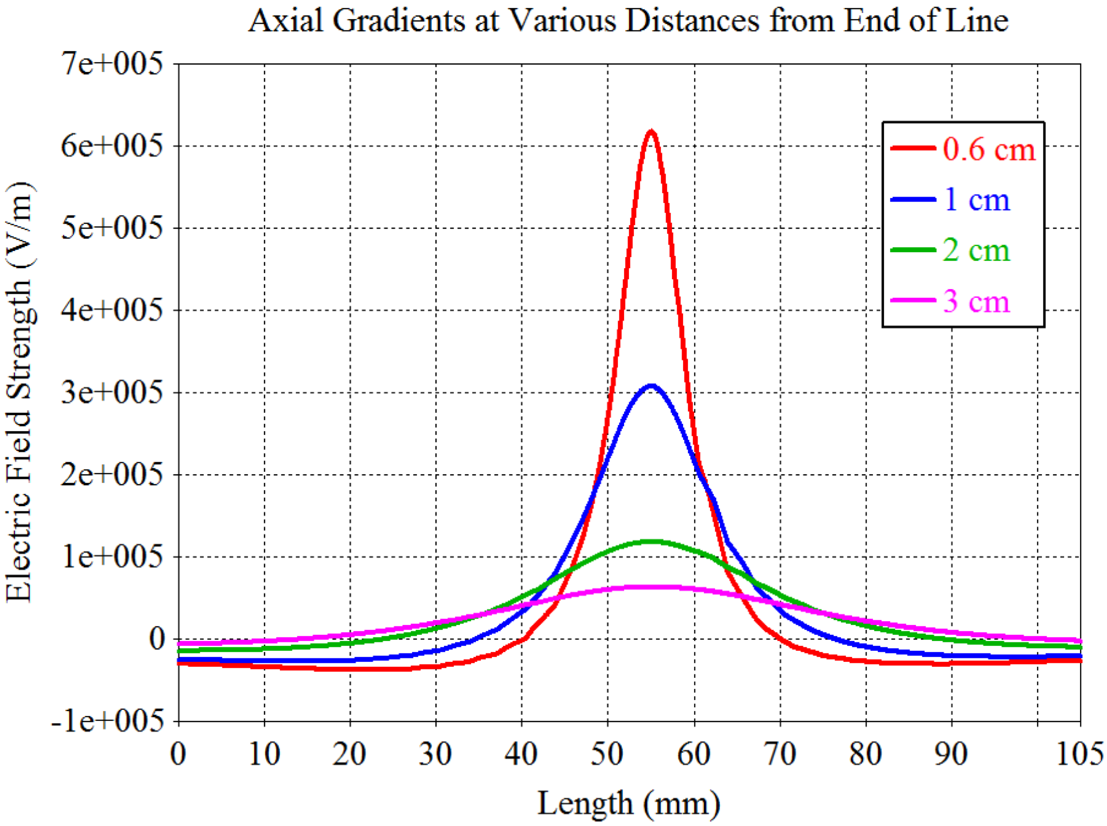

Figure 3.7: Axial gradients generated by a single transmission line along the axes of varying distances from the end of the line. The transmission line is centered at 55 mm.

### 3.1.3 Dielectric Constant Variation

To investigate the impact of changing the dielectric constant, this value was varied over several simulations. A representative comparison of three different dielectric constants, centered around that of polyimide at 3.5, is shown in Figure 3.8. In agreement with Equation 2.2, the pulse duration scales with $\sqrt{\epsilon_1}$, as does the rise time. Since the desired pulse is relatively short to avoid dielectric breakdown (<10 ns) and deleterious line-to-line interactions discussed in Chapter 4, a short rise time is preferred, and thus a relatively low dielectric constant is needed.

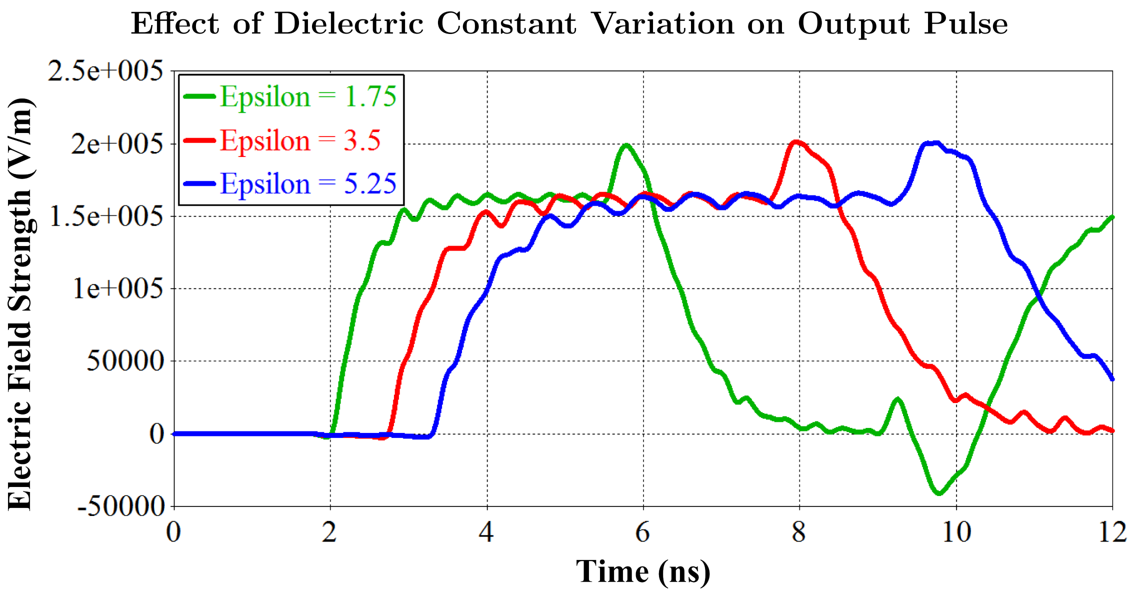

Figure 3.8: Comparison of transmission lines with three different dielectric constants.

### 3.1.4 Currents Generated

When a transmission is triggered, large currents are generated in the transmission lines. Figure 3.9 shows the current generated at the midpoint of a single transmission line in each conductive layer of the line, along with the gradient produced at the end of the line for a point of temporal reference. The currents generated in the top and middle lines, between which the excitation port is located, are equal in magnitude and opposite in sign. The current induced in the lower line is small; however, in a stacked geometry where this layer is a part of the subsequent transmission line, this line would conduct a current similar to that of the top line. At a 10 kV injection, these currents are approximately 5 kA - large, but lasting only a few nanoseconds. The current is then reversed in equal magnitude after the reflection of the pulse from the end of the line.

### 3.1.5 Line Width Variation

The width of the transmission lines is a key geometric component of the generated pulse. A series of simulations was performed to geometrically vary the width of the transmission lines to examine the impact of this dimension. In the CST Microwave Studio software,

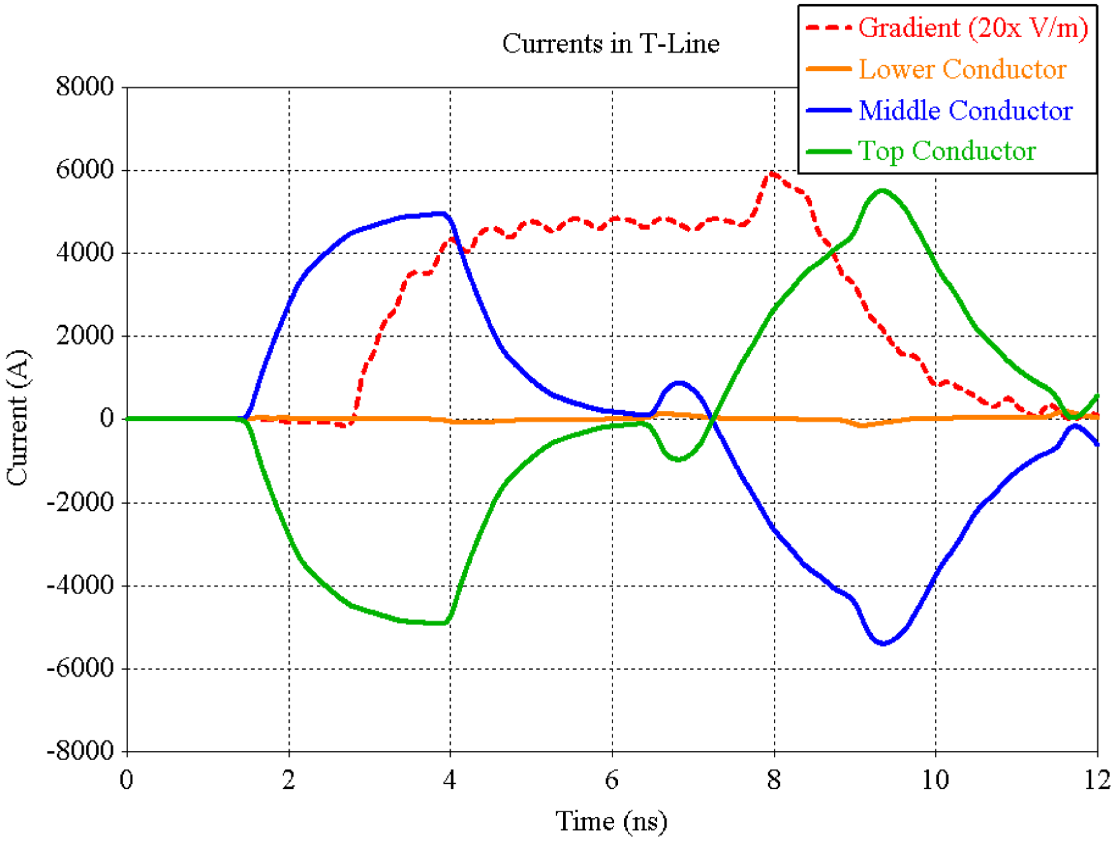

Figure 3.9: Currents generated in the top, middle, and bottom conducting layers at the midpoint of a single transmission line, along with the pulse shape of the gradient for reference purposes (scaled down by 95% for plotting purposes).

the width of the line was defined parametrically and swept across a series of values from 2 cm to 10 cm width. The resultant gradients produced 2.5 cm from the ends of the lines are shown in Figure 3.10. Most immediately clear is the difference in peak gradient. The fields propagating from the line termini fall off more rapidly as the lines become narrower, electrodynamically analogous to moving from a point to a line source of varying length. The returns from widening the lines diminishes after a point, however, and at 2.5 cm from the end of the lines, there is little gain from widening a line beyond 10 cm.

Two additional effects may be seen in Figure 3.10 as a result of widening the lines. Firstly, there is an increase in rise and fall times of the pulse with an increased line width. The slew rate of the rising edge of the pulse appears relatively constant, and the increased

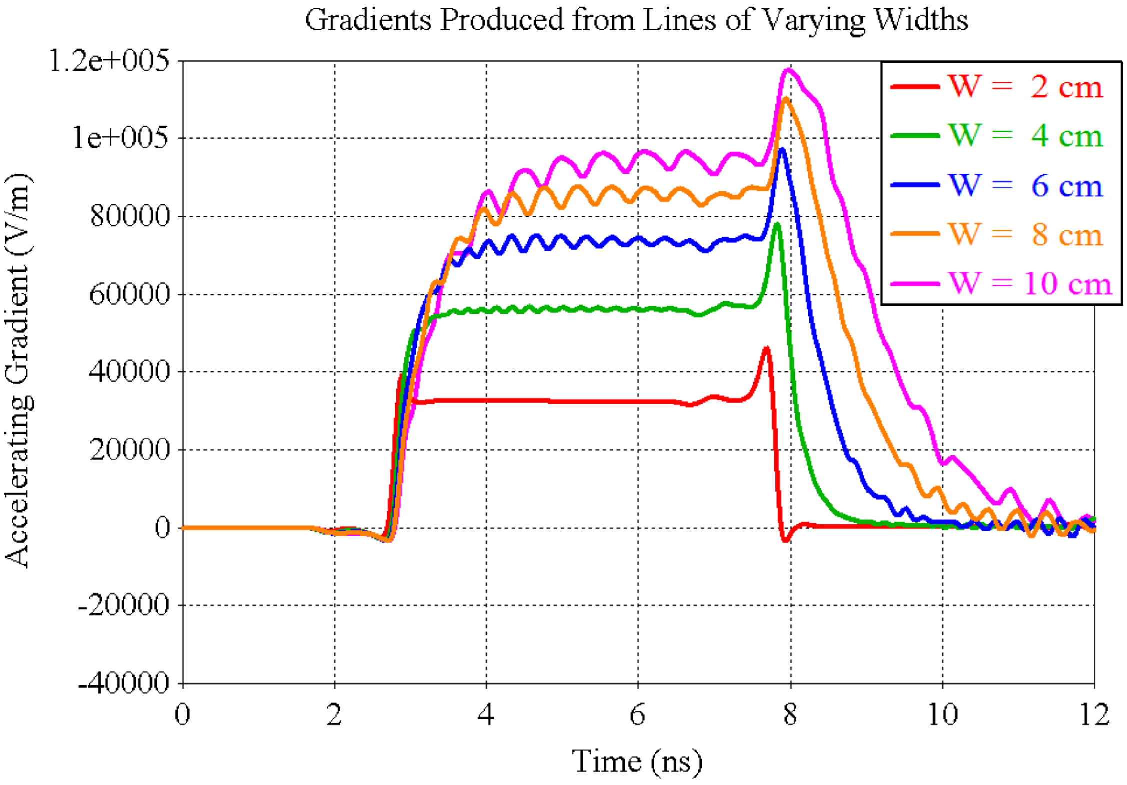

Figure 3.10: Z-component of the electric field generated 2.5 cm from the end of lines of varying width.

rise time corresponds to the higher ultimate peak height of the gradient. The pulse duration and fall time are also slightly impacted by line width; as a fast fall time is desirable due to the axial parasitic tail effect, line width choice (for a closing switch type excitation) is ultimately a trade-off between peak gradient and optimal pulse shape. Secondly, the ripple of each pulse increases and the frequency of the ripple decreases with a larger width. This indicates that the ripple is due to internal reflections within the width of the line, an effect further evidenced by the increasing ripple frequency with decreasing dielectric constant seen in Figure 3.8.

## 3.2 Matched Line Simulations

The addition of a symmetric, opposed line accomplishes two goals: increased accelerating gradient at the beam axis and a cancellation of the X component of the transverse fields shown in Section 3.1.1. For the basic transmission line geometry, addition of more than two matched lines brings a reduction of efficiency, as the width of the line must be greater than that of the beam pipe in order to transmit the greatest accelerating gradient to the beam axis. A geometry consisting of a single pair of matched, opposed transmission lines was constructed in order to asses the effect on the generated fields (Figure 3.11). For these simulations, the HGI beam pipe is ignored for the purpose of assessing the performance of the transmission lines in idealized terms. The dimensions and injection voltages of the additional line are identical to that of the first, and the lines are separated at the center by a distance of 5 cm for the following simulations.

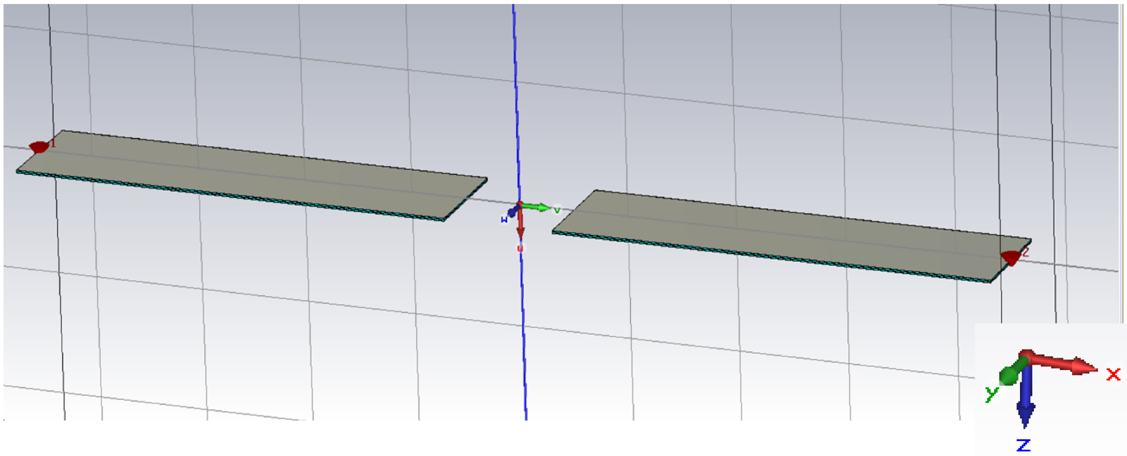

Figure 3.11: Geometry of a single matched pair of transmission lines.

### 3.2.1 Electric Fields Generated

Figure 3.13 shows the pulse generated by the matched line configuration at the center point between the two lines (2.5 cm from either line) in comparison with that of a single line in the same position, illustrating the doubling of the gradient. A qualitative plot of the gradient

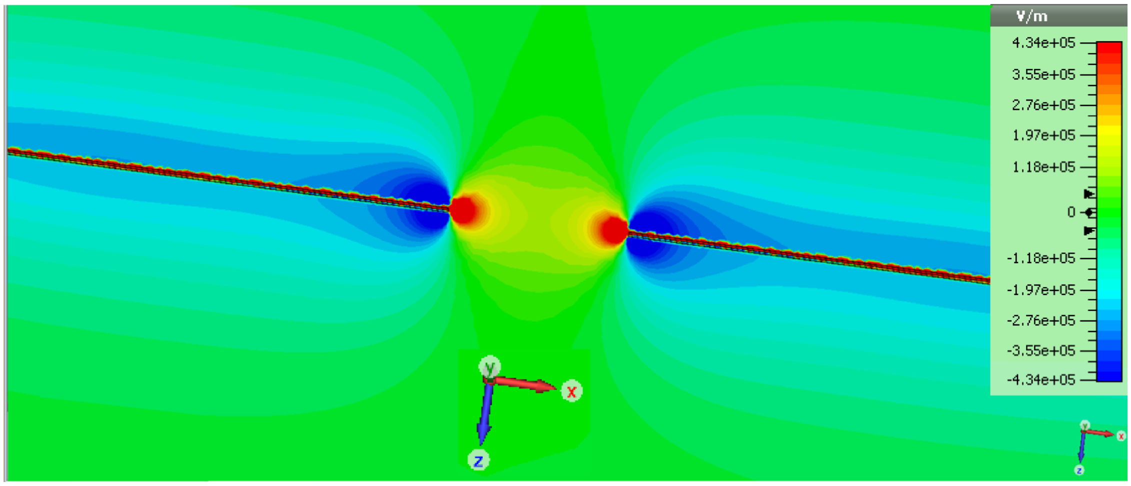

Figure 3.12: Accelerating gradient (Z-component of electric field, shown on the XZ cutplane) generated by a single transmission line pair.

produced by a pair of matched lines is shown in Figure 3.12. This image illustrates some effects described in the following sections. The impact of the matched line on the axial field is shown in Section 3.2.2. The accelerating gradient varies significantly in the region between the lines, an effect discussed in Section 3.2.3. Finally, significant fields are found above and below the line, which are the origin of the parasitic effect between lines further investigated in Chapter 4.

### 3.2.2 Axial Field Analysis

An axial field plot along the central axis between the two lines is shown in Figure 3.14. As expected, the large X component of the field is canceled out with the addition of the second line, while the Y component of the field remains negligible, and the magnitude of the Z component is doubled (relative to that of a single line, shown in Figure 3.5). However, while the X and Y components of the fields are eliminated at the central axis, each has a significant magnitude at axes off the central axis.

Figure 3.15 shows the Y component of the field in the matched line geometry. Moving further from the axis (while remaining between the two lines) yields increasing electric fields in this direction. The X component of the fields as you move in this direction remains

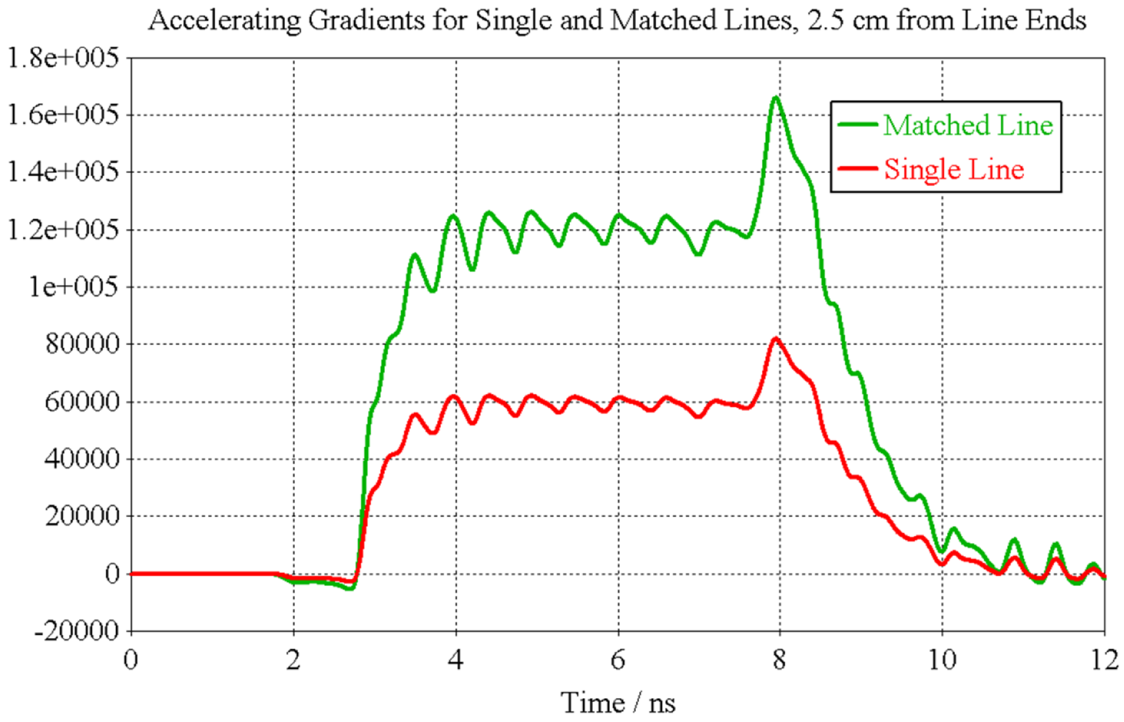

Figure 3.13: Z-component of the electric field generated by two matched lines and a single line.

negligible due to the canceling effect of the symmetry and is not shown. Similarly, Figure 3.16 shows the X component of the fields at various distances off the central axis in the X direction. In both cases, these off axis fields are smallest close to the beam axis, implying that the cross section of the beam itself should be small to minimize the impact of these off axis fields. However, their deleterious impact is somewhat alleviated by the fact that they alternate in direction above and below the line: for a given particle trajectory, both regions are experienced so the net force imparted to the particle in those directions is greatly reduced. Furthermore, the accelerating, Z component of the field is still much greater than these off axis components, and the particles will be traveling at high enough velocities (assuming sufficient injection energy) that the duration they experience any given off-axis field will be very short.

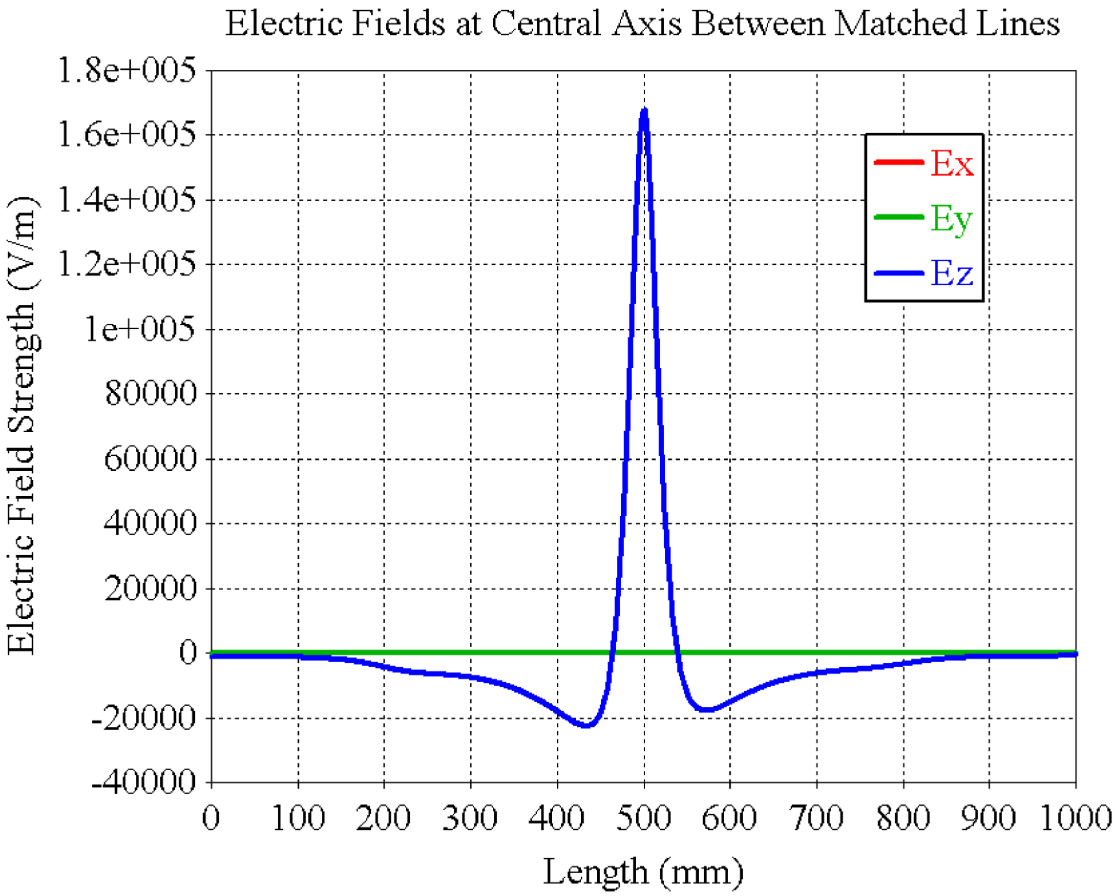

Figure 3.14: Electric fields generated at the central axis between two transmission lines during a pulse. Note the complete cancellation of the X and Y components.

### 3.2.3 Transverse Field Analysis

The accelerating gradient across the region between the lines has a bowl-like shape, as the magnitude of the electric field rapidly falls off with distance from the end of each of the lines. For the separation distance of 5 cm, the effective gradient at the center of the beam axis is over an order of magnitude smaller than that of the end of the lines (Figure 3.17) - this emphasizes the need to minimize the radius of the beam pipe to maximize the gradient that reaches the ions to be accelerated. A wide, flat region across the center of the axial region is well suited to particle acceleration, as the particles will experience a reasonably similar gradient when within this region, and thus be accelerated at the same rate.

However, when looking more closely at the central region of the beam pipe, there is still

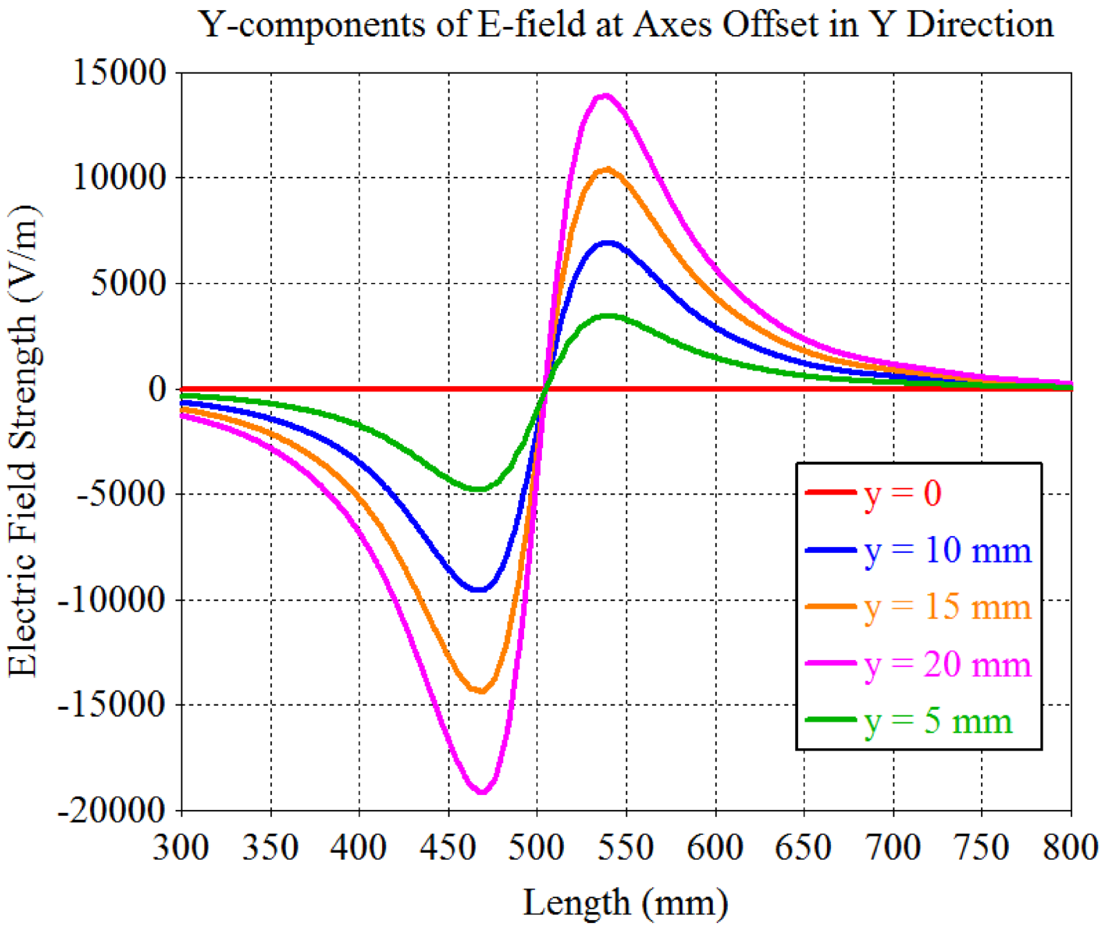

Figure 3.15: Y-component of the axial gradients generated by a single transmission line for various displacements in the Y direction.

a significant variation of field strengths. Figure 3.18 shows the central 2 cm section of the transverse plot shown in Figure 3.17. The outer regions have a gradient that is approximately 30% greater than that at the absolute center of the beam pipe. The impact of this difference on a particle bunch is described more fully in Chapter 5, but in short, particles nearer the transmission lines are preferentially accelerated. This discrepancy in acceleration may be accounted for by temporally shaping the accelerating pulse through various geometries, discussed further in Chapter 6.

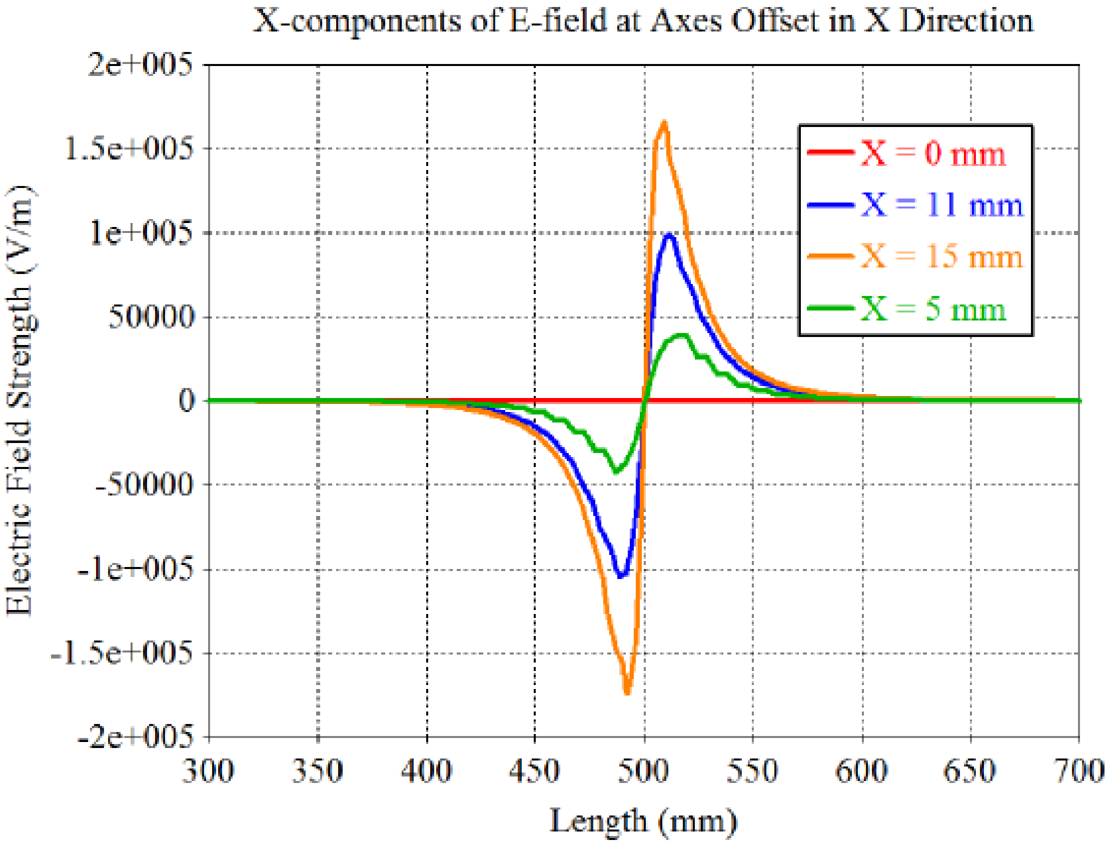

Figure 3.16: X-component of the axial gradients generated by a single transmission line for various displacements in the X direction.

## 3.3 Inclusion of Beam Pipe

While the previous simulations have excluded the beam pipe for the purpose of examining the pure performance of the transmission lines, in practical terms, the beam pipe is essential and will have an impact on the fields that ultimately reach the particle bunch. The following simulations incorporate the beam pipe in two ways. First, a beam pipe constructed of purely dielectric material is considered. Second, a beam pipe with the interleaved conductor-insulator structure of HGI material is investigated. Both types of beam pipe geometry are compared with a geometry containing no beam pipe.

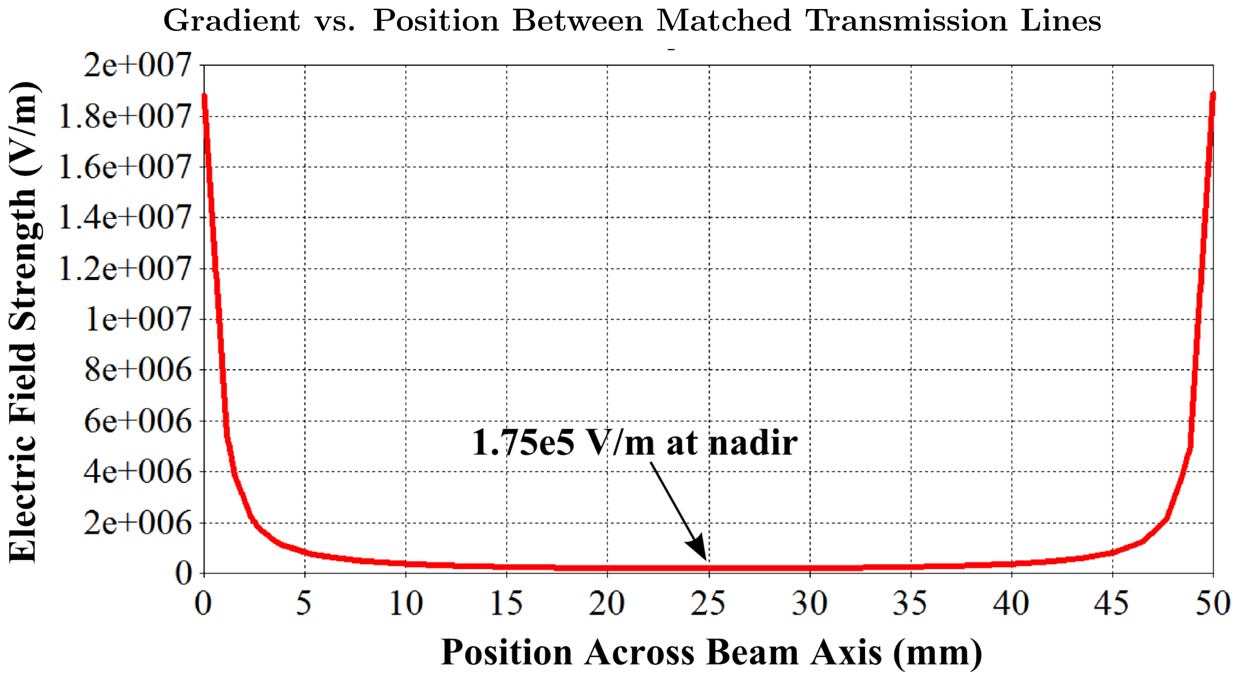
Gradient vs. Position Between Matched Transmission Lines

Figure 3.17: Accelerating gradient (Z-component) of electric fields across the region between a pair of matched transmsission lines.

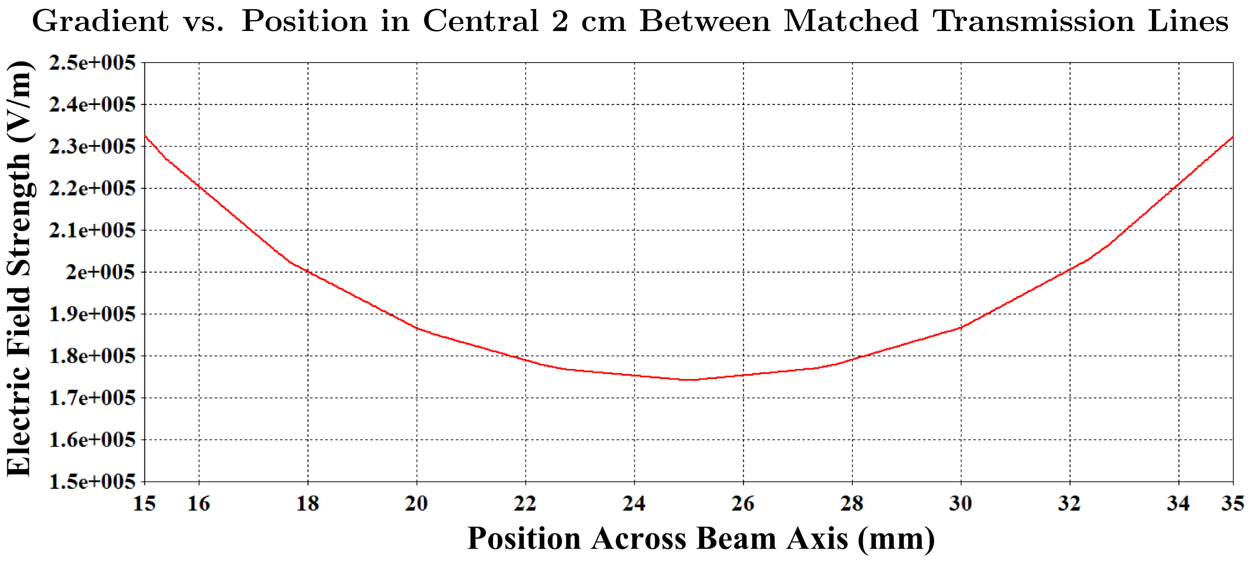
Gradient vs. Position in Central 2 cm Between Matched Transmission Lines

Figure 3.18: Accelerating gradient (Z-component) of electric fields across the region between a pair of matched transmsission lines. This plot shows just the central 2 cm of the inter-line region. Note that the field at the center is roughly 30% lower than that at the edges.

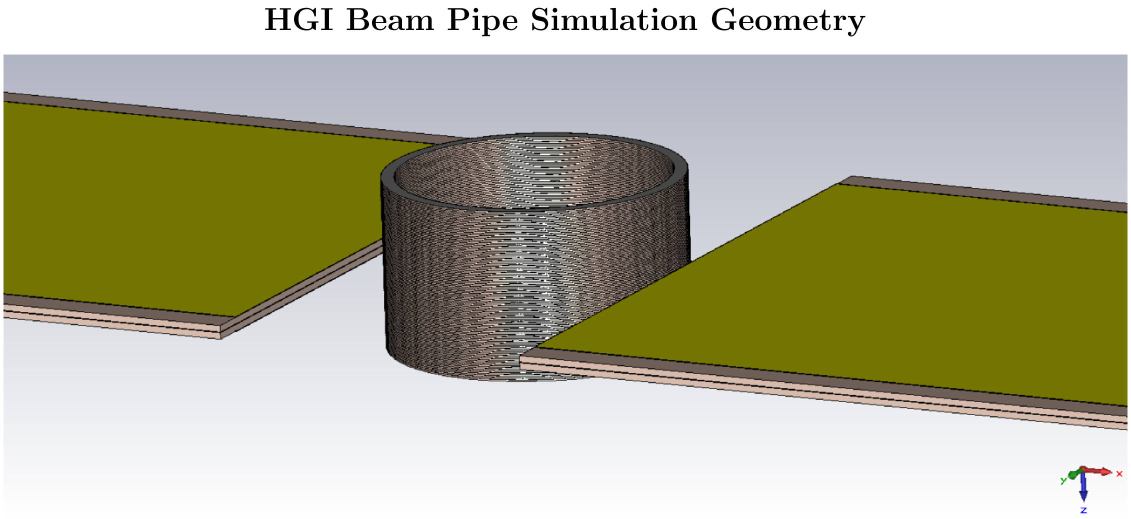

Figure 3.19: Simulation geometry for HGI beam pipe simulation.

### 3.3.1 Pure Dielectric Beam Pipe

A simulation utilizing the geometry and excitation parameters described in Section 3.1.1 with the addition of a beam pipe consisting of pure dielectric material was designed. The dielectric material chosen was Rexolite®, a cross-linked polystyrene possessing a dielectric constant of 2.53 and a dielectric strength of 2.1 MV/m commonly used in the construction of HGI materials [72]. The outer radius of the beam pipe was defined 1 mm from the end of the matched transmission lines, the diameter of the beam pipe was 2 mm thick, and the spacing between the transmission lines remained 5 cm. This geometry was compared with a benchmark simulation containing a region of pure vacuum between the lines by setting the beam pipe material to vacuum. An additional simulation was performed with a pure insulator beam pipe with twice the dielectric constant of Rexolite®.

### 3.3.2 High Gradient Insulator Beam Pipe

The high breakdown strengths of high gradient insulators have made them particularly interesting for DWA applications. The addition of conducting layers to the beam pipe significantly changes the way the fields propagate to the beam axis. A geometry consisting of the above parameters was constructed with the exception of replacing the beam pipe with an HGI stack. The thicknesses and materials of the HGI stack were chosen to coincide with the best performing sample in published data. As such, the insulator material chosen was Rexolite® with a thickness of 0.254 mm, while the conductor chosen was stainless steel with a thickness of 0.013 mm [4]. The thickness of the beam pipe was chosen to be 2 mm with an outer radius beginning 1 mm from the end of the transmission lines as in the pure dielectric simulation. A schematic of the simulation geometry is shown in Figure 3.19.

### 3.3.3 Impact of Beam Pipe Inclusion

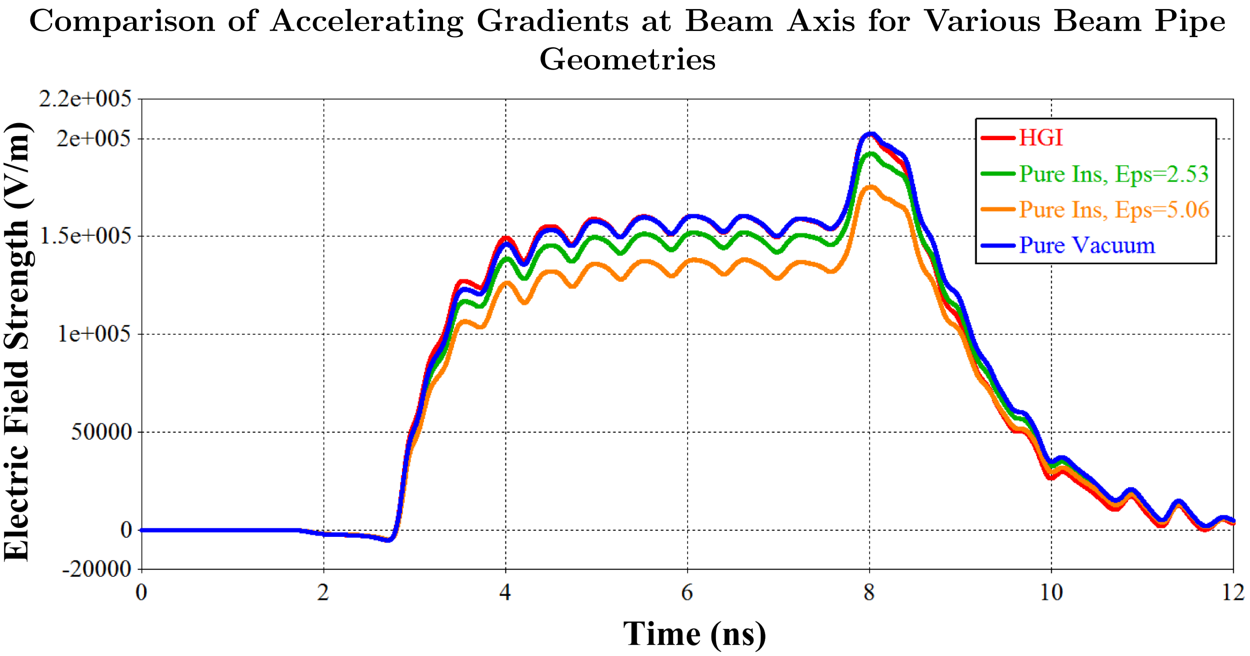

Figure 3.20: Accelerating gradient for various beam pipe materials, along with the beam pipe excluded.

A plot of the field strengths for the pure dielectric, pure vacuum, and HGI geometries is shown in Figure 3.20. The pure dielectric beam pipe has a dampening effect on the pulse, such that the gradient is decreased as the dielectric constant of the beam pipe increases. The addition of the HGI beam pipe, however, does not degrade the pulse height in this geometry. This can be attributed to the fact that the layered conductors of the HGI geometry effectively

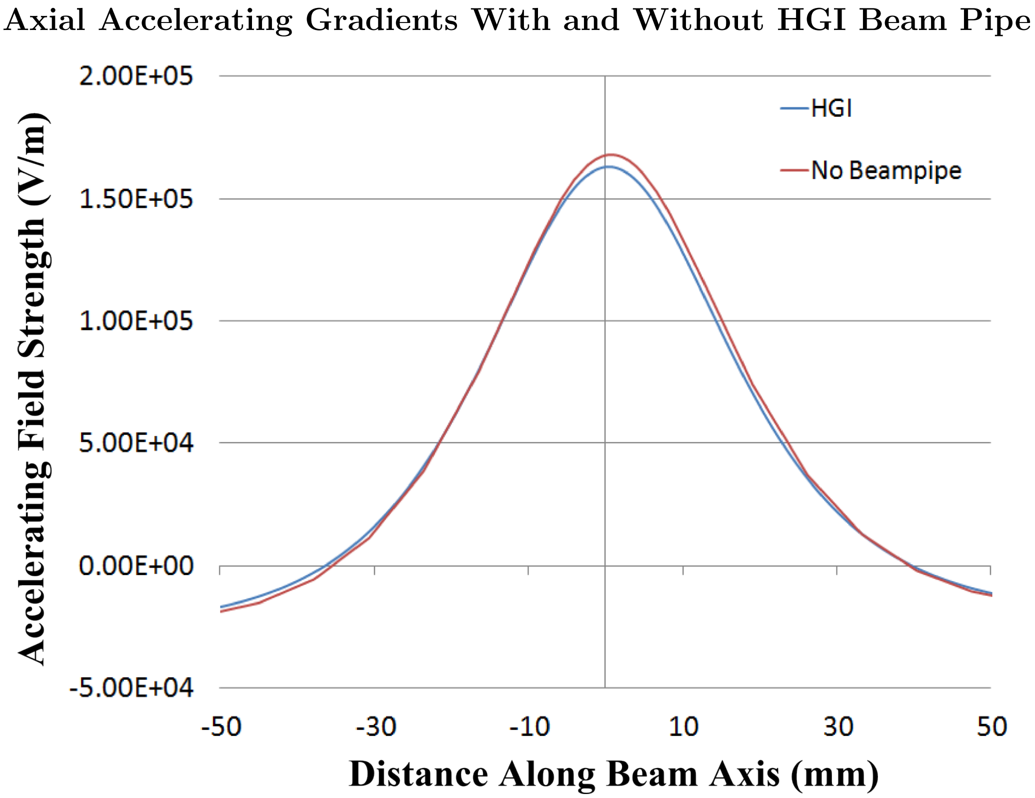

Figure 3.21: Accelerating gradient along a curve corresponding to the central axis of the beam pipe with and without HGI beam pipe.

direct the pulse closer to the beam axis and mitigate the rapid gradient fall-off from the end of the lines observed in Section 3.2. This effect can be observed in Figure 3.22 - note that the dampening effect of the field propagation in the pure dielectric case may also be seen in the field fall-off within the beam pipe.

An additional effect of adding the HGI beam pipe is propagation of the fields around the beam pipe itself. The layered conductors and insulators of the HGI transport the fields in a way similar to many “micro” transmission lines and cause significant fields on the cutplane between the lines (see Figure 3.23). The impact of this effect on the axial gradient along the beam axis is illustrated in Figure 3.21 and is seen to be minimal.

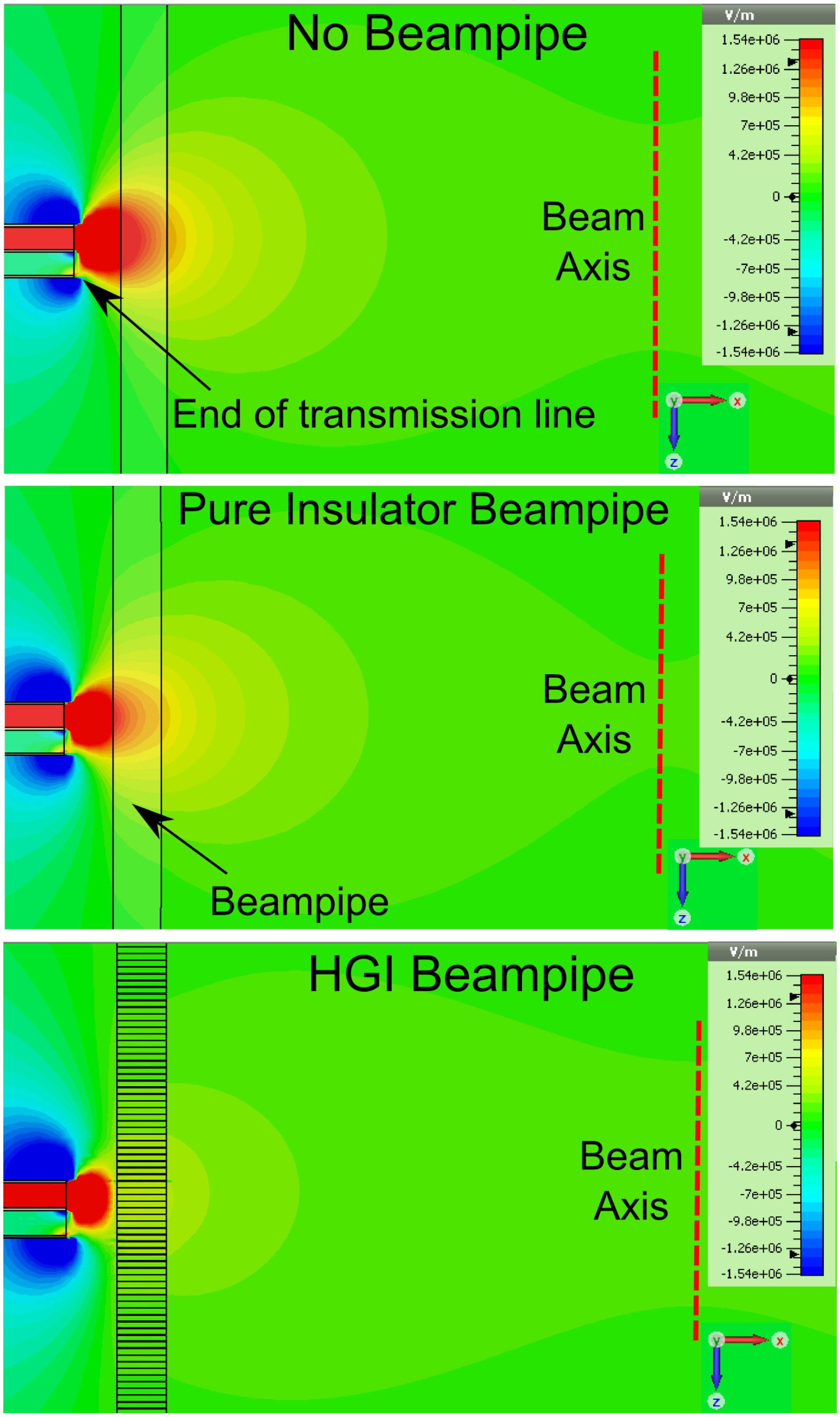

Figure 3.22: Z component of the electric fields in the vacuum (no beam pipe), insulator, and HGI beam pipe geometries. Identical scaling was used for each image.

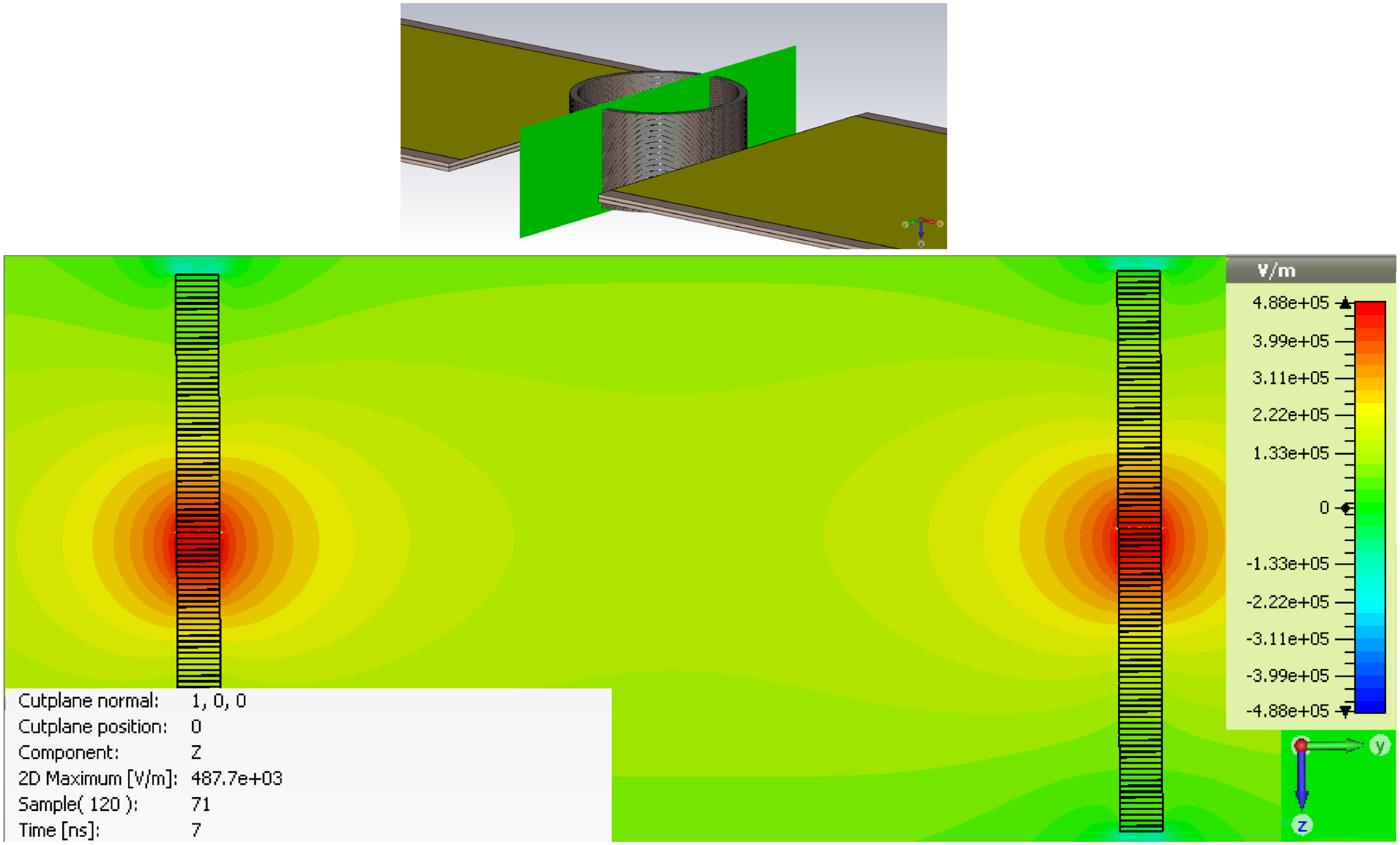

Cutplane normal: 1, 0, 0
Cutplane position: 0
Component: Z
2D Maximum [V/m]: 487.7e+03
Sample( 120 ): 71
Time [ns]: 7

Figure 3.23: (Top) X-Z cutplane through the HGI beampipe. (Bottom) Z component of the electric fields in the X cutplane through the HGI beampipe. Scaling has been adjusted relative to Figure 3.22.

## 3.4 Pulsed Voltage Input

Having characterized the lines for an idealized closing switch, we can now inspect the impact of injecting a pulsed voltage into the pair of matched transmission lines. Using the previously defined benchmark line geometry, two different pulsed excitation voltages were simulated with hold times at the peak voltage of 100 ps and 1 ns. For the sake of comparison, the magnitude of the voltage is still 10 kV; however, there are commercially available pulsers with similar output shapes that operate at 10s of kV.

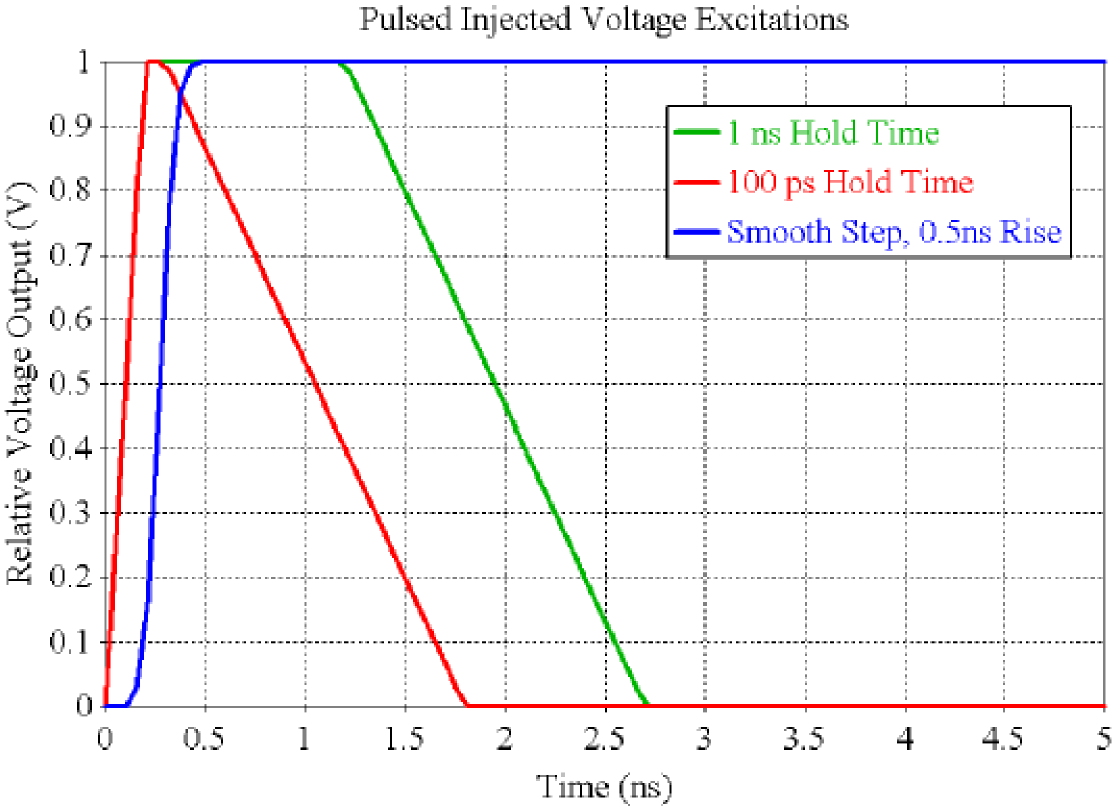

Figure 3.24: Excitation signals used for pulsed voltage output simulations.

Not surprisingly, the short pulsed voltage injections produce a gradient that are temporally shorter than the excitation produced by the smooth step signal (Figure 3.25). For both pulsed injections, the duration that the gradient is within 10% of the peak value is on the order of a nanosecond. While this pulse duration is much shorter than the pulse duration of the smooth step defined by Equation 2.2, this pulse shape is still suitable for accelerating

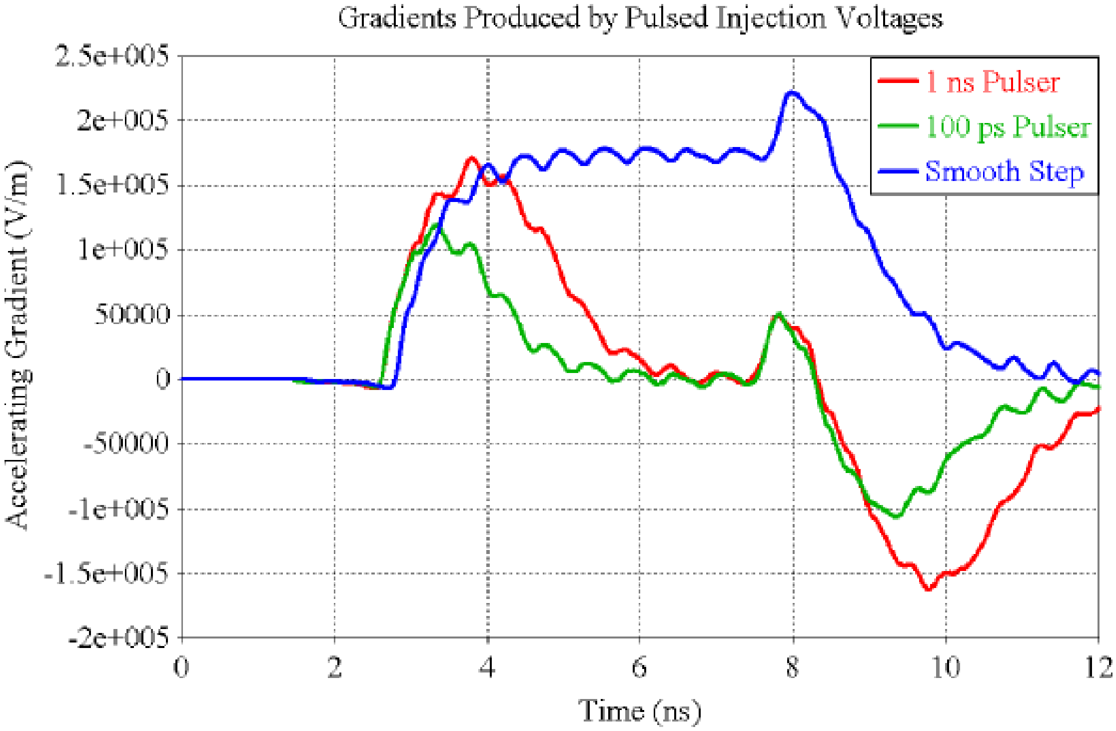

Figure 3.25: Gradients produced 2.5 cm from the end of a transmission line for two different pulser-type excitations, along with the smooth step pulse representing a closing switch.

protons since the temporal length of the pulse as required for proton therapy applications is only 300 picoseconds. Another effect of note is that the gradient generated by this pulser becomes negative after the initial accelerating pulse, and the parasitic tails of the axial fields become accelerating, which will help to slightly offset other parasitic behaviors (Figure 3.26). These axial parasitic tails of the pulser are also observed to have a magnitude about a factor of two smaller than those generated by the smooth step/closing switch excitation.

Figure 3.27 shows the currents generated within a transmission line receiving a pulsed voltage injection. These currents are smaller than those generated by the smooth step closing switch excitation shown in Figure 3.9 which peak at 5 kA. Like the smooth step case, the initial reflection is opposite in polarity and equal in magnitude to the first. The second reflection, in contrast, begins with a negative magnitude before returning to the initial polarity. This second set of reflection generates the second, negative gradient pulse.

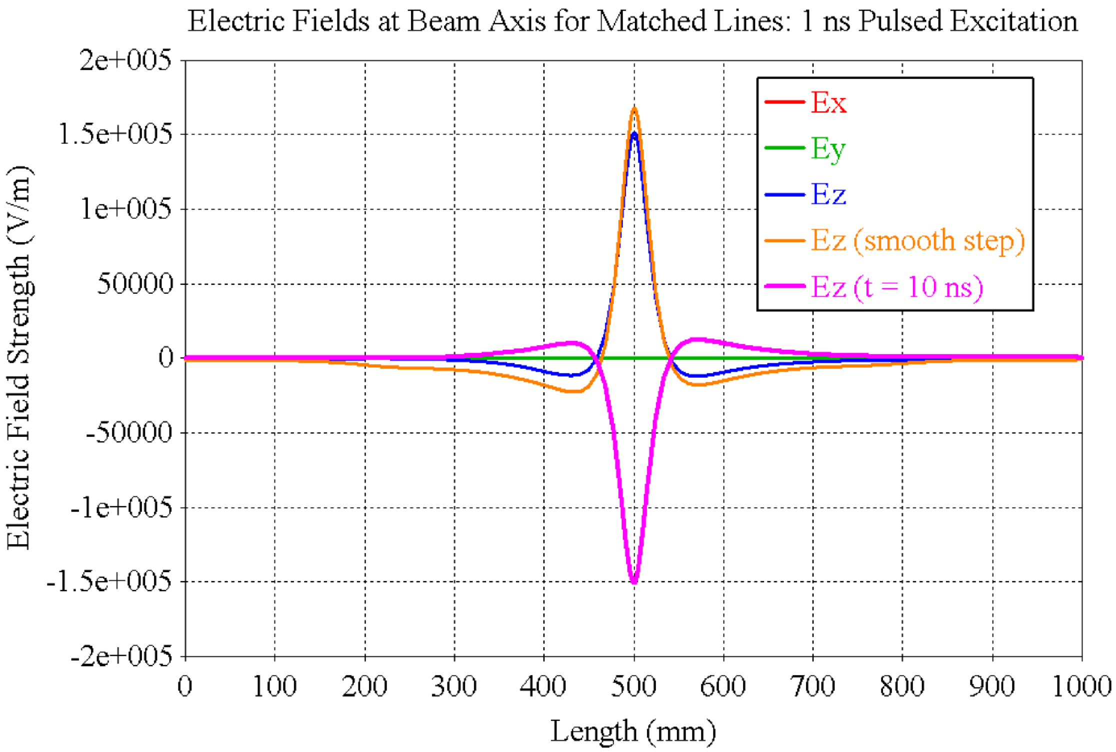

Figure 3.26: Electric fields generated by a 1 ns pulsed excitation during the pulse, along with the Z-component during the reflected pulse (at t= 10 ns) and that of a smooth step excitation during the pulse.

## 3.5 Hardware Transmission Line Verification

In order to verify the simulations, a simple test transmission line was constructed. The layers of the transmission lines were built using Pyralux® AP Plus AP7378R, a copper clad laminate available from DuPont. Each sheet consists of 305 $\mu$m of Kapton® dielectric bonded to 70 $\mu$m of copper [73] on either side. To create layers similar to the above simulated transmission lines, the sheets were cut into three lines 50 cm in length and 10 cm in width. For the purposes of electrically connecting to the lines, two of the lines had 1 cm by 1 cm tabs on the switching end. In this way, a transmission line with three conducting layers and three insulating layers (one of which is not used) is formed. A fast delay generator (9530 Digital Delay Pulse Generator from Quantum Composers®, Inc.) was used to inject a voltage pulse across the two tabs, and this voltage pulse was imported into CST Microwave Studio to

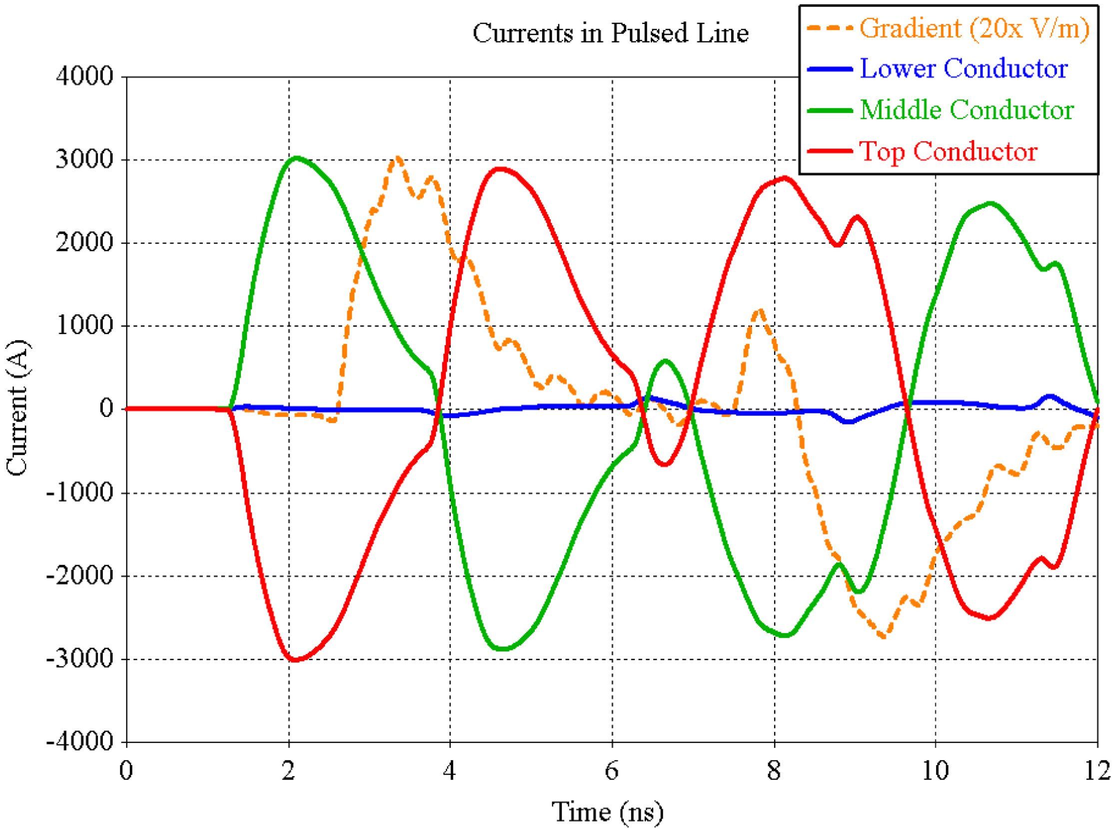

Figure 3.27: Currents generated in the top, middle, and bottom conducting layers at the midpoint of a single transmission line receiving a pulsed voltage injection, along with the pulse shape of the gradient for reference purposes (scaled down by 95% for plotting purposes).

serve as the excitation pulse for a simulation matching the physical geometry (Figure 3.29). The lines were compressed with custom machined mounting brackets made of Delrin®, an acetal polymer produced by DuPont; no extra dielectric or conductive adhesive was used. This method of compressing lines with Delrin® has also been used in experiments in the literature [38]. The voltage output of the pulse generator and at the end of the lines was measured using a Tektronix® DPO7354 3.5 GHz oscilloscope. Figure 3.28 shows a rendering and photograph of the experimental setup.

The injected voltage pulse is shown in Figure 3.29. The parameters of the pulse were chosen to give the shortest possible rise time and a pulse shape similar to that of a fast pulser or shock line. The rise time of the pulse, defined as the time taken for the pulse to reach from 10 % to 90% of its maximum value, is 2.7 ns. The duration of the pulse, defined to

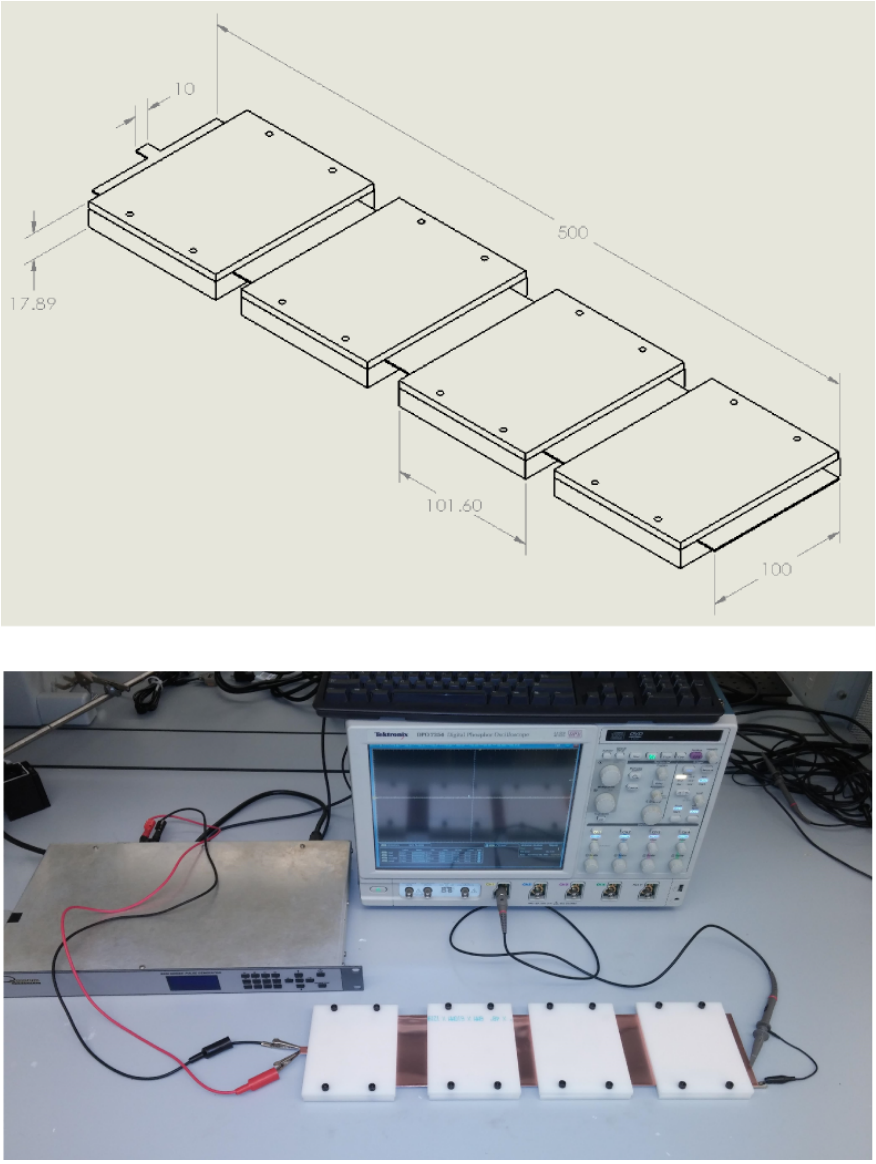

Figure 3.28: 3D rendering of transmission line assembly (top) and photograph of experimental setup (bottom).

be its full-width half-maximum, is 5.71 ns. These pulse parameters are near the limit of the pulse generator's speed. In order to minimize the rise time, the amplitude of the pulse was actually set to 5 V (in TTL mode), though the pulse length was set to be very short, such that the magnitude of the output only reached the 400 mV shown in Figure 3.29 before the pulse was turned off. This was found to slightly increase the voltage slew rate of the generator (and correspondingly reduce the rise time of the pulse). However, because of this

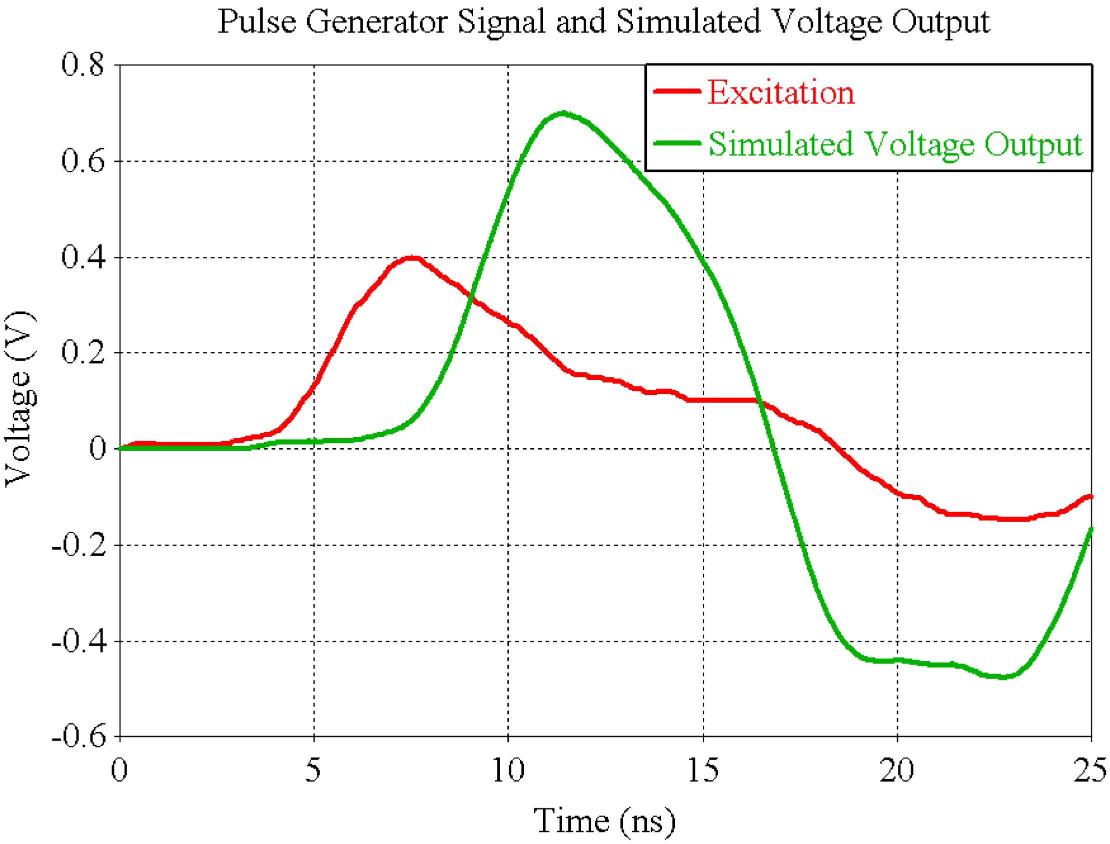

Figure 3.29: Voltage output measured from pulse generator with the simulated voltage output.

method, the pulse height is significantly impacted by the 50 ps jitter of the generator [74], resulting in a variation of output on the order of 10-20 mV pulse-to-pulse and some pulse shape distortion.

The magnitude of the output pulse is also impacted by the impedance matching of the system. The output impedance of the pulse generator is 50 Ω, while the impedance of the transmission line (given by Equation 2.3) is 1.23 Ω, resulting in a transmitted pulse of only 4.79% of the injected voltage according to Equation 2.5. This is acceptable, as the primary goal of this experiment was designed to examine pulse shape rather than efficiently power the lines.

The output of the transmission line, superimposed with the simulated output, is shown in Figure 3.30. As the excitation signal was measured (and imported to the simulation software)

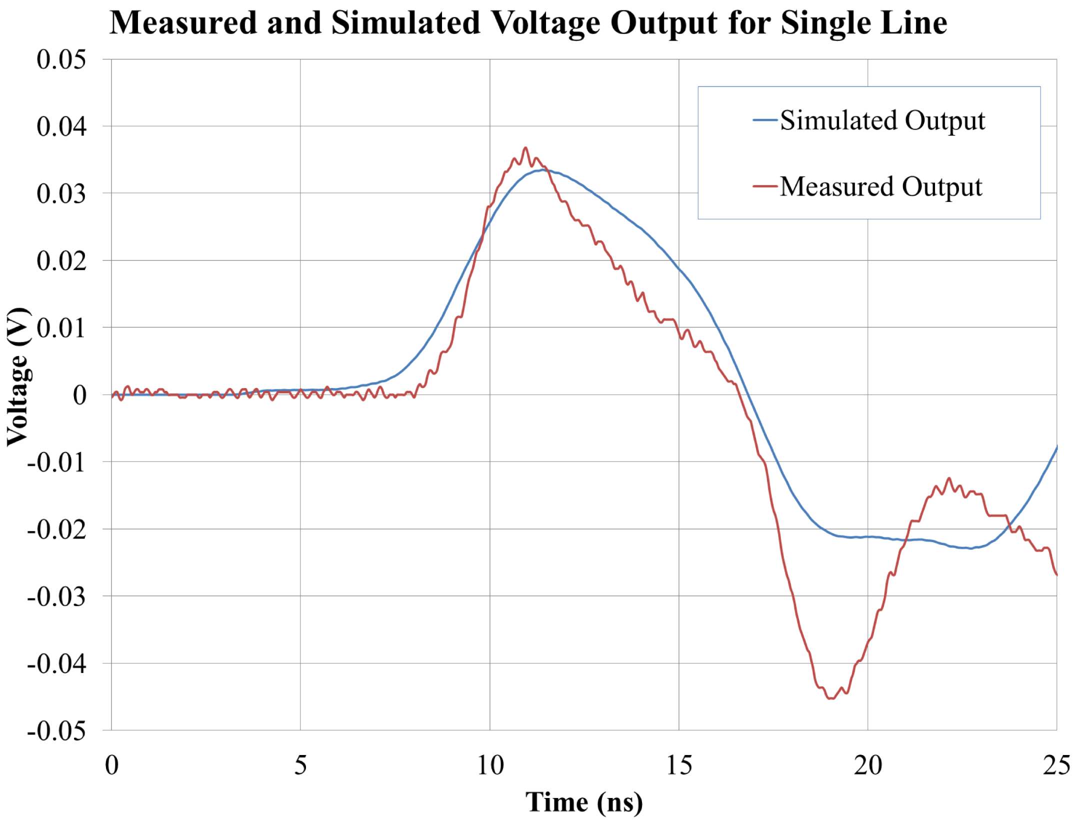

Figure 3.30: Simulated and measured voltage output for the single transmission line experiment. The simulated output has been scaled by the transmsission coefficient of the transmission line.

prior to the line, the simulated voltage output was scaled by the transmission coefficient of 0.0479. The magnitudes measured and scaled simulated pulses show good agreement with the simulated value within 5% of the measured value. The differences in the shapes may be attributed to the aforementioned output variation of the pulse generator or imperfect coupling between the lines (Figure 3.31).

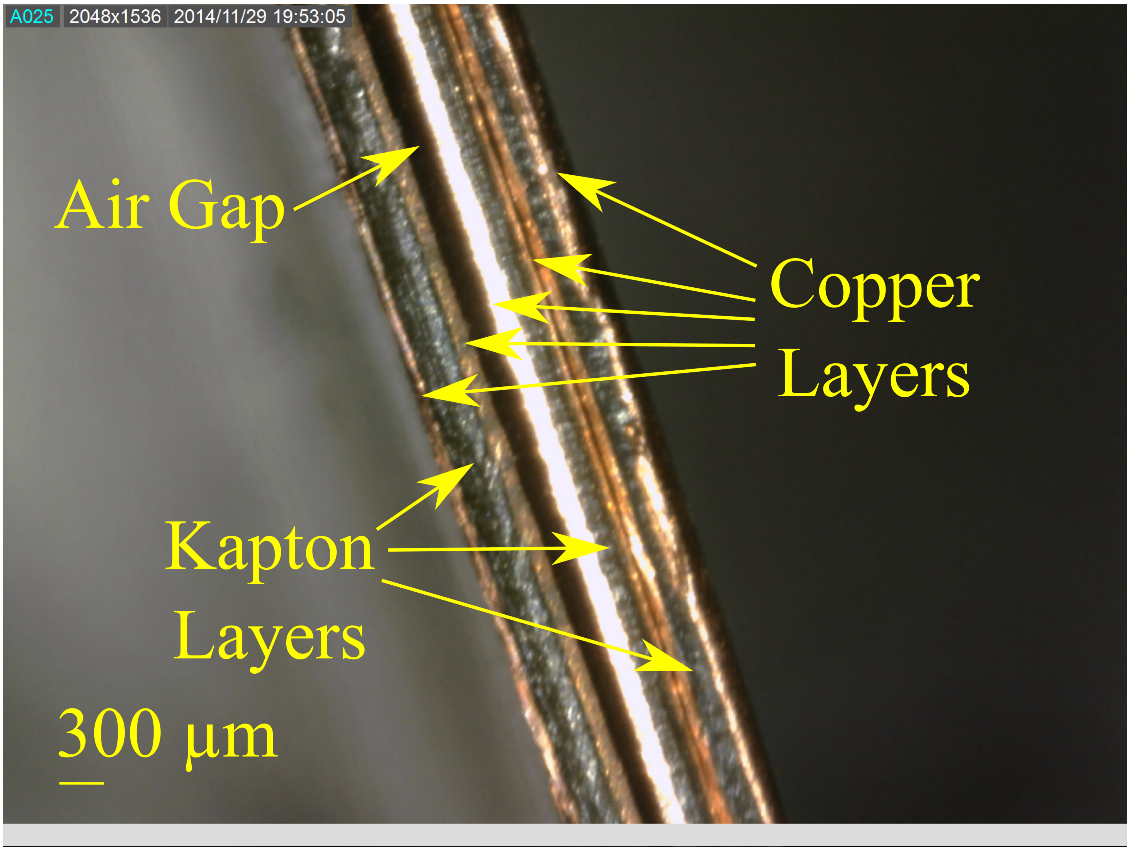

Figure 3.31: Magnified image of the edge of the experimental transmission lines. Note the imperfect coupling between the left and center line.

# Chapter 4

# Characterization of Stacked Transmission Lines

## 4.1 Introduction

Having described and characterized the behavior of individual lines, we may assess their behavior in a stacked configuration conducive to use in an accelerator, since in order to create an accelerating pulse that spatially includes the entire particle bunch along the beam axis, it will be necessary to fire several transmission lines at once. A number of stacks with varying dimensions and excitation parameters have been simulated, and selected results are shown below. In order to fully understand the impact of neighboring transmission lines, the firing of an individual line immediately surrounded by other lines is compared both to a single line with no neighboring lines and the simultaneous firing of a stack of several transmission lines.

The influence of stacked lines on each other is of particular importance due to the observed parasitic effect between the lines. This parasitic effect has been found to be one of the limitations of efficiency of the stacked transmission line geometry in the dielectric wall accelerator [6]. This effect, illustrated in Figure 4.1, occurs due to the inductive fields generated between the lines and will be investigated in the following chapter.

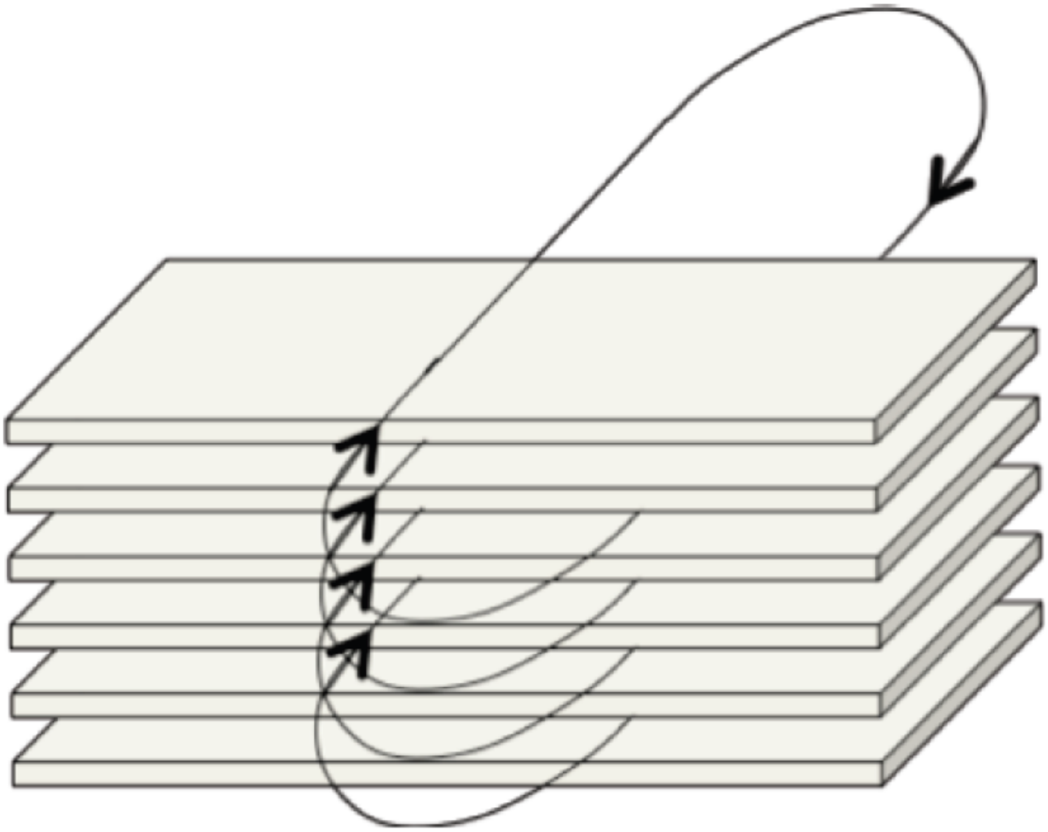

Figure 4.1: Schematic illustrating the parasitic induced currents in stacked transmission lines. Figure from Caporaso, 2009 [6].

## 4.2 Stacked Simulation Methods

The impact of neighboring transmission lines on the behavior of a single line is assessed by simulating a stack of transmission lines where only a single line is fired. The impact on the pulse properties may then be compared to the behavior of a bare line. The geometry of each line is the same as the benchmark geometry described in Section 3.1.1 such that the individual lines are 40 cm by 10 cm, with 1 mm thick insulator layers. A stack of five identical lines was constructed such that the bottom layer of one line is the top layer of the subsequent line (Figure 4.2). This stack of lines was excited at 10 kV via an edge excitation port with a 0.5 ns rise time smooth step function under the following conditions:

**Case 1** All five lines contain edge ports and are simultaneously fired.

**Case 2** All five lines contain edge ports and are individually fired.

**Case 3** Only the center line contains an edge port (as the ports themselves act as wires when not excited).

**Case 4** Only the center line is present, acting as a single line surrounded by vacuum.

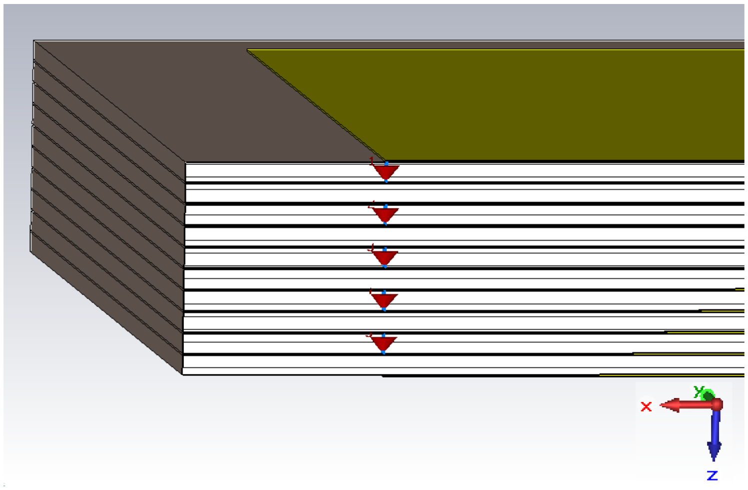

Figure 4.2: Switching side of the geometry used in stacked transmission line simulations, with ports on each of the five transmission lines.

Additionally, single and matched stacks of 50 transmission lines (giving a total height of 11.01 cm) was simulated. Each line simultaneously received a 10 kV injected voltage, as above, with voltage monitors at the end of each line. To analyze the pure behavior of the stacked lines, the beam pipe was omitted.

## 4.3 Stacked Simulation Results and Discussion

### 4.3.1 Five Line Stack

Images of the gradients generated by the stacked lines in a 2D X-Z cutplane at the midline of the transmission lines in Cases 1, 2, and 3 are shown in Figures 4.4, 4.5, and 4.6, respectively

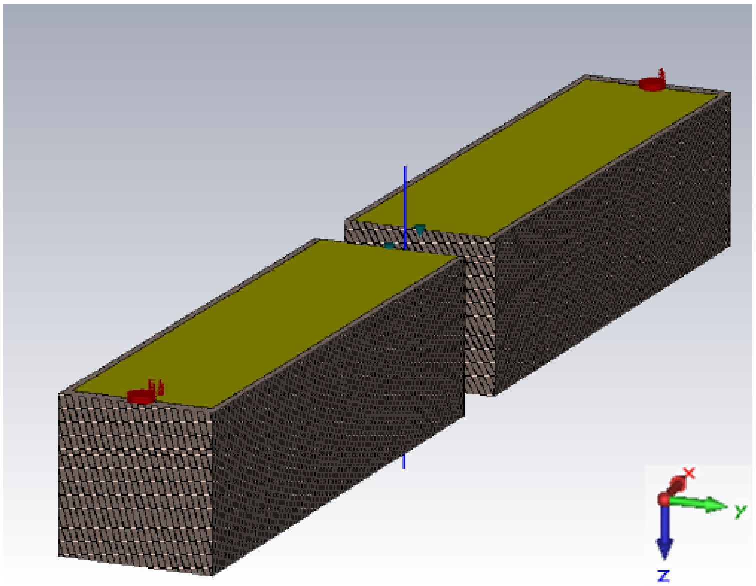

Figure 4.3: Geometry of the 50 line matched stack, where the blue line indicates the beam axis.

- note that the scaling differs between Figure 4.4 and Figures 4.5 and 4.6, as the gradients are much higher when the lines are simultaneously fired. Each image was taken at the same time step in their respective simulations - 7 ns from the start of the simulation and during the top of the flat top of the pulse.

### Parasitics

Examining Figures 4.5 (Case 2) and 4.6 (Case 3), we see the impact of firing of a single line on neighboring lines. In both Cases, fields are induced in neighboring lines; the difference is that in the Case where each line possesses a port, the field strengths in the Z direction are alternating between positive and negative, but while when they are not connected by ports, the fields within neighboring lines are all in the negative Z direction within each adjacent line, with the magnitude of the field decreasing in layers further from the triggered line. This is due to the ports being considered wires when not receiving an excitation input - while in practice each line would contain a voltage port, it is interesting to observe the propagation of these parasitic fields in their absence. In both cases, the maximum induced field strength within the non-firing lines is approximately 500 kV/m; in comparison, the maximum field

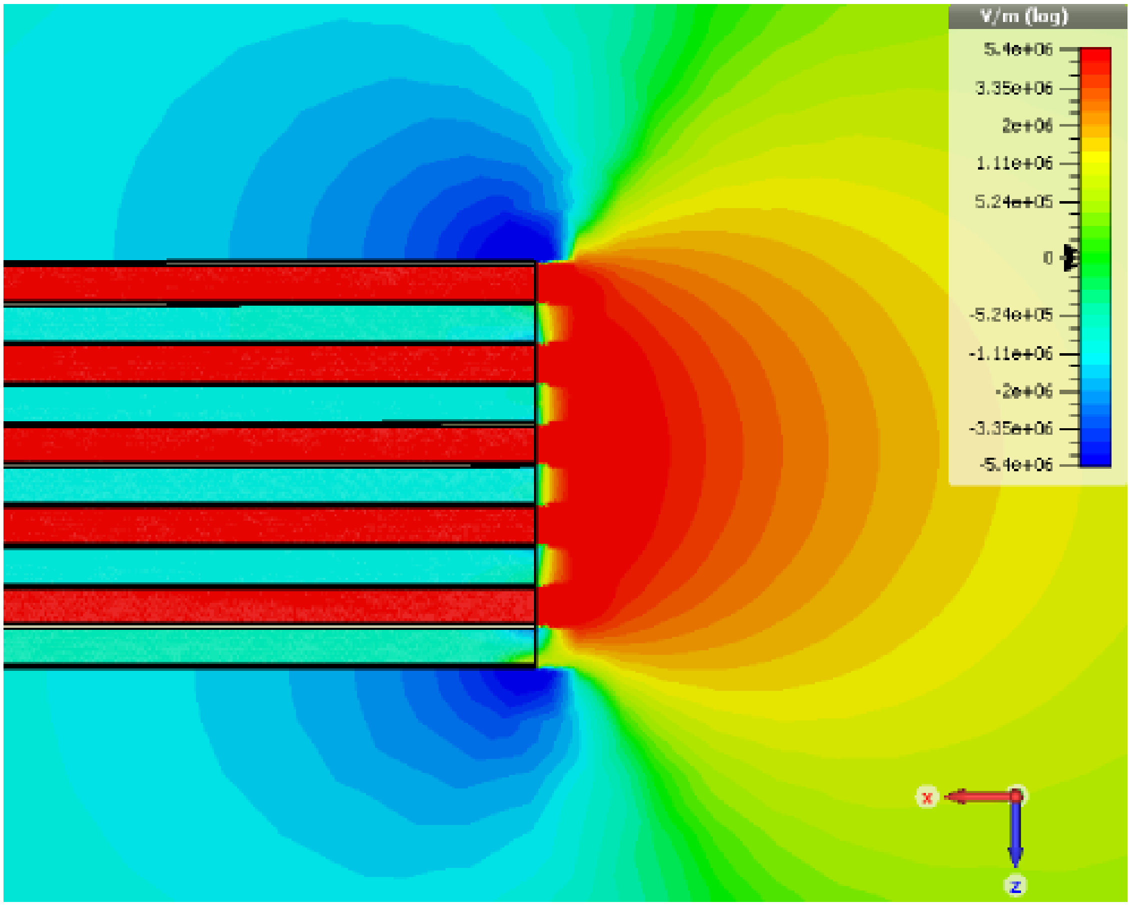

Figure 4.4: Accelerating gradient (Z component of the electric field) in the XZ cutplane produced by firing all 5 lines simultaneously (Case 1).

within the triggered line is 54 MV/m.

The impact of these induced fields may be inspected by defining a voltage monitor at the end of each line. Figure 4.7 shows the voltage output generated in neighboring lines when the bottom line alone is fired. While these voltages are small relative to the output voltage of a given line, similar voltages are produced by each triggered line in its neighbors. When simultaneously fired, it is the sum of these parasitic induced voltages that draws down the voltage output. Figure 4.8 shows the voltage output of each line when simultaneously fired along with the voltage output of a bare line. In this Case, the voltages in each line of the stack are very similar, and in all Cases about 5% smaller than those of the bare line. A more dramatic change in voltage output with position in the stack will be found in the Section

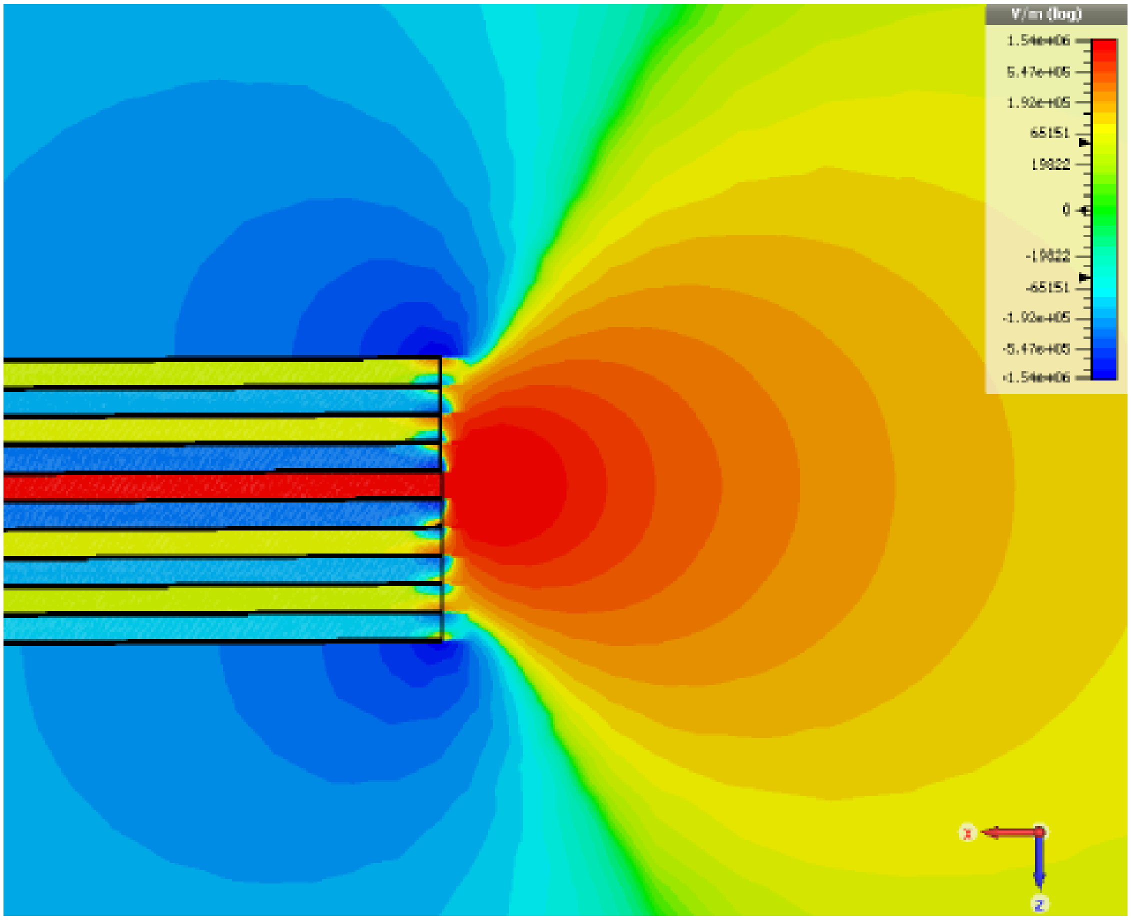

Figure 4.5: Accelerating gradient/Z-component of the electric field produced by firing the central line while the other lines are connected by ports (Case 2).

4.3.2 within the discussion of the 50 line stack.

### Axial Fields

When considering the cutplane image of the gradients in the simultaneously fired stack in Figure 4.4, it appears that the propagation of the fields from the stacked, simultaneous firing of the lines is quite similar to that of a single line. Indeed, the axial gradient 1 cm from the end of the stack (Figure 4.9) possesses a shape similar to that of a single transmission line. Due to superposition, the gradient of the stack of five simultaneously fired lines is the sum of each line fired individually. An additional observed effect is the summing of the negative tails of the axial gradient. While individual lines each reach -25 kV/m to -35 kV/m, the

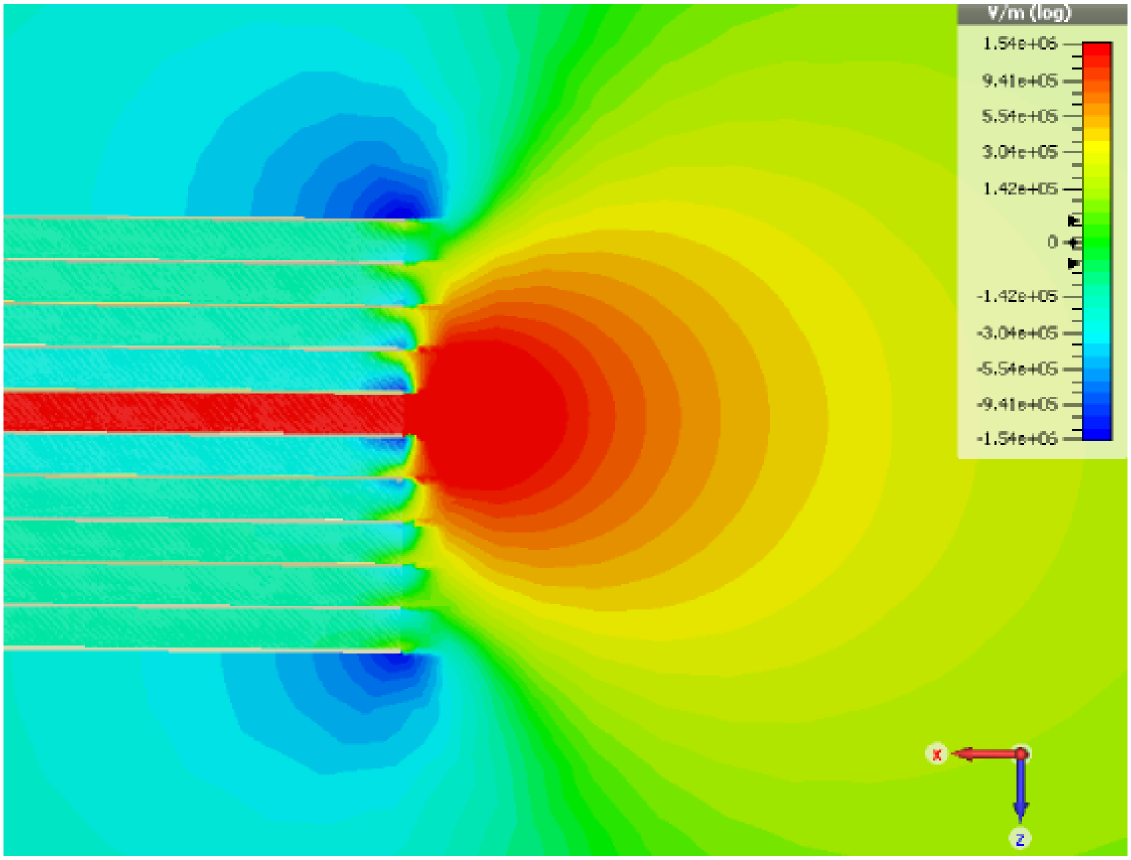

Figure 4.6: Accelerating gradient/Z-component of the electric field produced by firing the central line while the other lines are not connected by ports (Case 3).

negative region of the simultaneously fired stack reaches -150 kV/m.

Looking more closely at the fields produced by each fired line (Figure 4.10), an interesting effect appears. The center line (N = 3), despite being subjected to the largest parasitic voltage drop, also produces the highest gradient of the lines. This appears to be due to the induced voltages in neighboring lines causing the fields to propagate in a direction outward from the line, which can be qualitatively observed in Figure 4.5. Thus, the effect of parasitics on the ultimate accelerating gradient produced is more complex than just the reduced voltage output of the line; the directionality of the field propagation helps offset the parasitic voltages.

Another effect observed in Figure 4.10 is the difference in gradient produced by the top (N = 1) and bottom (N = 5) lines. This asymmetry comes from the location of the voltage injection ports, as the voltage in these simulations is being injected between the top and

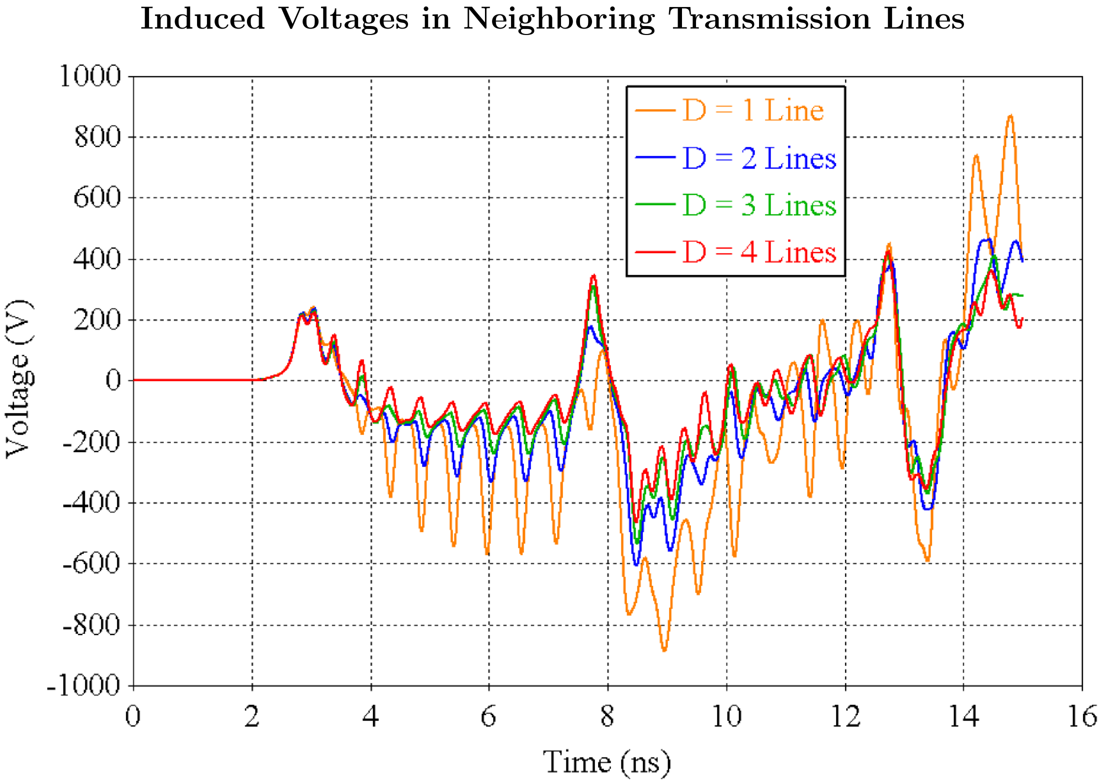

Figure 4.7: Voltages induced at ends of neighboring lines from the firing of a single transmission line while neighboring ports are present (Case 2), with the distance D defined as the number of lines away from the fired line.

central layers of the transmission line. As such, the proximity of the voltage-injection side of the bottom line results in a slightly higher contribution to the gradient.

A comparison of the gradients produced by the center line in the five line stack (with and without ports connected to adjacent lines) and single line surrounded by vacuum is shown in Figure 4.11. Looking at the curves for the center fired line with and without ports, the ultimate difference in gradient produced is small, even with the significant differences in the adjacent induced fields apparent in Figures 4.6 and 4.5. However, when considering the comparison between the center fired line and the single, unstacked line, the center fired line produces a gradient 37% higher than that of the bare line, despite the 5% drop in voltage output of the stacked line.

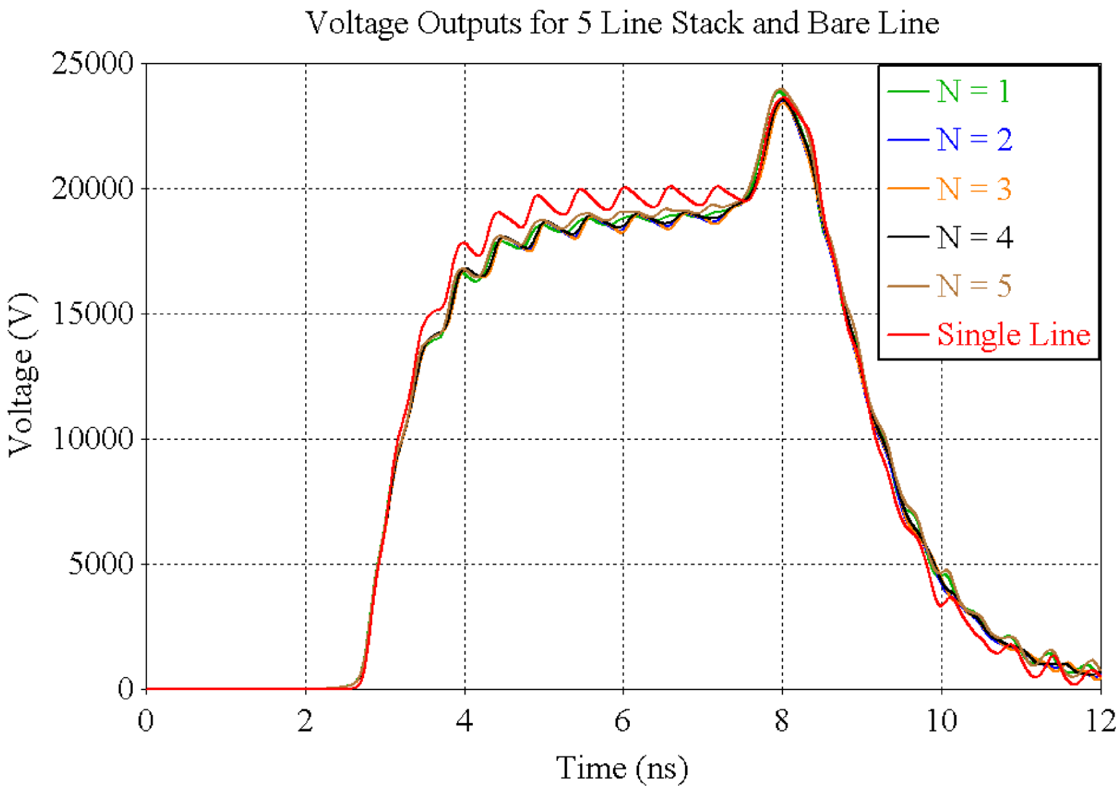

Figure 4.8: Voltage outputs for each of the five stacked transmission lines along with that of a bare line residing in vacuum.

### 4.3.2 50 Line Stack Results

An image of the gradients produced by the matched, 11 cm, 50 line stack is shown in Figure 4.12. A large, relatively flat region of high gradient is found between the lines, with the fields “bowing” in from the top and bottom. Each line was injected with a 0.5 ns rise time smooth step voltage injection, described previously, for a total of 100 ports. The stacks are spaced 5 cm apart, and no beam pipe is used in order to examine their idealized behavior.

#### Parasitics

To analyze the parasitic effects in the larger stack size geometry, a single stack of 50 lines was simulated. Each line contained a smooth step voltage port and a voltage monitor at the terminus of each line. Figure 4.13 shows the output of selected voltage monitors throughout the stack, along with the voltage output of a bare line.

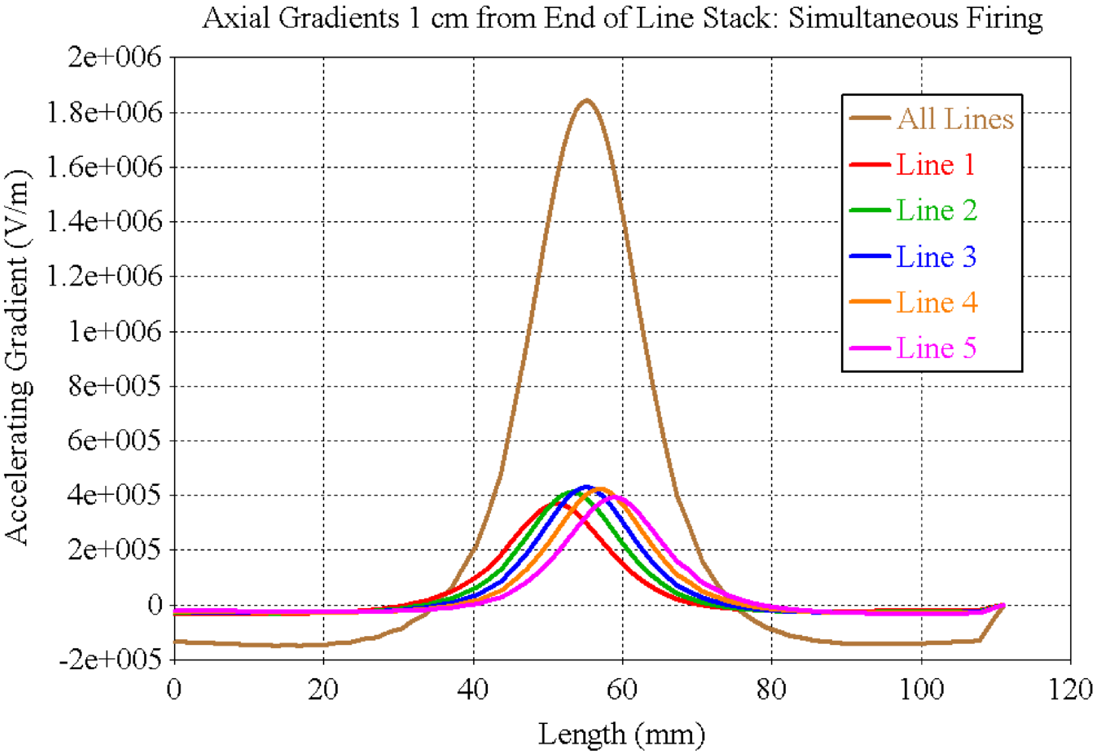

Figure 4.9: Axial gradient produced by the simultaneous firing of stacked transmission lines (Case 1), which equals the sum of the individually fired lines also shown.

The 50 line geometry exhibits a markedly more pronounced parasitic effect than the previously considered five line stack. The reduction in voltage output ranges from 16% for the top line to 30% in the center line, where the parasitic effect is maximized - for comparison, the reduction in the five line case was 5%. For this particular line geometry, the effect plateaus after about 15 lines (or 3 cm), and the voltage reduction stays fairly constant for the center lines. This indicates that beyond a certain stack height, there is no additional parasitic loss, though more lines will be operating at the maximum parasitic loss. These parasitic losses, however, are again offset by the field directionality gain discussed in Section 4.3.1. Finally, the pulse duration of the stacked geometry is about 50 ps shorter than that of the single line, indicating that the parasitic effect has an additional effect of causing the lines to discharge slightly faster.

### Axial Gradients 1 cm from End of Line Stack from Individual Lines

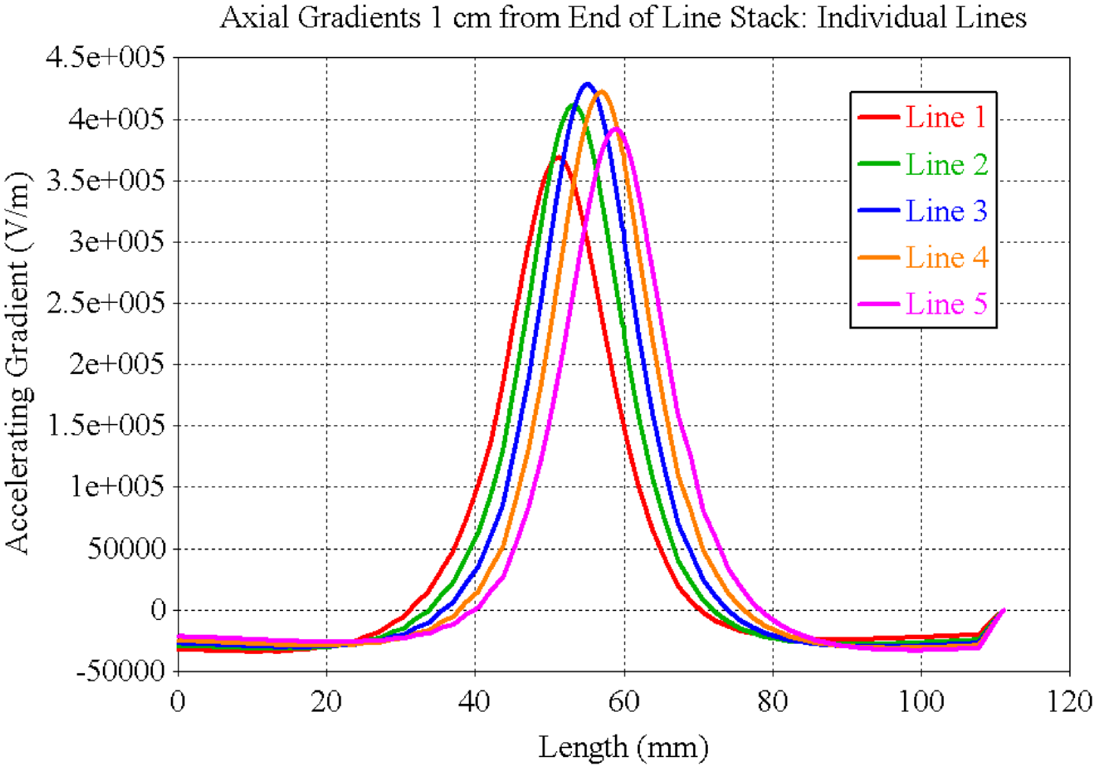

Figure 4.10: Axial gradients produced by each of the individually fired transmission lines (Case 2) 1 cm from the end of the stack of five transmission lines.

### Axial Fields

The following analysis of axial fields utilizes the matched 50 line stack geometry with the stacks separated by 5 cm. Figure 4.14 shows each component of the electric field generated at the central axis of the geometry (2.5 cm from the end of each line stack) at t = 7 ns from the start of the simulation. As expected, the X and Y components are negligible at the central axis. The gradient produced has a much flatter top than that of a single line or small stack, with the gradient reaching 7 MeV/m. The edges of the axial gradient are significantly lower than that of the center, with the gradient corresponding to the top and bottom of the stack reaching only 25% of the peak gradient. This is alleviated somewhat by moving the stacks closer together, which is done for the particle simulations in Chapter 5. Finally, the axial parasitic field gradient becomes negative just 5 mm from the top and bottom of

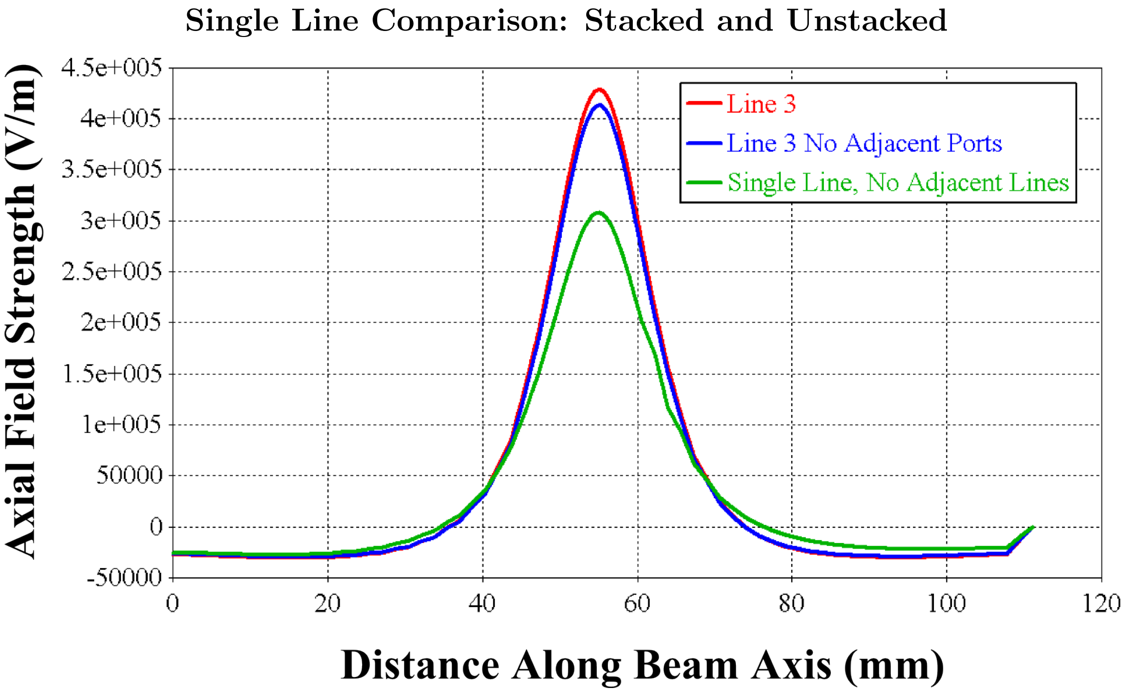

Figure 4.11: Comparison of axial gradients produced by a transmission line fired within a stack of five (Line 3), and surrounded by vacuum with no adjacent lines.

the stack, with fields reaching -2 MeV/m at the nadir, again emphasizing the importance of precise timing of the sequential firing of lines.

The X component of the axial fields offset at various distances from the central axis in the X direction is shown in Figure 4.15, exhibiting a broader, amplified version of the effects first described in Section 3.2.2. Within the extent of the stack, the X components of the field are relatively small, with peaks near the top and bottom of the stack. The direction of the X component of the fields again alternates, centered around the midpoint of the stack. While the fields at the larger offsets are several MV/m, the actual radius of a proton beam for radiotherapy will be approximately 3 mm, as described in Section 2.1.4, and likely only experience X gradients of under 1 MV/m in either direction. The impact of these lateral and transverse fields on a proton bunch will be further detailed in Sections 5.4 and 5.5.

Figure 4.16 shows the Y component of the axial fields offset in the Y direction. There is again a broadening of the axial fields relative to the single line case, with the magnitude of the gradients changing linearly across the height of the stack. The amplitude of these

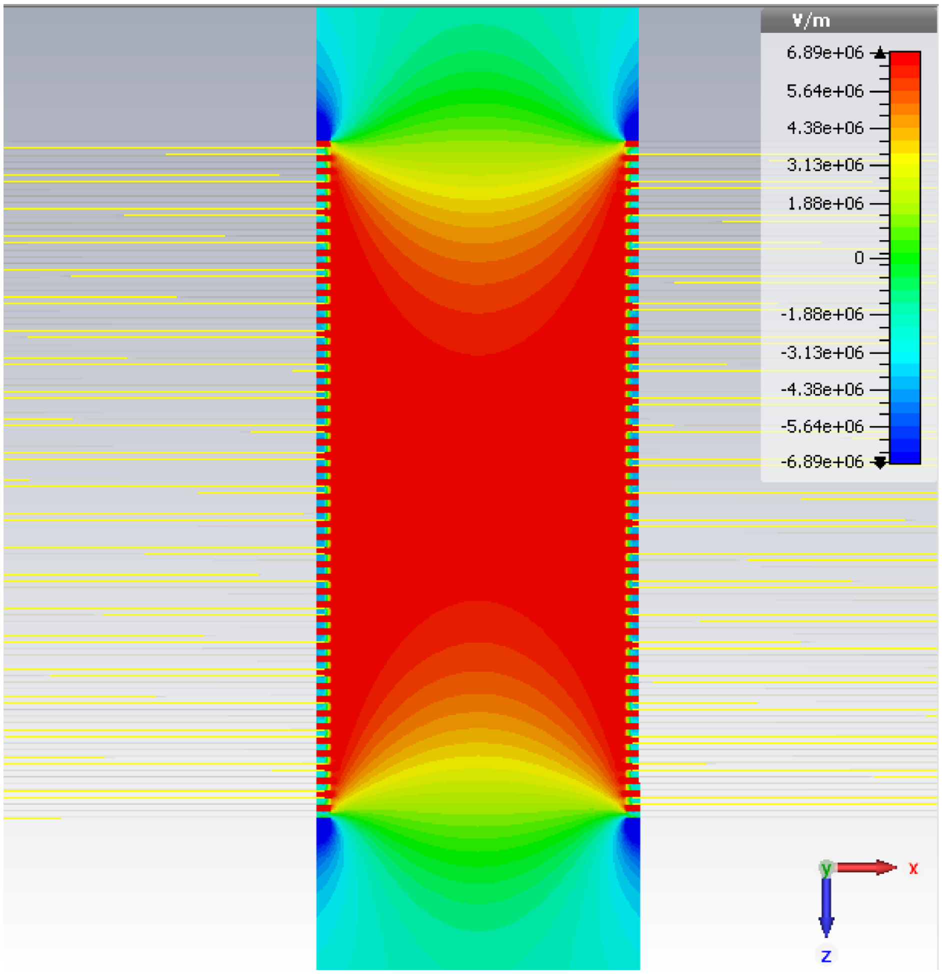

Figure 4.12: Accelerating gradient generated by a stack of 50 matched transmission lines in the XZ-cutplane.

effects is much smaller than the X case, at hundreds of kV/m. As above, the direction of the field alternates about the midpoint of the stack such that a particle would experience both positive and negative acceleration in this direction as it traverses the height of the stack.

Figure 4.17 shows the accelerating gradient at various offsets in the X direction. This behavior is of interest due to the significant variation in field strengths between a single pair of matched lines described in Section 3.2.3. However, in the stacked geometry, the magnitude of the gradient is relatively constant at various points between the lines, with a difference in field strength of only 2% between the center and 1 cm off axis and less than 1% when 0.5 cm off axis. Figure 4.18 shows the magnitude of the accelerating gradient across the region

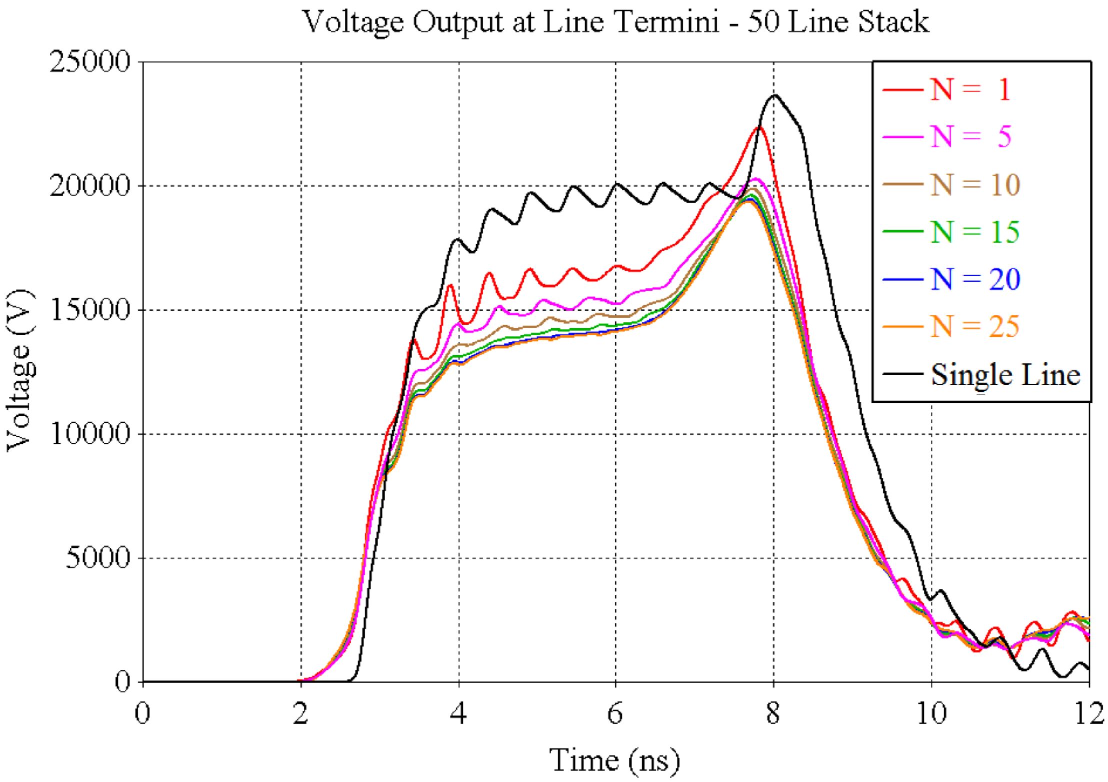

Figure 4.13: Voltage outputs for various lines within a stack of 50 transmission lines, where N is the position of the line within the stack, along with the voltage output of an identical transmission line in vacuum.

between the stacks at various heights within the stack. The field is largest at the center of the stack and, as expected, significantly smaller at the top and bottom of the stack.

## 4.4 Stacked Simulation Conclusions

By simulating stacks of transmission lines, we can better understand the effect stacked lines have on each other. We have described and quantified the parasitic effect of stacking the lines - its effect on line efficiency was found to plateau beyond a certain stack size. The directionality of the field propagation when the lines are stacked was found to partially offset the parasitic voltages by increasing the axial accelerating gradient away from the line stack. The non-accelerating components of the axial fields were investigated and quantified for a particular stacked geometry, and their qualitative behavior may be generalized across

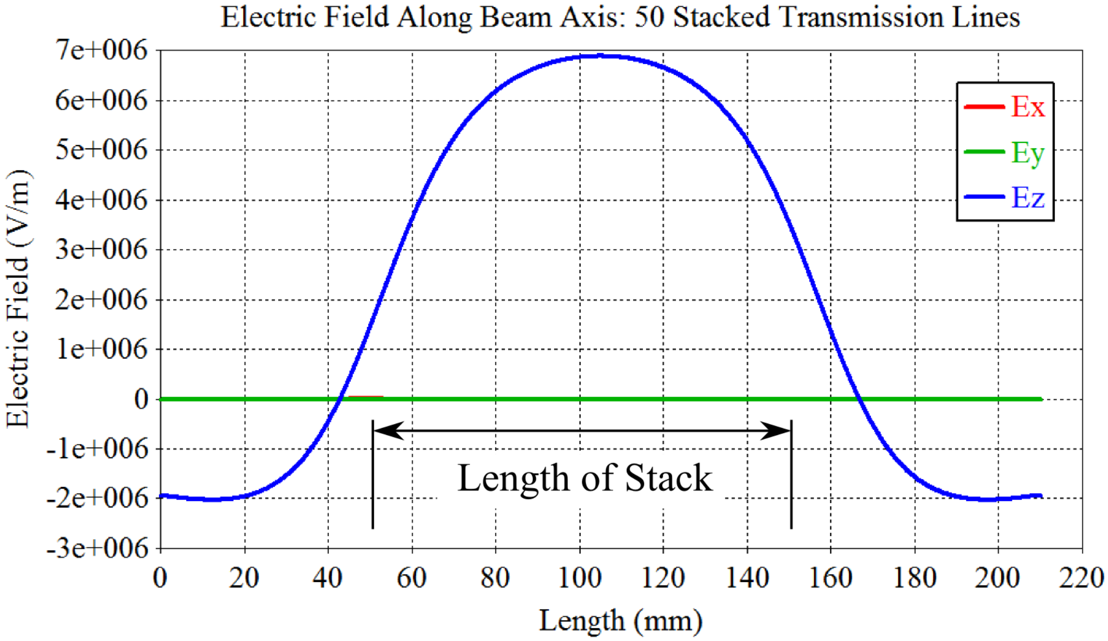

Figure 4.14: X, Y, and Z components of the electric field generated by a stack of 50 transmission lines (11 cm) during a pulse.

other geometries. The variation in accelerating gradient across a pair of matched lines was found to be alleviated by simultaneously firing a sufficiently large stack. This study informs the design of multi-stack systems suitable for particle acceleration, and the ultimate impact of these factors on an ion bunch will be described in Chapter 5.

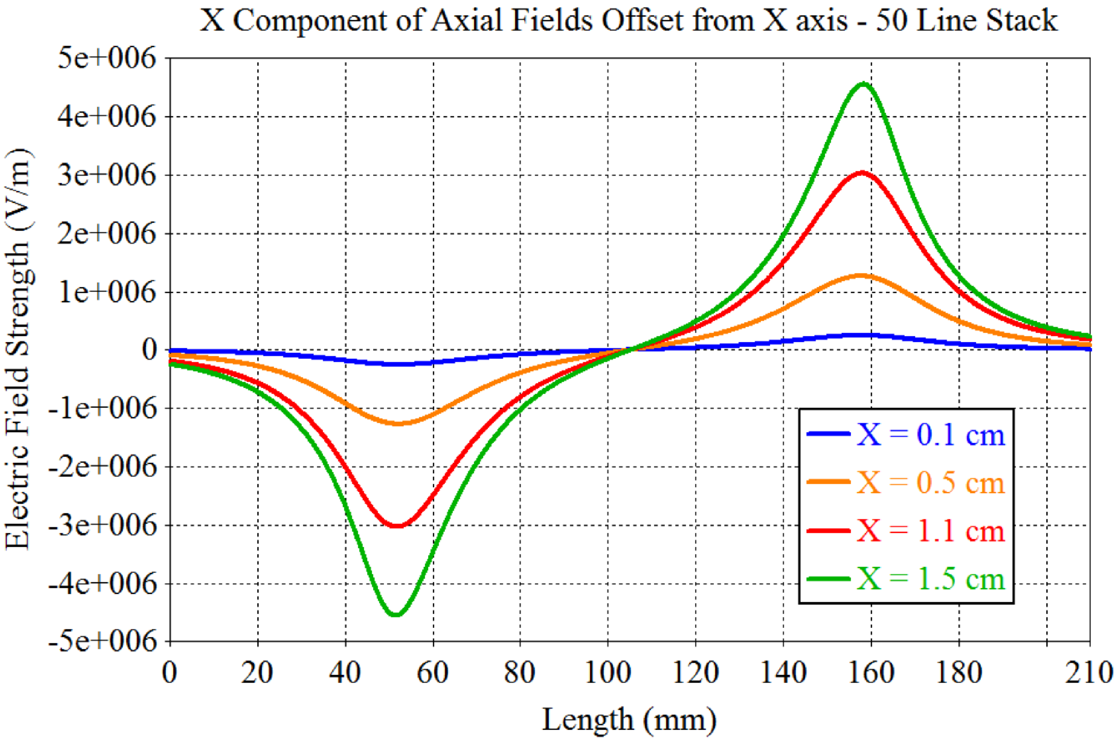

Figure 4.15: X component of the electric field generated by a stack of 50 transmission lines at various offsets in the X direction.

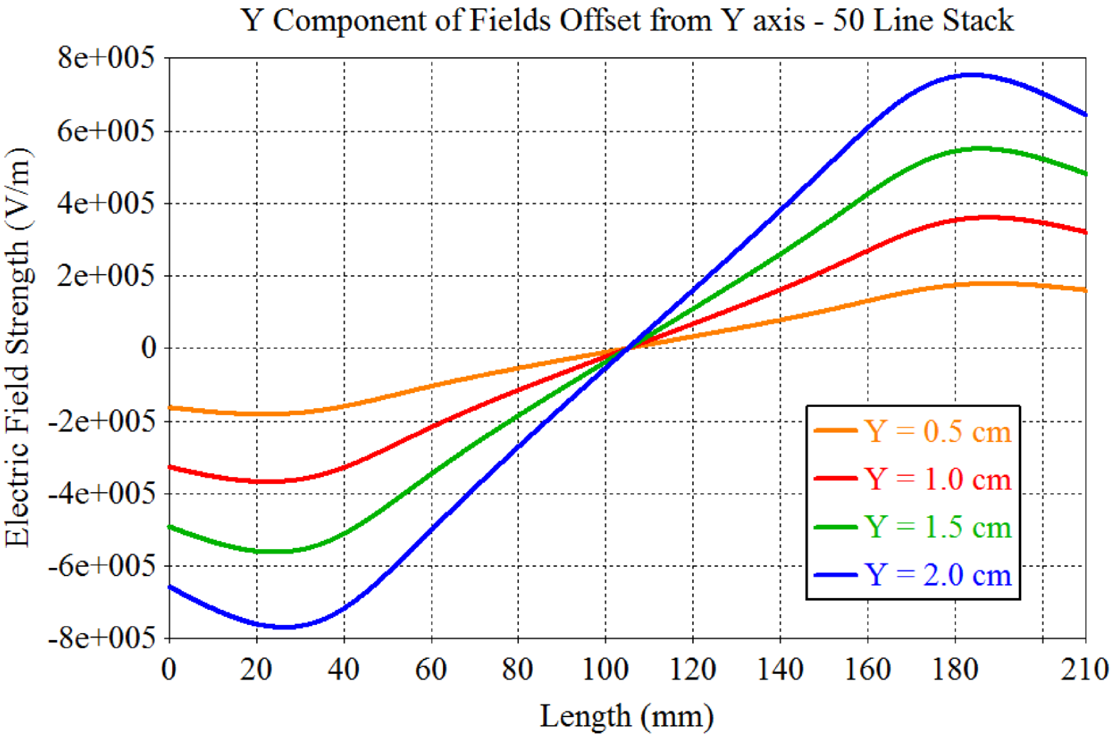

Figure 4.16: Y component of the electric field generated by a stack of 50 transmission lines at various offsets in the Y direction.

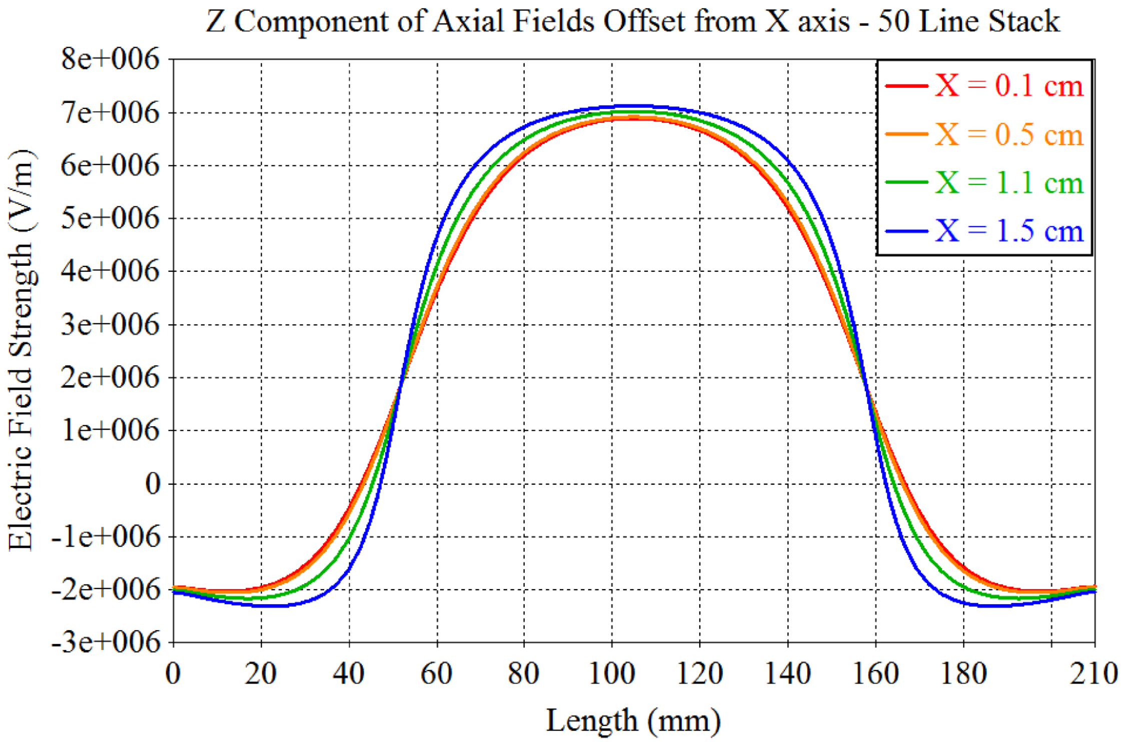

Figure 4.17: Z component of the electric field (accelerating gradient) generated by a stack of 50 transmission lines at various offsets in the X direction.

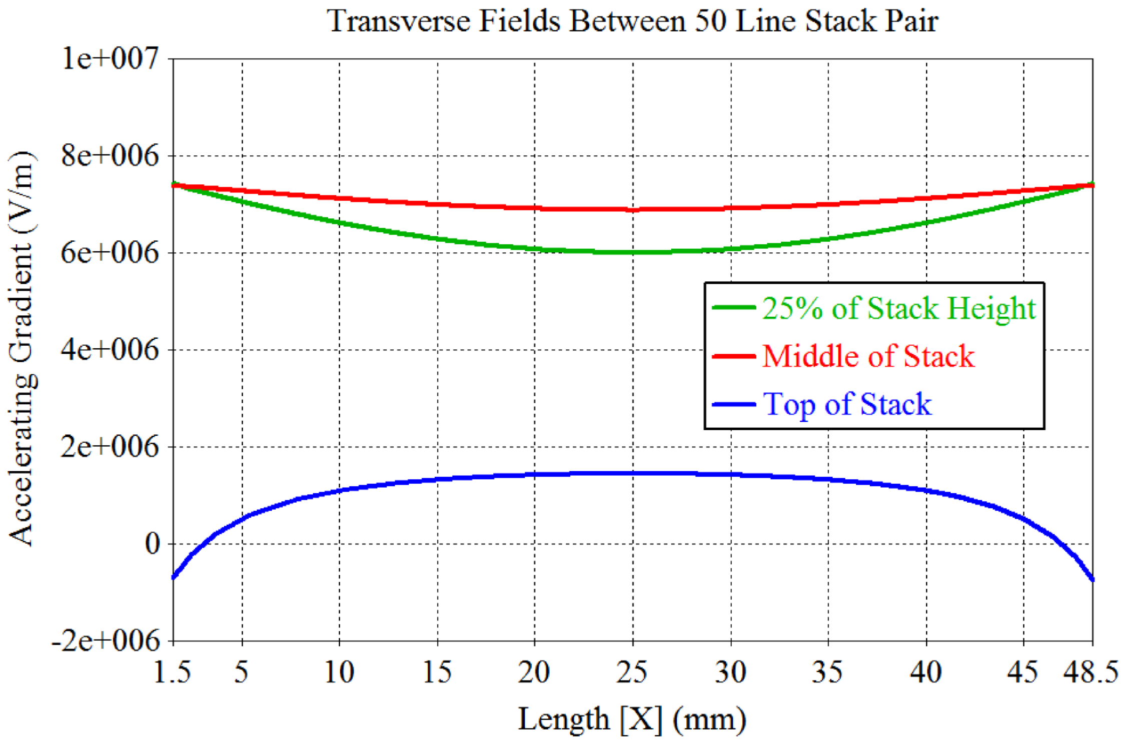

Figure 4.18: Z component of the electric field (accelerating gradient) generated by a stack of 50 transmission lines along curves in the X-direction, between the stacks of lines.

# Chapter 5

# Particle Tracking Simulations

## 5.1 Introduction

Having characterized the behavior of individual transmission lines in Chapter 3, as well as stacks of lines in Chapter 4, we can incorporate that knowledge into the tracking of particles. This can be done by first investigating the acceleration of the particles by a single transmission line stack, followed by acceleration of a series of stacks in a short scale accelerator configuration. Both the closing switch and pulsed voltage excitations will be considered, with the goal of determining the energy gained per unit length for each configuration, as well as the other spatiotemporal properties of the ion bunch. These results will help inform future iterations and improvements of the device, such as the geometry variations described in Chapter 6.

## 5.2 Single Stage Acceleration - Smooth Step

### 5.2.1 Geometry

A single stage accelerator consisting of five stacked, matched transmission lines separated by a distance of 2 cm was modeled and simulated. The insulator and conductor thicknesses of each line were defined to be 1 mm and 0.1 mm, respectively, while the line width was defined to be 10 cm and the line length to be 40 cm. In this particular geometry, the conducting layer between each line was twice as thick (at 0.2 mm) to represent a simple stacking of discrete lines rather than the bottom conductor of each line also acting as the top conductor of the next. The conductor itself was an idealized perfect electrical conductor (PEC), while generic insulating material with a dielectric constant of 10 was used between the conductors. A non-HGI dielectric beam pipe was defined, extending 7 cm above and below the line stack, and possessing a thickness of 2 mm, dielectric constant of 10, and an outer radius of 2 cm (abutted against the end of the lines). A smooth step excitation with a 0.5 ns rise time was used to inject a voltage of 20 kV at the end of each of the 10 total lines.

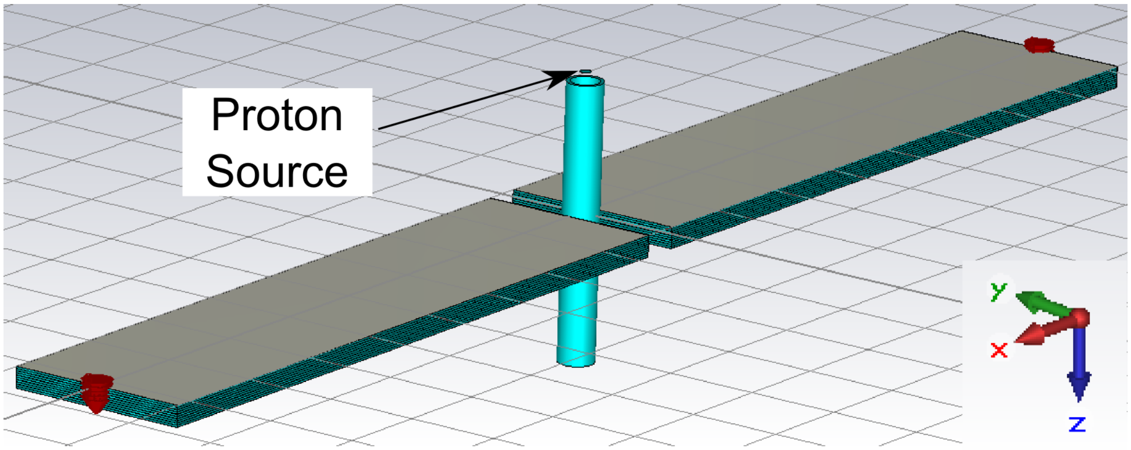

Figure 5.1: Single stage acceleration geometry, using a smooth step excitation and pure dielectric beam pipe.

### 5.2.2 Particle Source Definition

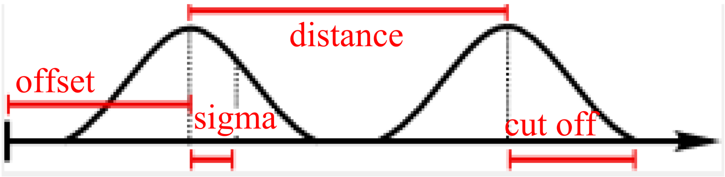

Figure 5.2: Parameters of Gaussian particle source. Image modified from CST, Inc., 2014.

Protons were emitted from a circular area with a 3 mm radius located at one end of the beam pipe. A Gaussian emission model was chosen, with available pulse parameters shown in Figure 5.2. The properties of the pulse used for this simulation are shown in Table 5.1. The kinetic and angular spread were chosen to be zero in order to isolate the effects of the acceleration on the particle bunch. The initial energy was chosen to be 2 MeV to match the output of the proton RFQ described in Section 2.1.4, as well as the charge and temporal properties. The time offset was varied to look at the impact of relative timings of the particle bunch and gradient pulse, further described in Section 5.2.4.

Table 5.1: Particle injection properties for proton acceleration simulations.

| Property | Value | Unit |
|---|---|---|
| Initial energy | 2 | MeV |
| Charge | 30 | pC |
| Cutoff length | 0.15 | ns |
| Time offset | 0.15 + (2.7 to 4.8) | ns |
| FWHM | 75 | ps |
| Kinetic and angular spread | 0 | % |

### 5.2.3 Phase Space Analysis

Figure 5.3 shows a phase space plot of the particle bunch post-acceleration in which the abscissa is position along Z (the beam axis), the ordinate is energy, and each point is a proton; in essence, a snapshot of the particle bunch in time. In this way, the energy and spatial distribution of the particles are intuitively visualized. In this example, 9.5 ns after the start of the simulation, the proton bunch has a spatial extent of 6 mm and an energy spread of 1.5 keV, and the trailing particles have a higher energy than the front of the pulse.

Several of these phase space plots may be combined on one set of axes to give concisely visualize the behavior of the particles as they traverse the accelerator. Figure 5.4 shows such a collected phase space plot for the single stage geometry, with each subsequent colored grouping representing the position-energy phase space at a moment in time, spaced by 0.4

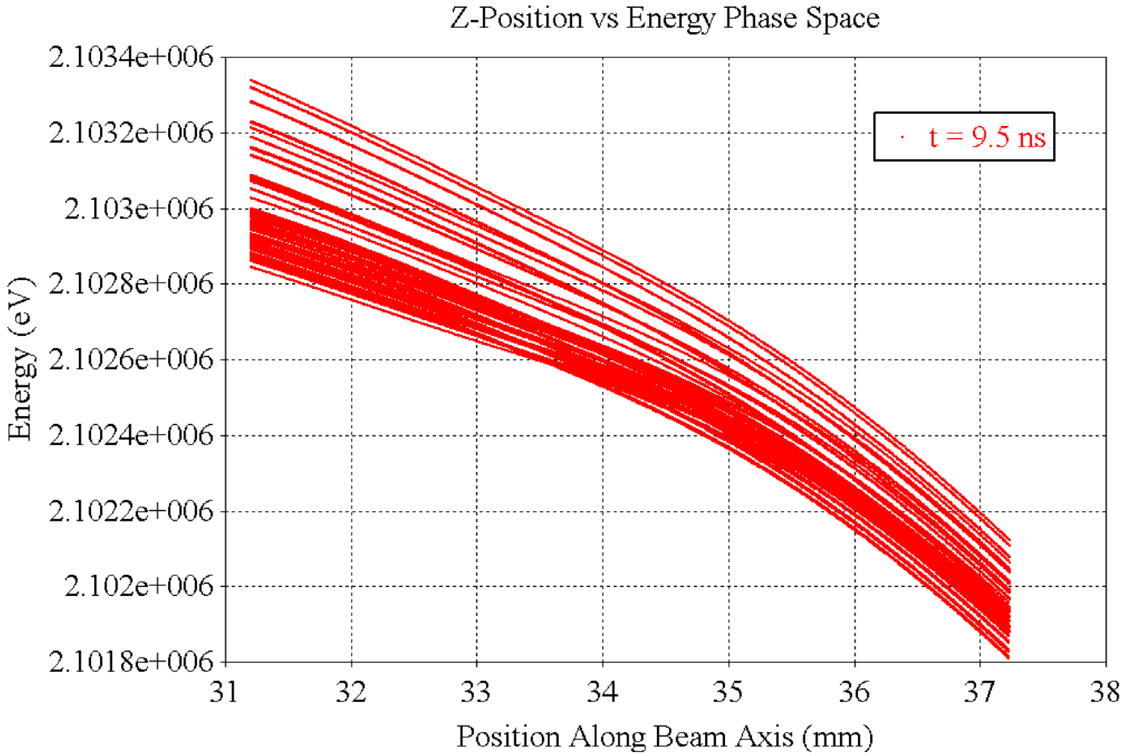

Figure 5.3: Example Z-position vs. energy phase space plot of 88,776 protons. The image represents a snapshot in time of the particle bunch, with each point being a particle; the line-like structure of the particles is due to the finite emission points from the circular source.

ns. The line stack in this geometry extends from 0 to 11.5 mm. Several observations may be made from this plot. The peak energy reached by this stage is 2.103 MeV, an energy gain of 103 keV. By looking at the average energy of temporally adjacent phase space plots, we find that the bunch gains 5.06 MeV/m at peak acceleration in this geometry. When the total average energy gain is compared to the accelerator stack height, an energy gain of 8.96 MeV per meter of transmission line height is found. The output pulse of the transmission line stack begins before the particles arrive (to allow the gradient to reach its maximum value before the bunch arrives), causing the particles to lose energy before passing through the region of stacked lines due to the decelerating parasitic axial fields described in previous chapters. Just prior to the midpoint of the acceleration found temporally at t = 8 ns and spatially at Z = 5.75 mm, the particles at the front of the pulse receive more energy than those that are trailing; after the midpoint of the accelerator, the trailing particles receive more energy relative to those at the front, and after about 30 mm, begin to have higher energies than the particles that are spatially ahead of them.

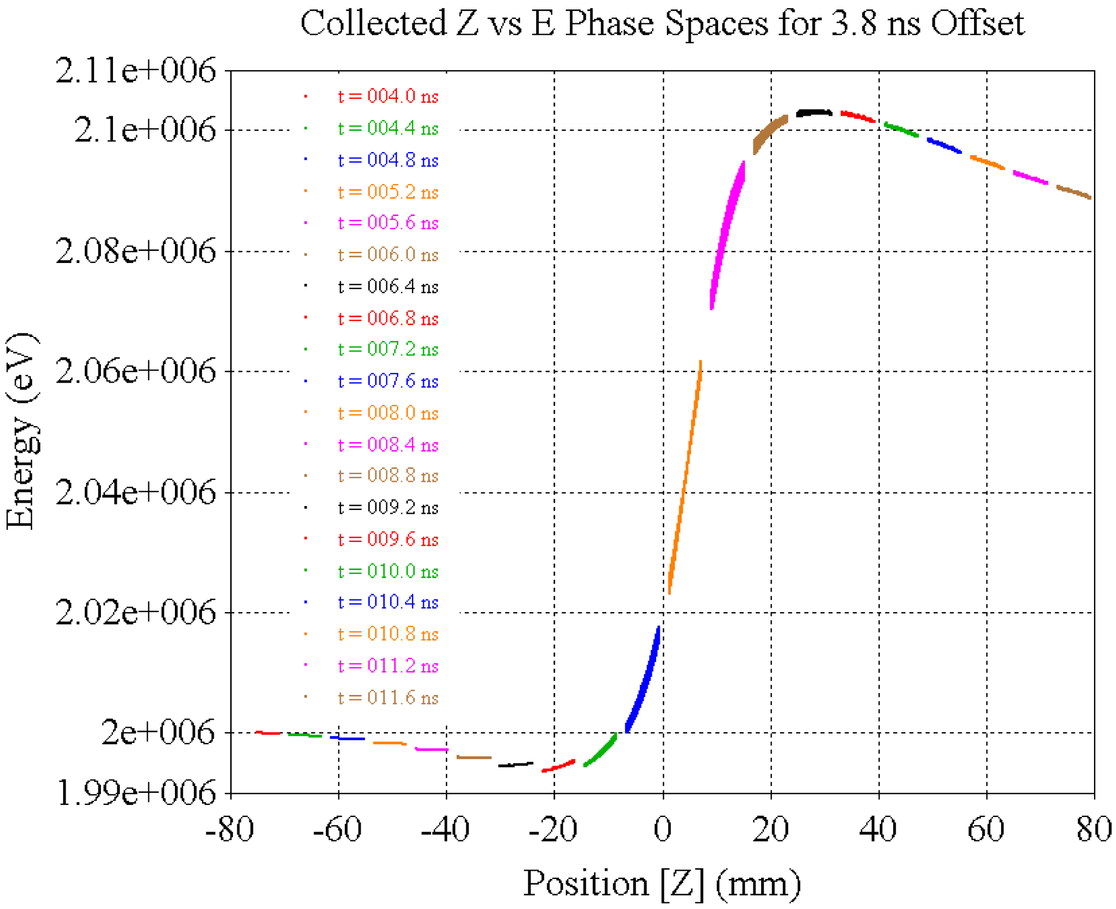

Figure 5.4: Collected Z-position vs. energy phase space of single stage acceleration. Each like-colored grouping represents an individual snapshot in time of the particle bunch, with each succesive step separated by 0.4 ns.

### 5.2.4 Timing Optimization

The arrival time of the particle bunch relative to the rise in accelerating gradient within the beam pipe has a large impact on the post-accelerator phase space of the ions. Determining the optimal arrival time to maximize energy gain is a difficult problem, particularly for more complex pulse shapes. An approach taken here is to parametrically sweep the particle offset time across a range of values in order to maximize the energy gain, in this case from 2.7

ns to 4.8 ns. The collected phase spaces shown in Figure 5.5 show the results of such a timing optimization. A timing offset of 4.3 ns was found to import the most energy to the particles, resulting in a 7.8% energy gain over the initial value of 2.7 ns. Prior to entering the accelerator region, the optimized version is seen to actually decelerate particles due to the axial parasitic fields, indicating that the most efficient acceleration occurs when the pulse starts to rise well before the particle bunch arrives.

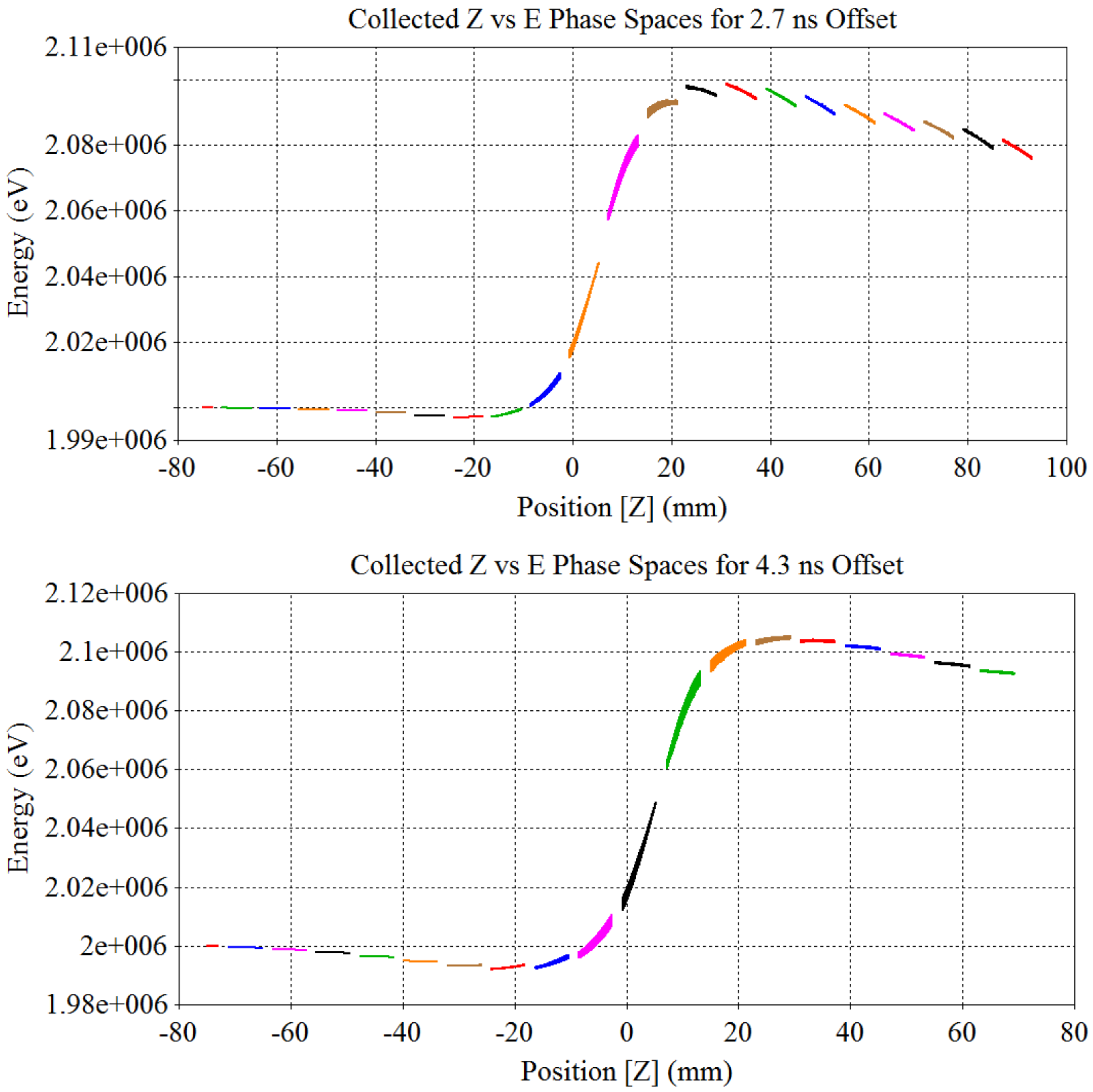
Collected Z vs E Phase Spaces for 2.7 ns Offset

Collected Z vs E Phase Spaces for 4.3 ns Offset

Figure 5.5: Collected phase spaces generated while optimizing arrival time, with each successive color grouping representing the particle bunch at a moment in time, separated by 0.4 ns.

## 5.3 Multiple Stage Acceleration - Smooth Step

### 5.3.1 PIXE Accelerator: Geometry and Excitation

Examining the applications of the DWA to fields other than radiotherapy, we have modeled a compact multi-stage geometry based on the closing switch/smooth step voltage injection. The insulators and beam pipe were defined to have a dielectric constant of 3.4, similar to polyimide, while the conductors were set to PEC. The insulator thicknesses were set to 0.93 mm and the PEC thickness to 0.7 mm. The matched stacks each consisted of 150 lines, for a total DWA height of 30 cm (Figure 5.6). Each line was excited by a 0.5 ns smooth step signal of 20 kV. Rather than use the 2 MeV RFQ injection used in the previous simulation, a compact low-energy injector was designed, which is described in the following section.

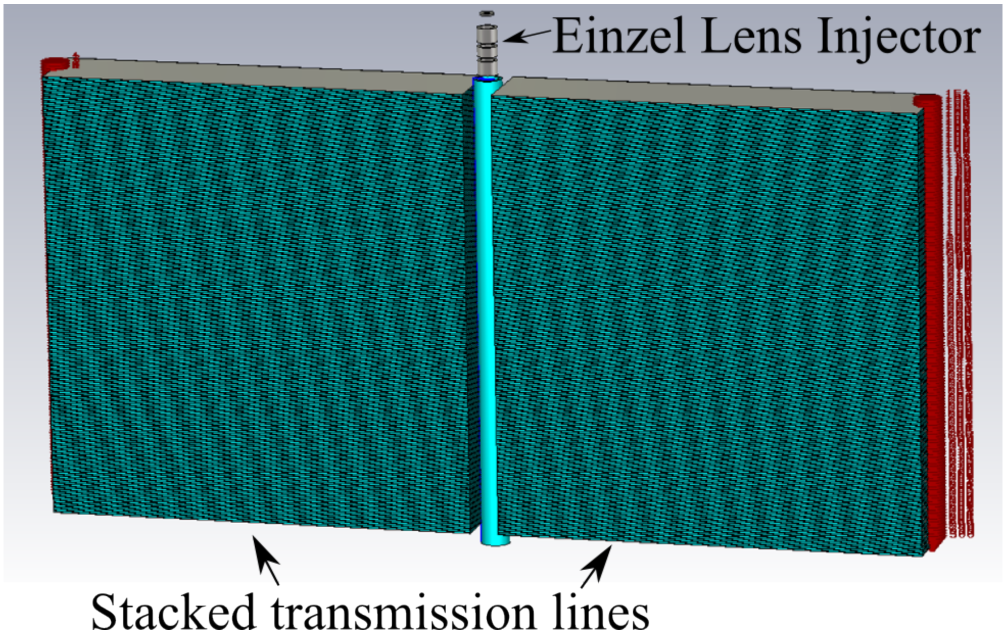

Figure 5.6: Model of a 30 cm accelerator capable of accelerating particles to energies suitable for PIXE.

### 5.3.2 Injector

The output of the proton source was defined to be similar to that of a laser ablated Titanium Hydride (TiH) source, capable of producing 20 to 250 nC of charge depending on laser power and initial accelerating voltage [76]. This output is sufficient to provide the beam currents necessary for PIXE analysis (<5 nA) [68]. Initial acceleration is performed by a -80 kV bias on the source followed by a simple 3 element Einzel lens configuration. The electrostatic potentials of the injector as well as the collected phase spaces of this portion of the model are shown in Figure 5.7.

### 5.3.3 Phase Space Analysis

The collected phase spaces of the accelerator as a whole are shown in Figure 5.8. The average energy of the proton bunch following acceleration is 2.3 MeV, for an effective gradient of 7.6 MeV/m. There is significant spreading in terms of energy (up to 30% in either direction) and distance (up to 3 cm) of the particle bunch throughout the accelerator. Large differences in energy are created when the low energy particles first reach the high gradients of the accelerator. Due to sub-optimal focusing of the injector, 58% of the injected protons collide with the beam pipe (Figure 5.9).

### 5.3.4 Drawbacks and Future Work

A number of drawbacks exist with this system as described. The particle bunch generated by the Einzel lens injector is not well bunched; a more sophisticated model based on existing 80 keV proton injectors could be used to improve the output phase space of the ion source [77]. Due to the sub-optimal particle bunch, switch timing optimization is difficult without losing a significant portion of the pulse, and the system falls short of the goal energy of 3 MeV. The initial design goal was to use off-the-shelf parts; unfortunately, conventional switches cannot operate at the 20 kV, 0.5 ns rise time regime as described. Optical switches of this type are not readily available and, in any case, the laser triggering system is outside the scope of this system in terms of desired size and budget. As such, further design improvements to this structure have not been performed. However, a potentially more viable option for this application is pulser voltage input. Short scale accelerators designed around using a

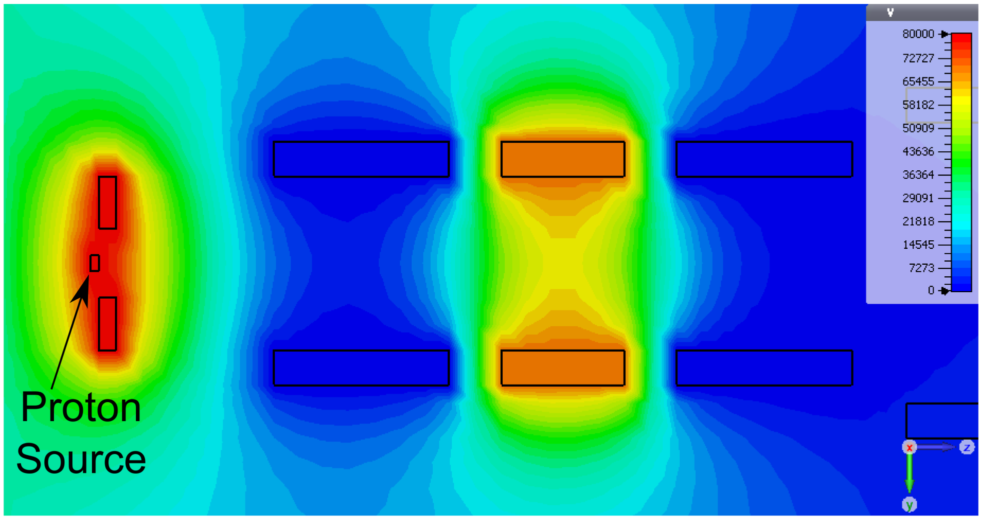

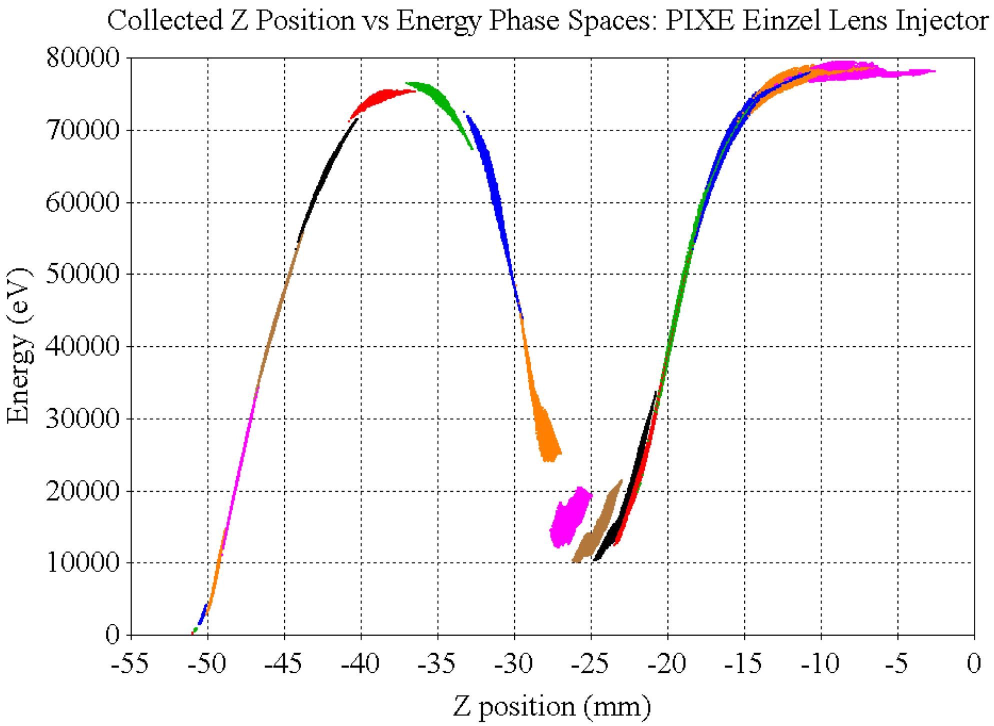

Figure 5.7: (Top) Electrostatic potentials of Einzel lens proton injector. (Bottom) Collected position vs. energy phase spaces of proton injector.

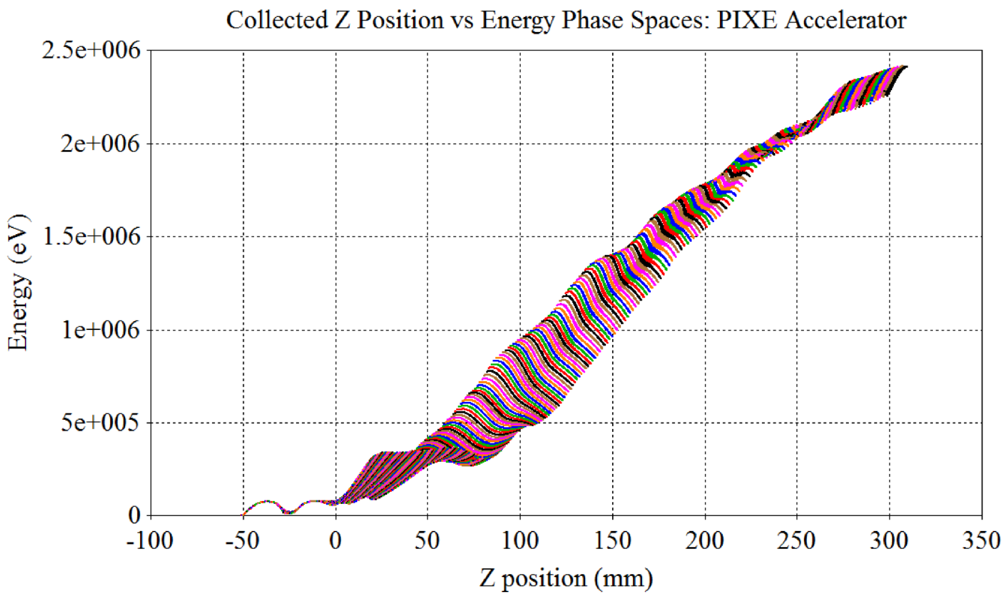

Figure 5.8: Collected position vs. energy phase spaces for the PIXE accelerator.

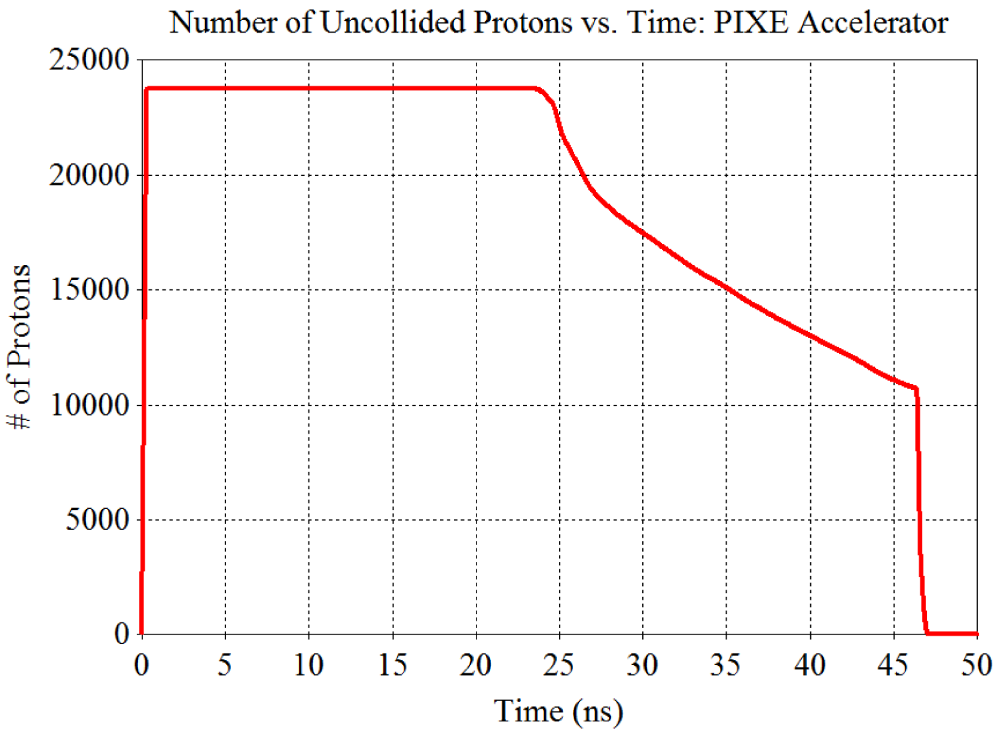

Figure 5.9: Number of protons vs. time for the PIXE acceleration - the loss of protons is due to collisions with the wall, while the sudden drop at the end corresponds to the protons exiting the end of the accelerator.

pulser-based voltage injection are investigated in the following sections.

## 5.4 Single Stage Pulser Acceleration

### 5.4.1 Geometry and Excitation

In order to inspect the feasibility of using a short pulsed voltage excitation, a five line acceleration stage was simulated. The line geometry and materials (copper and lossy polyimide) are the same as the benchmark line described in Chapter 3, giving a stack height of 1.11 cm. The spacing between the lines was 2 cm. The beam pipe consisted of HGI material, as described in Section 3.3.2, and extended 1.2 cm above and below the stack of lines. The outer radius of the beam pipe was 1.8 cm, and the thickness was 2.5 mm. The voltage was injected with a 200 ps rise time, 1 ns hold time, and 1.5 ns fall time at amplitudes of 10 kV and 20 kV. This pulse, while much shorter than the smooth step excitation, is still wide enough to capture the entire 300 ps particle bunch. The excitation signal and voltage output of a line receiving this voltage is shown in Figure 5.10. Due to the limited duration of the pulsed voltage injection, note that the output is not quite double the input.

### 5.4.2 Phase Space Analysis

Figures 5.11 and 5.12 show the collected position vs. energy phase spaces of the 10 kV and 20 kV pulsed voltage injections, respectively. The energy gained in the 10 kV case was 46.3 keV, while that of the 20 kV pulser was 92.5 keV. Dividing these values over the length of the accelerating stack (1.11 cm), the gradients achieved per length of accelerator stack were 4.17 MeV/m and 8.33 MeV/m, respectively. This value is comparable with the gradients achieved in the smooth step case in Section 5.3.3. The total energy spread (including the 2 MeV injection voltage) in both cases remained less than a percent, though the spread in energy gain was 4.8% for the 10 kV case and 4.0% for the 20 kV case.

In order to investigate the radial defocusing of the particle bunch, an additional type

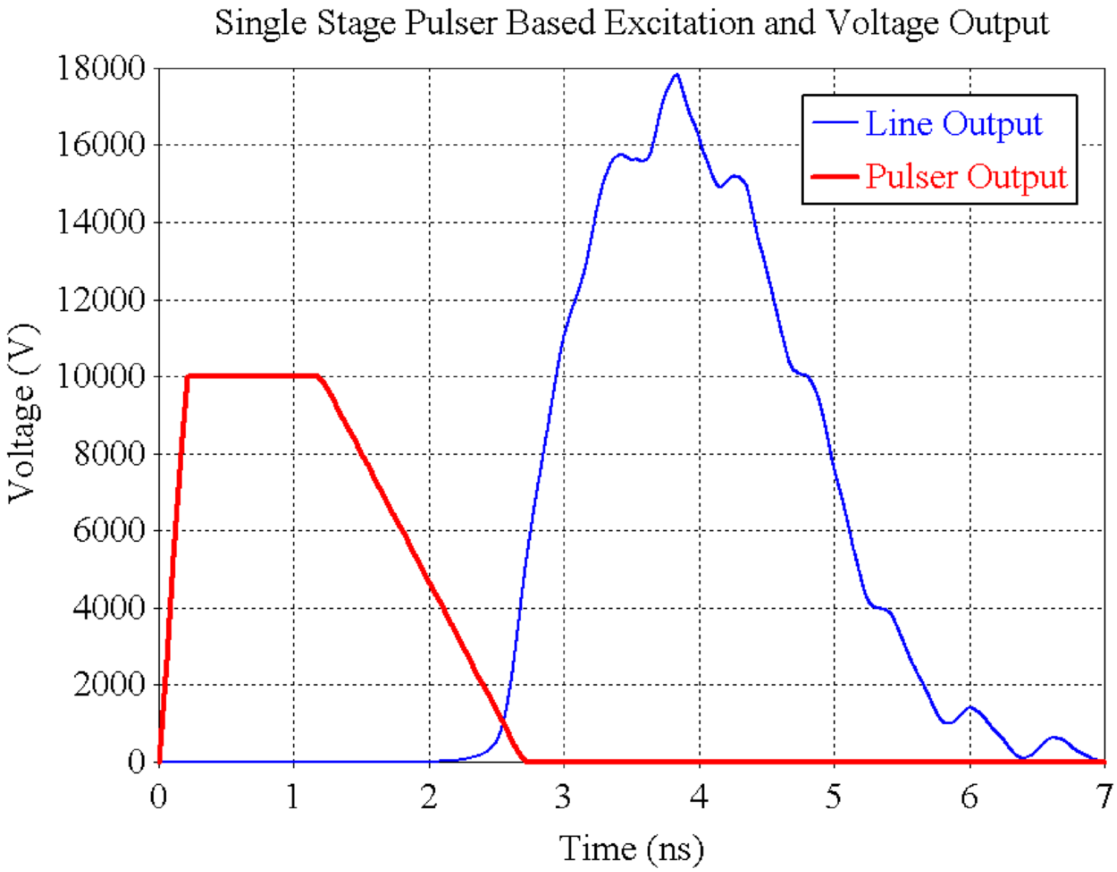

Figure 5.10: Excitation voltage signal used for the pulsed acceleration simulations, along with the voltage output of the line excited by said voltage.

of phase space plot may also be considered. By examining the particle velocities in the transverse (X and Y) directions versus position along the Z axis, we can investigate the impact of the off-axis fields on the spreading of the beam. Figure 5.13 shows the X velocity of the particle bunch with respect to position within the accelerator, and several observations may be made from the plot. The transverse velocities are initially all zero, due to the partially idealized particle source. Prior to the center of the transmission line stack, the particles gain some velocity in the X direction, while after the center of the stack (at Z = 5 mm) each particle gains velocity in the opposite direction. This reversal in velocity is due to the alternating polarity of the axial fields away from the central axis found in Section 4.3.2. The maximum magnitudes of these velocities are relatively small (at roughly 0.02 mm/ns), which would result in a spreading of 1 mm after 50 ns.

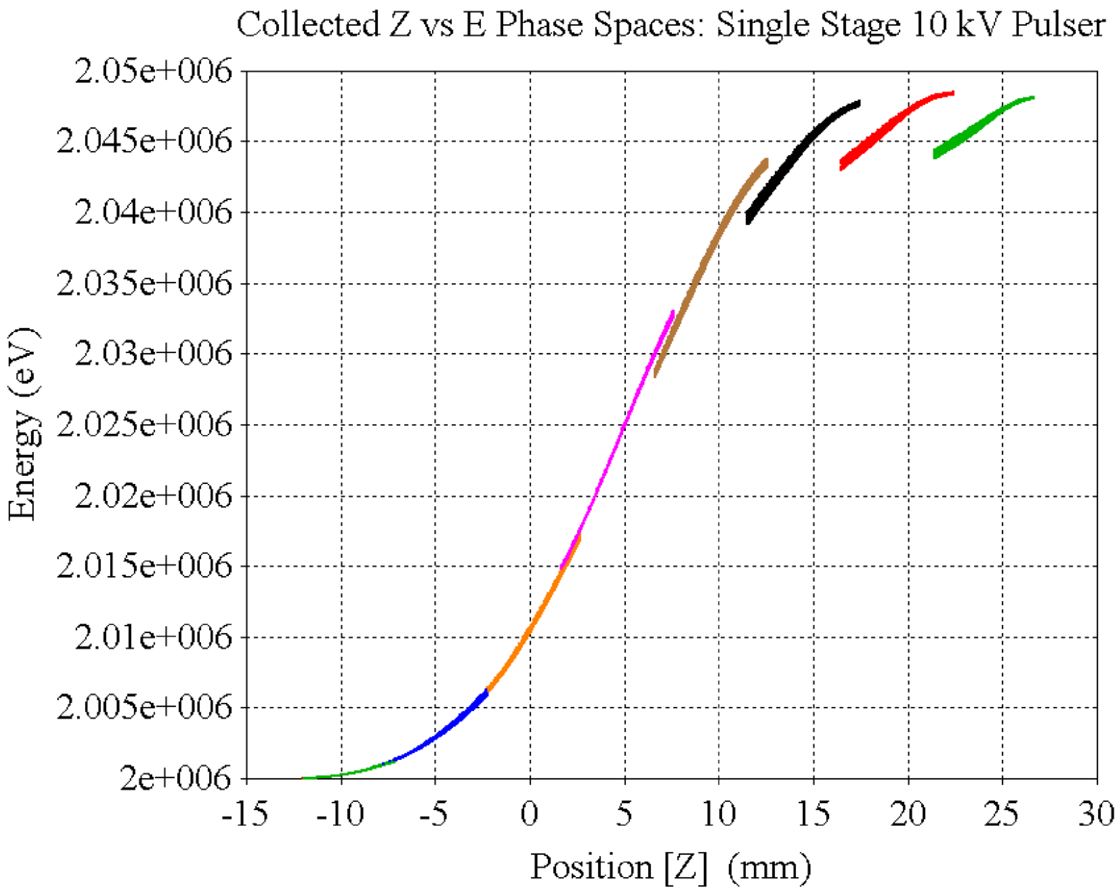

Figure 5.11: Collected Z-position vs. energy phase spaces of a single stage, 10 kV pulser based acceleration. Each like-colored bunch is separated by 0.25 ns.

Figure 5.14 shows a similar velocity versus position phase space plot for the Y component of the particle velocities. Immediately apparent is the similarity to the corresponding plot of the X component of the velocity, indicating a symmetry of the X and Y components of the fields. This symmetry can be observed by looking at the axial fields at distances away from the central axis in both X and Y. Figure 5.15 shows the X and Y components of the fields along a curve offset from the central axis by ± 2.1 cm in both X and Y, for a total distance of 3 cm from the central axis. The fields are seen to be identical, except for the region above and below the beam pipe. Figure 5.16 shows these same fields along axes offset by 2.1 cm in positive X and negative Y as well as negative X and positive Y. The X component of each curve in Figure 5.16 is equal to the Y component of the opposite offset. This indicates

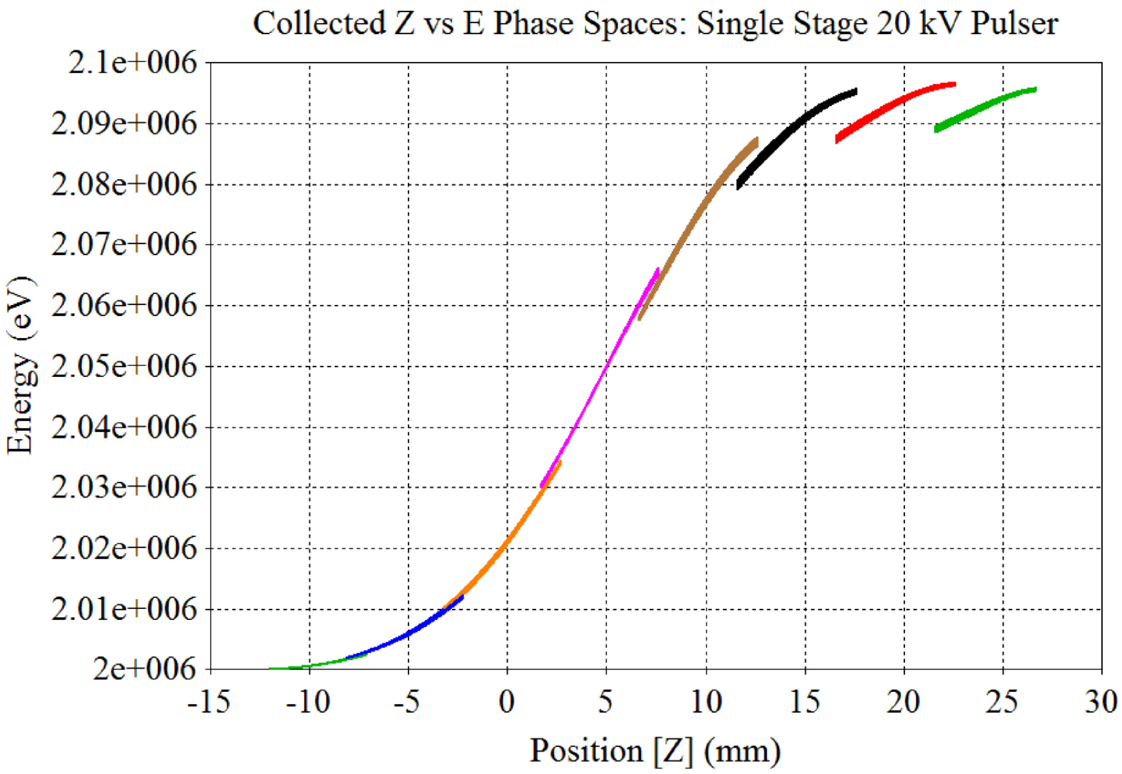

Figure 5.12: Collected Z-position vs. energy phase spaces of a single stage, 20 kV pulser based acceleration. Each like-colored bunch is separated by 0.25 ns.

a cylindrical symmetry of the transverse fields within the accelerator. This symmetry is induced by the propagation of fields around the layered conductors and insulators of the HGI geometry, as first seen in Figure 3.23.

## 5.5 Multiple Stage Pulser Acceleration

### 5.5.1 Geometry and Excitation

Having demonstrated the efficacy of accelerating protons with a pulsed voltage input into a transmission line stack, we can now scale up the geometry to several sequentially fired stacks fired in synchrony with the proton pulse. A set of five stacks of ten transmission lines, each stack separated by 1 mm, thus giving a total height of 11.45 cm, was excited by a 10 kV voltage pulse as defined in Section 5.4.1. The voltage injection of each stack was offset by

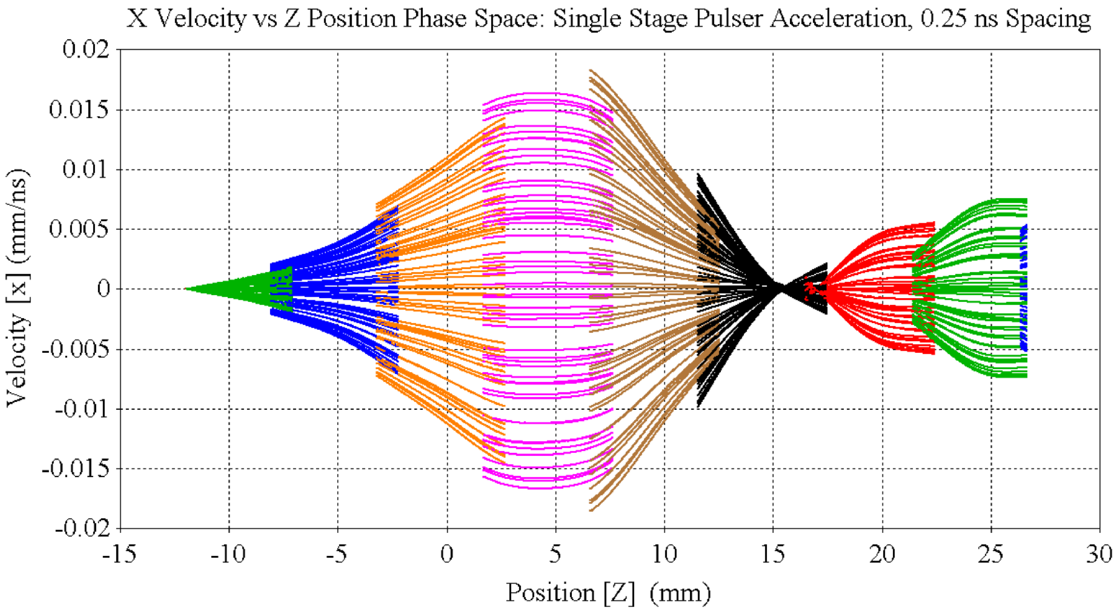

Figure 5.13: Collected Z-position vs X-Velocity phase spaces of a single stage pulser based acceleration. Each like-colored bunch is separated by 0.25 ns.

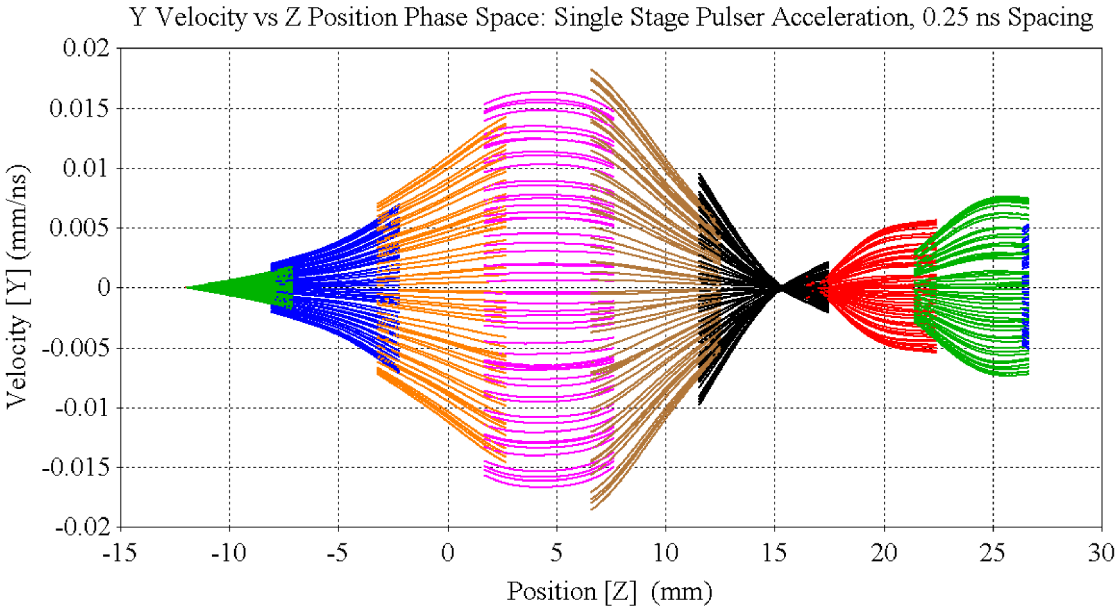

Figure 5.14: Collected Z-position vs Y-Velocity phase spaces of a single stage pulser based acceleration. Each like-colored bunch is separated by 0.25 ns.

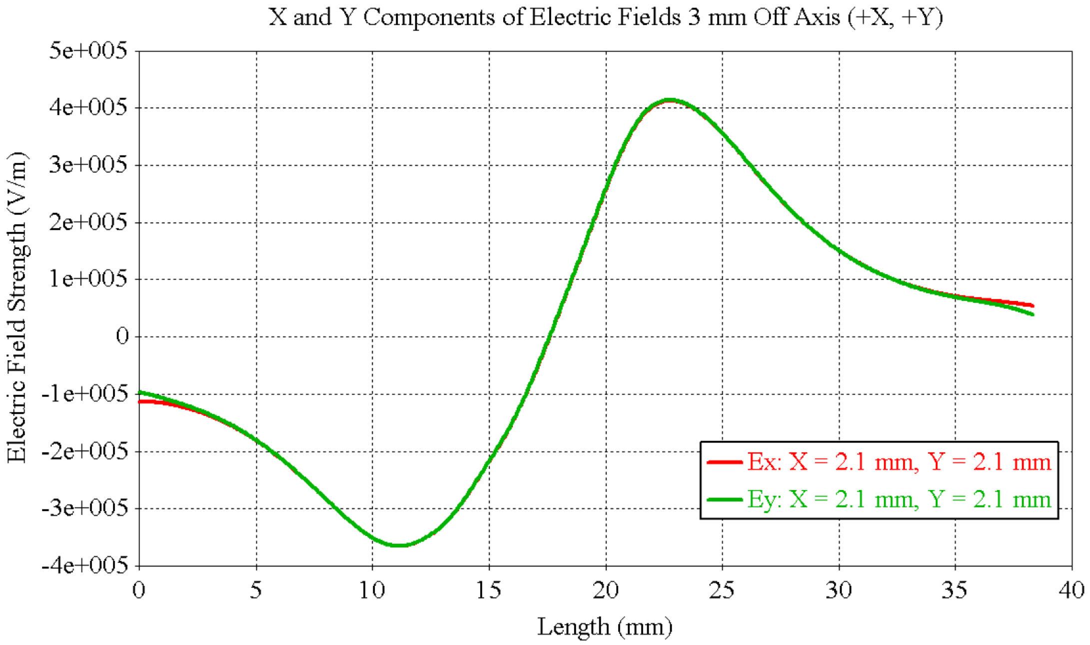

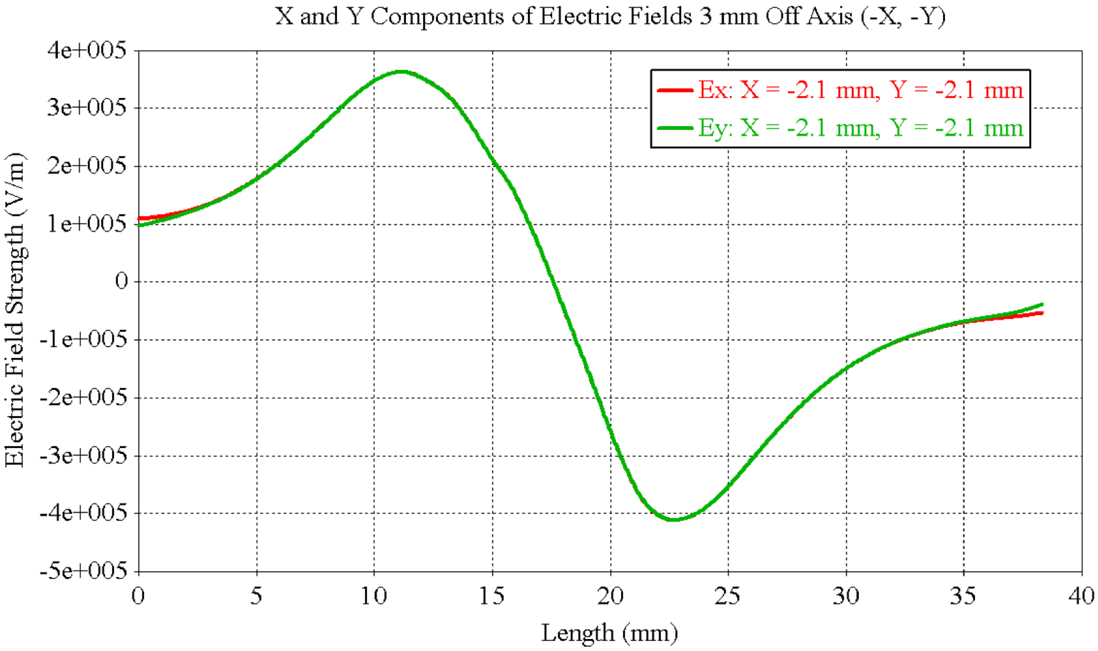

Figure 5.15: (Top) Axial fields along a curve 3 cm from the central axis in the positive X and positive Y directions. (Bottom) Axial fields along a curve 3 cm from the central axis in the negative X and negative Y directions. Note that the X and Y components overlap except for the top and bottom regions of the curve, outside of the beam pipe.

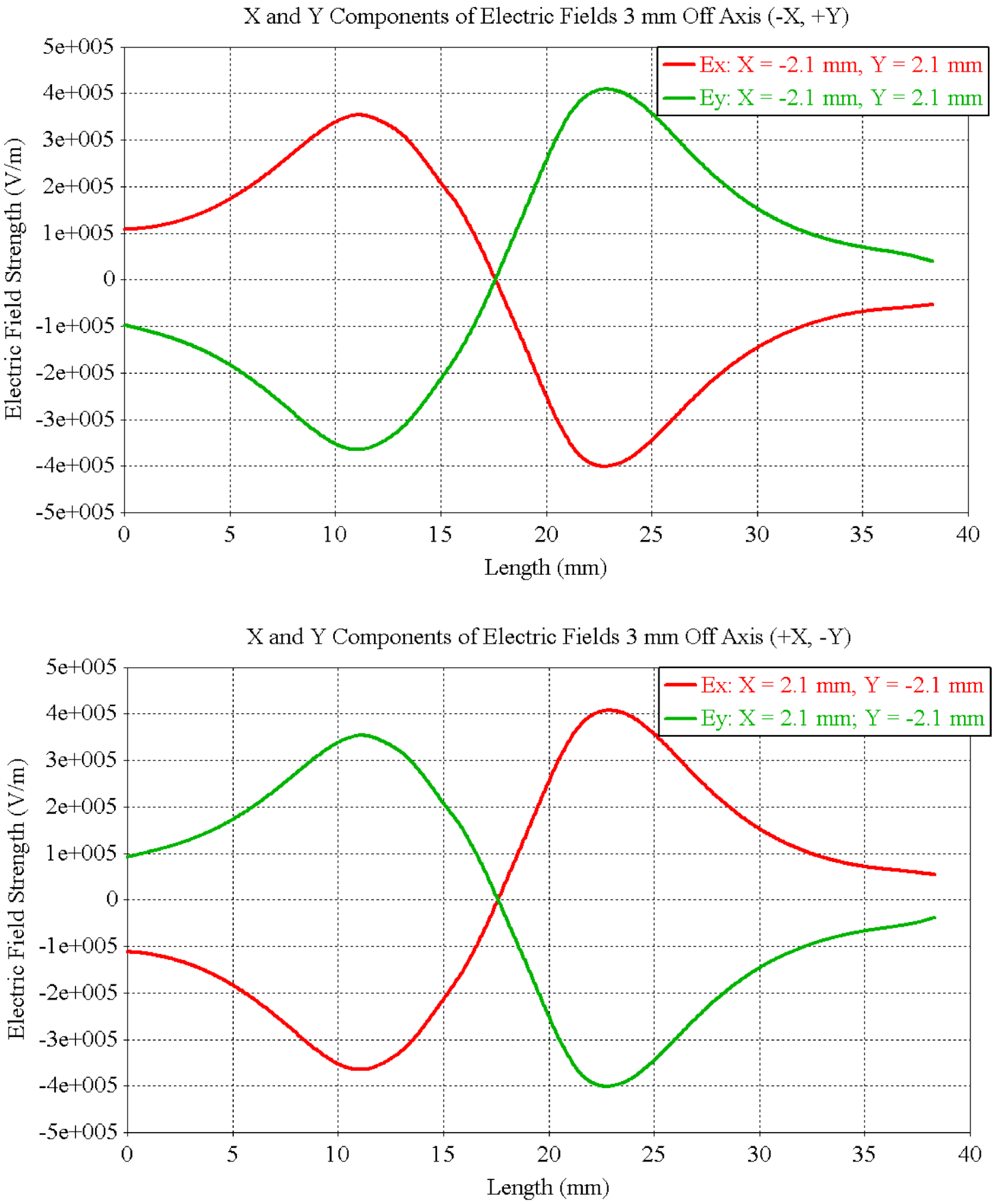

Figure 5.16: (Top) Axial fields along a curve 3 cm from the central axis in the negative X and positive Y directions. (Bottom) Axial fields along a curve 3 cm from the central axis in the positive X and negative Y directions. Note that the X component of one equals the Y component of the other.

1.2 ns per stage to correspond with the velocity of the initial energy of the protons. The proton source was defined with the same parameters as in Section 5.2.2.

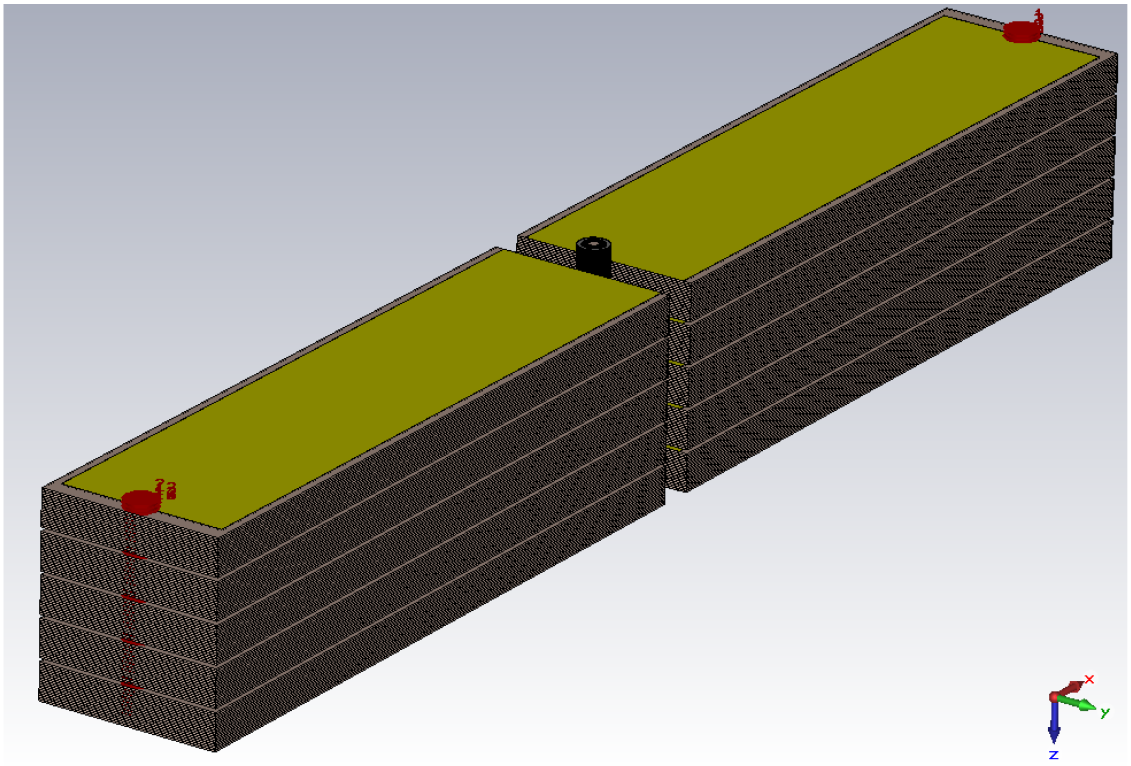

Figure 5.17: Geometry of a five stage accelerator geometry.

### 5.5.2 Electric Field and Phase Space Analysis

Figure 5.19 shows the Z-component of the electric field at successive time points in the simulation. Note that the reflected pulse may be seen in the first line while the final line is firing. The peak field strength in each case is approximately 7 MeV/m. The collected phase spaces of the acceleration may be seen in Figure 5.18. The protons gain 540 keV over the 11.45 cm accelerator length, giving an energy gain of 4.72 MeV/m, comparable to the gains found in the smooth step case. The relatively constant slope of energy over position throughout the length of the accelerator indicates that the particles receive a relatively constant acceleration. Spatially, the particles are compressed from 6 mm to 5 mm, indicating that some degree of bunching is occurring.

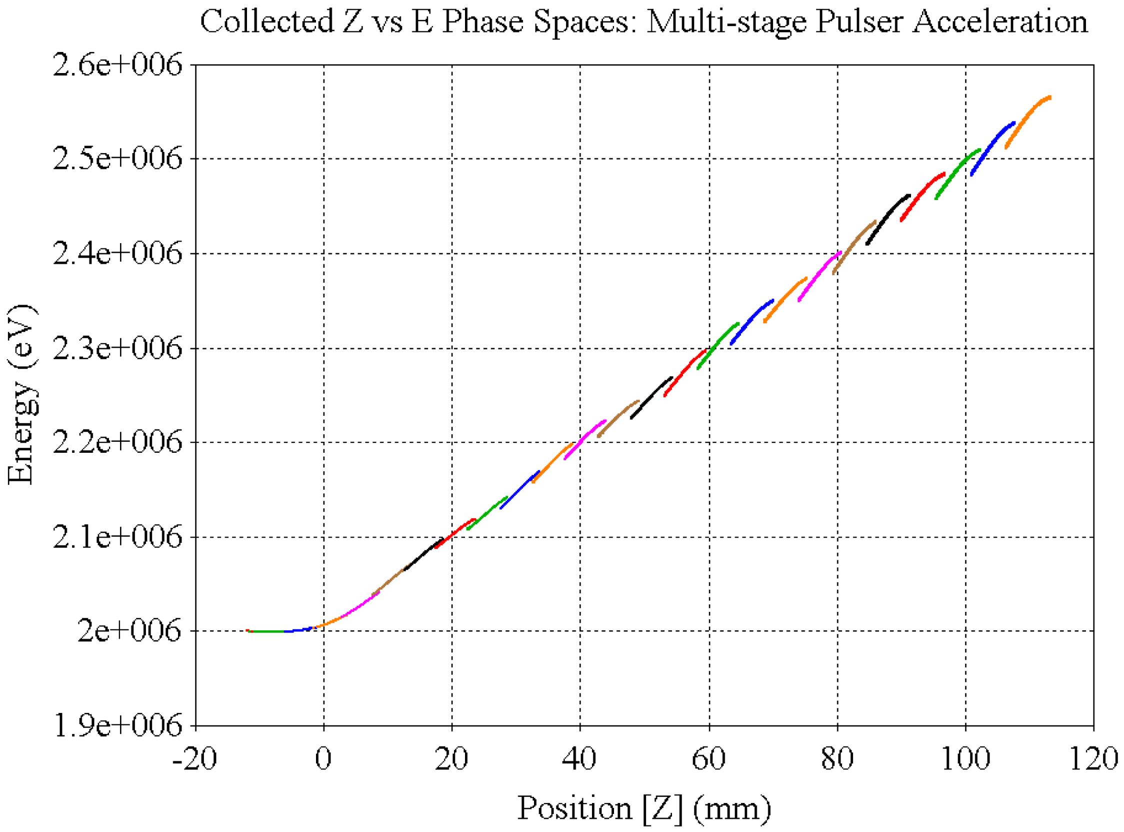

Figure 5.18: Collected Z-position vs. energy phase spaces of a multi-stage, pulser based acceleration. Each like-colored bunch is separated by 0.25 ns.

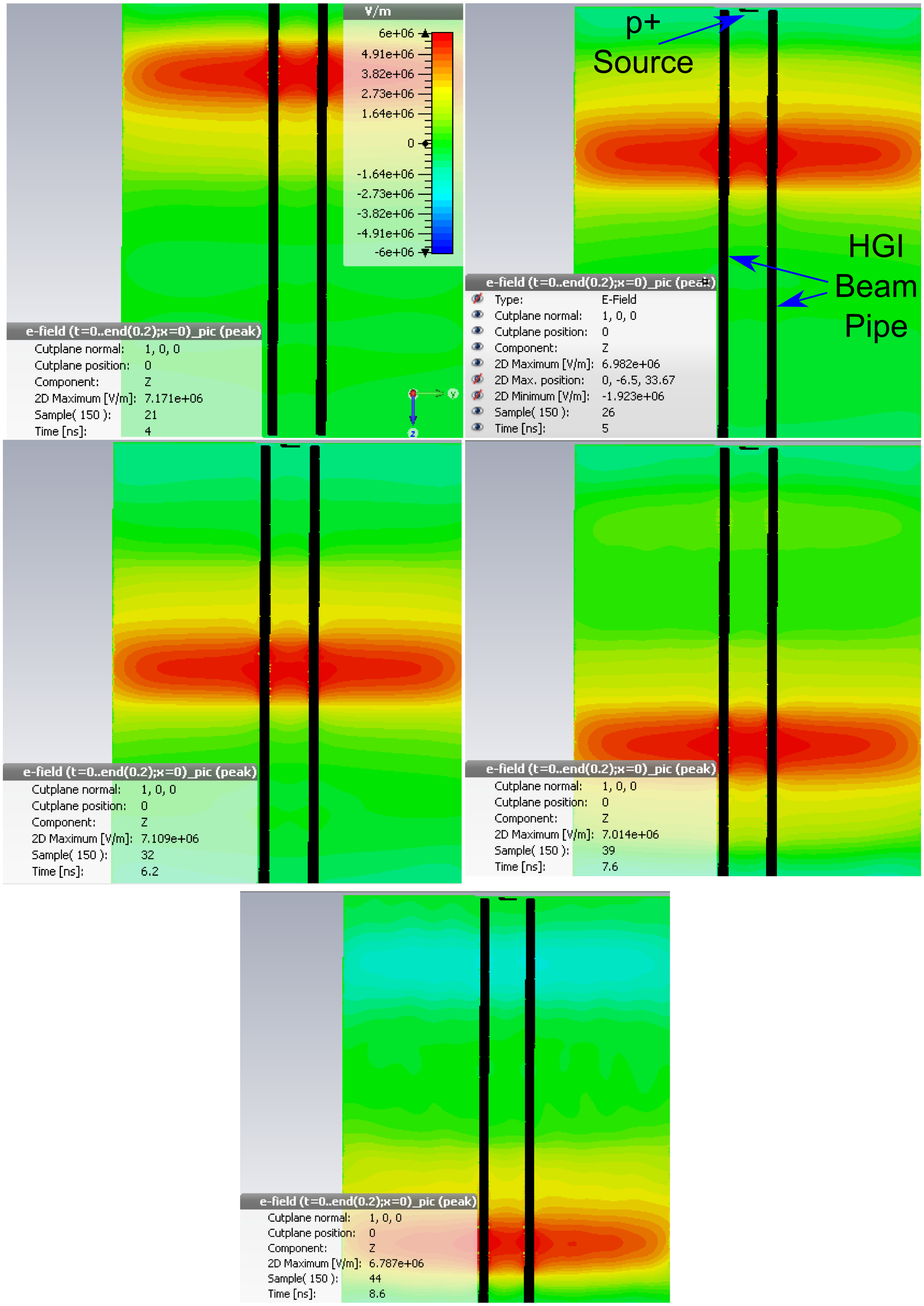

e-field (t=0..end(0.2);x=0)_pic (peak)
Cutplane normal: 1, 0, 0
Cutplane position: 0
Component: Z
2D Maximum [V/m]: 7.171e+06
Sample( 150 ): 21
Time [ns]: 4

e-field (t=0..end(0.2);x=0)_pic (peak)
Type: E-Field
Cutplane normal: 1, 0, 0
Cutplane position: 0
Component: Z
2D Maximum [V/m]: 6.982e+06
2D Max. position: 0, -6.5, 33.67
2D Minimum [V/m]: -1.923e+06
Sample( 150 ): 26
Time [ns]: 5

e-field (t=0..end(0.2);x=0)_pic (peak)
Cutplane normal: 1, 0, 0
Cutplane position: 0
Component: Z
2D Maximum [V/m]: 7.109e+06
Sample( 150 ): 32
Time [ns]: 6.2

e-field (t=0..end(0.2);x=0)_pic (peak)
Cutplane normal: 1, 0, 0
Cutplane position: 0
Component: Z
2D Maximum [V/m]: 7.014e+06
Sample( 150 ): 39
Time [ns]: 7.6

e-field (t=0..end(0.2);x=0)_pic (peak)
Cutplane normal: 1, 0, 0
Cutplane position: 0
Component: Z
2D Maximum [V/m]: 6.787e+06
Sample( 150 ): 44
Time [ns]: 8.6

Figure 5.19: Accelerating gradients generated by each stage of the multi-stage pulsed accelerator.

### 5.5.3 50 kV Excitation with Modified Geometry

While the simulation geometry described in Section 5.5.1 demonstrated successful acceleration of particles, the gradient was rather limited. To increase this gradient, a simulation was performed with a 50 keV injection voltage. In addition to this change, the gap between the lines was reduced to 1.5 cm, and both the inner and outer radius of the beam pipe were reduced to 4.5 mm and 6.5 mm, respectively. The timing schedule remained the same as the previous case; this ultimately proves deleterious to the pulse, as can be seen in the position/energy phase space plot in Figure 5.20. In the later stages of the accelerator (after about 70 mm), it can be seen that the pulse shape becomes distorted, and the energy gain per unit length is reduced. This indicates that the protons have gained enough energy that the EM pulses from the transmission lines are being transmitted to the beam pipe.

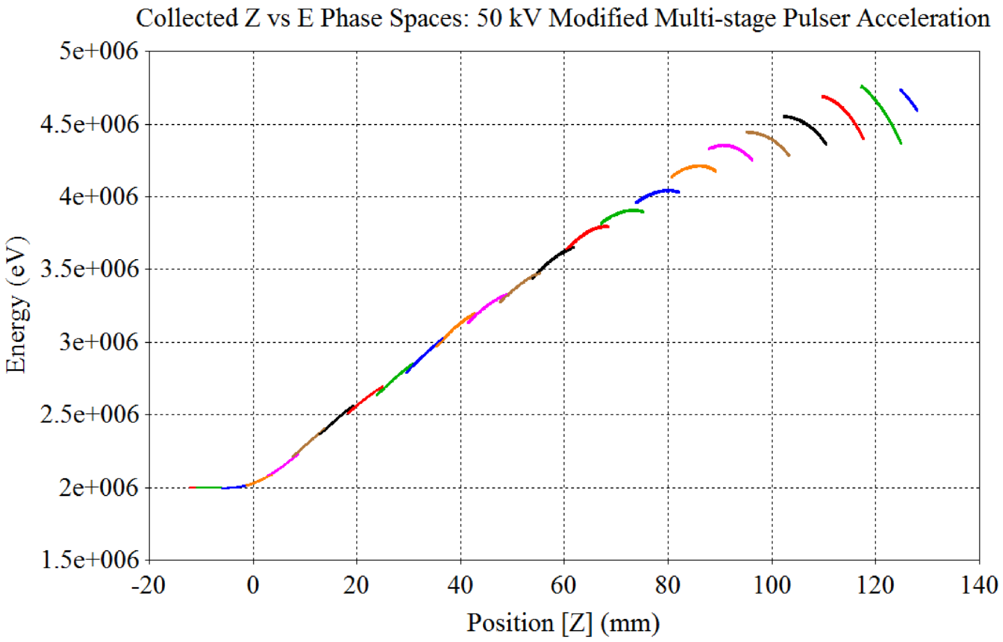

Figure 5.20: Collected Z-position vs. energy phase spaces of a multi-stage, 50 kV pulser based acceleration. Each like-colored bunch is separated by 0.25 ns.

To further investigate this effect, we can look at the power transmitted as a function of time to the entire particle bunch. Figure 5.21 shows this wave-particle power transfer as a function of time for both the 10 kV and modified 50 kV pulser accelerators. Each peak

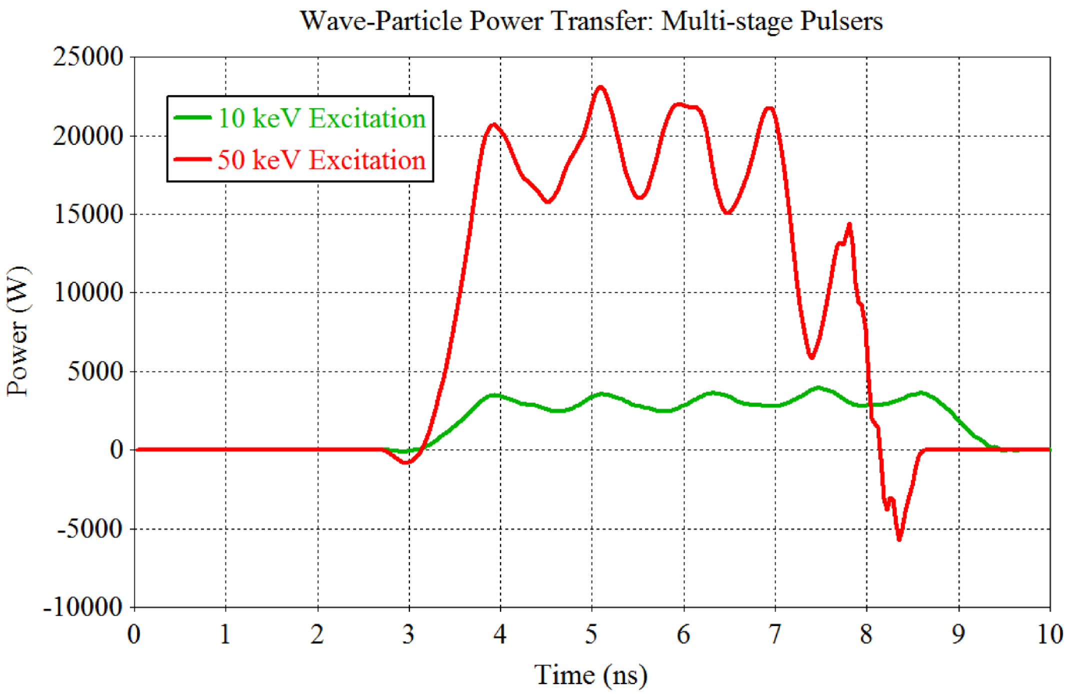

Figure 5.21: The net power transmitted as a function of time to the particle bunch for the 10 kV and modified 50 kV pulser accelerators.

corresponds to the arrival time of the EM pulse to the beam pipe, but due to the long tails of the axial fields produced by each stack, the transmitted power remains within about 25% of the peak value throughout the length of the beam pipe. However, in the 50 kV pulser case, the final stage is fired too late due to the energy gain of the particles, and the axial parasitic fields actually cause a net energy loss in the period from 8.1 to 8.6 ns. As such, the switching schedule of the DWA must be customized to the average gradient of a given geometry and excitation. Despite the late timing of the final stage of the 50 kV accelerator, the energy gained per accelerator length in this configuration was 21.7 MeV/m.

## 5.6 Carbon Ion Acceleration

The DWA architecture may also be used to accelerate ions heavier than protons. The main difference in operation is the timing of the device; heavier ions will travel slower than a lighter one at a given energy for sub-relativistic velocities. Accelerated heavy ions are typically multiply charged, and the total energy imparted to an ion is proportional to this charge. The energy gain of an ion when exposed to an electric field is governed by the mass to charge ratio of that ion. To demonstrate the acceleration of heavier ions, a simulation was performed utilizing the 50 kV pulser geometry and an injection of carbon ions with a charge of +6 (giving a mass/charge ration of 0.5). In this simulation, the carbon ions gained an average of 930 keV in the 1 cm acceleration, resulting in an averaged energy gain of 7.75 $\frac{MeV}{amu \cdot m}$.

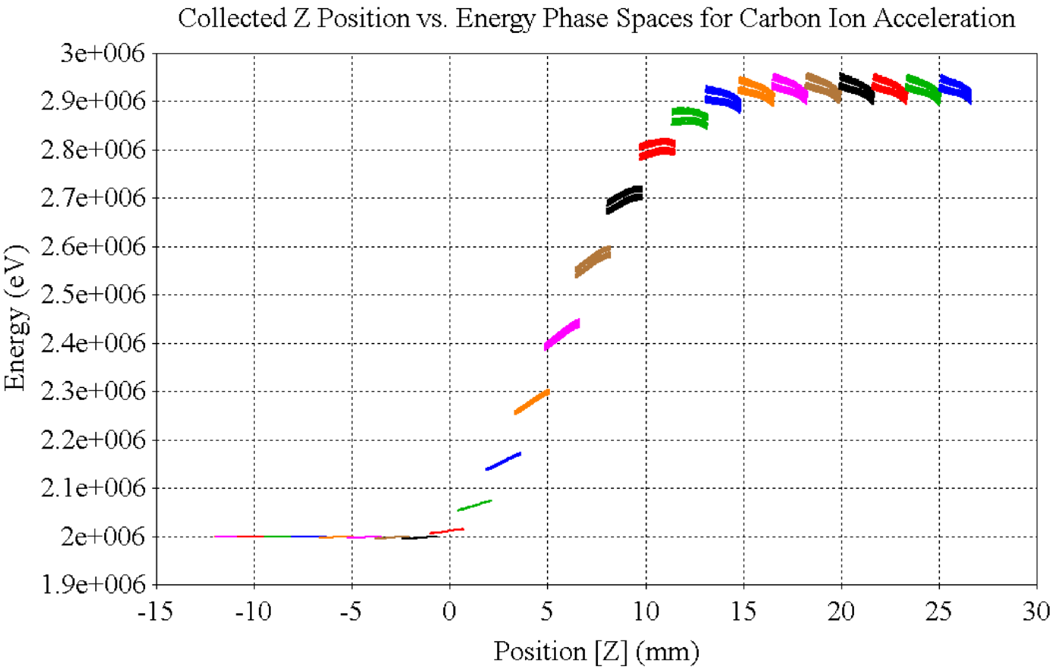

Figure 5.22: Collected phase spaces of carbon ions accelerated with a 50 kV pulser excitation. Each like-colored bunch is separated by 0.25 ns.

## 5.7 Conclusion and Future Work

A variety of short scale accelerator models have been simulated and analyzed. Two triggering modalities - closing switch and pulsed voltage injection - were investigated and utilized in simulation to accelerate particles at gradients up to 21.7 MeV/m. Plots of the collective phase space of a given accelerator geometry were shown to be useful tools for analyzing the performance of an accelerator structure, and when used in conjunction with a parametric study of injection and timing parameters, may be used to quickly optimize the switching schedule of a DWA. Having demonstrated the efficacy of a short voltage pulse excitation for accelerating particles injected at 2 MeV, this method could be coupled to a low energy ion source to reduce the dependence on a bulky RFQ, which would be useful in ultra-compact applications. When utilizing a beam pipe composed of HGI, a cylindrical symmetry in the off-axis transverse fields was found. The feasibility of accelerating heavy ions was demonstrated by simulating a single stage acceleration of carbon ions. As these traditional stacked transmission line geometries fall short of the target gradient of 100 MeV/m for radiotherapy applications, variations of the basic transmission line geometry will be investigated and described in Chapter 6.

# Chapter 6

# Variations of Transmission Line Geometry

## 6.1 Transmission Line Variants

### 6.1.1 Blumlein

A typical Blumlein is very similar to a standard transmission line, with the addition of an electrical connection at the end of the line away from the beam pipe between the top and bottom conductive plates (Figure 6.1). The center conductor is initially charged relative to the connected top and bottom switches, and a closing switch between the central and outer conductors generates a traveling electromagnetic wave which creates the accelerating gradient when it reaches the open end of the line. The connection between the upper and lower lines generates a reflection within the line which theoretically causes a doubling of the gradient at the end of the line [78]. Additionally, this configuration eliminates the high electric fields on the non-accelerating side of the line, though the lateral edges of the line still experience the high fields and generate a parasitic coupling between the lines.

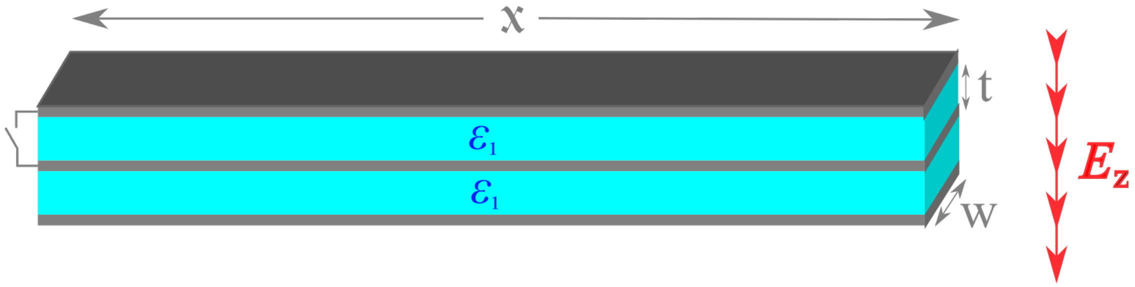

Figure 6.1: A schematic representation of a Blumlein transmission line utilizing a closing switch in the middle of the line.

### Mid-fired Blumlein

A Blumlein transmission line utilizing analogous geometry to the benchmark transmission line described in Section 3.1.1 was modeled to investigate the differences in the voltages generated in the lines. The length of the extra region around the shorted end of the line was 5 mm (Figure 6.2). Voltage and electric field monitors were defined to compare with those of a standard transmission line. A 0.5 ns smooth step/closing switch type signal of 10 kV was used to excite the line at the midpoint of its 40 cm length.

The voltages generated by the mid-fired Blumlein configuration in comparison to the benchmark transmission line are shown in Figure 6.3. The rising edge of the Blumlein pulse occurs earlier than that of the transmission line due to the voltage input being physically closer to the line terminus. The magnitude of the voltage as compared to the charging voltage is nearly doubled, reaching a 18.3 kV peak height. As the fields are reflected within the line, a negative pulse is generated after the transit time of the line. The peak height of this reflected pulse is slightly higher, at 22.8 kV, though this voltage is only reached for a short duration. By changing the polarity of the input voltage, this second peak could be used to accelerate positively charged particles. In comparison, the average voltage output of the transmission line is about 19.5 kV, with a peak height of 23.6 kV. The fields from the open end of the line propagate towards the beam axis in a very similar manner as those in the transmission line geometry. Thus, as expected, the accelerating gradient generated by the Blumlein has a very similar shape to its voltage output, seen in Figure 6.4. The rapid

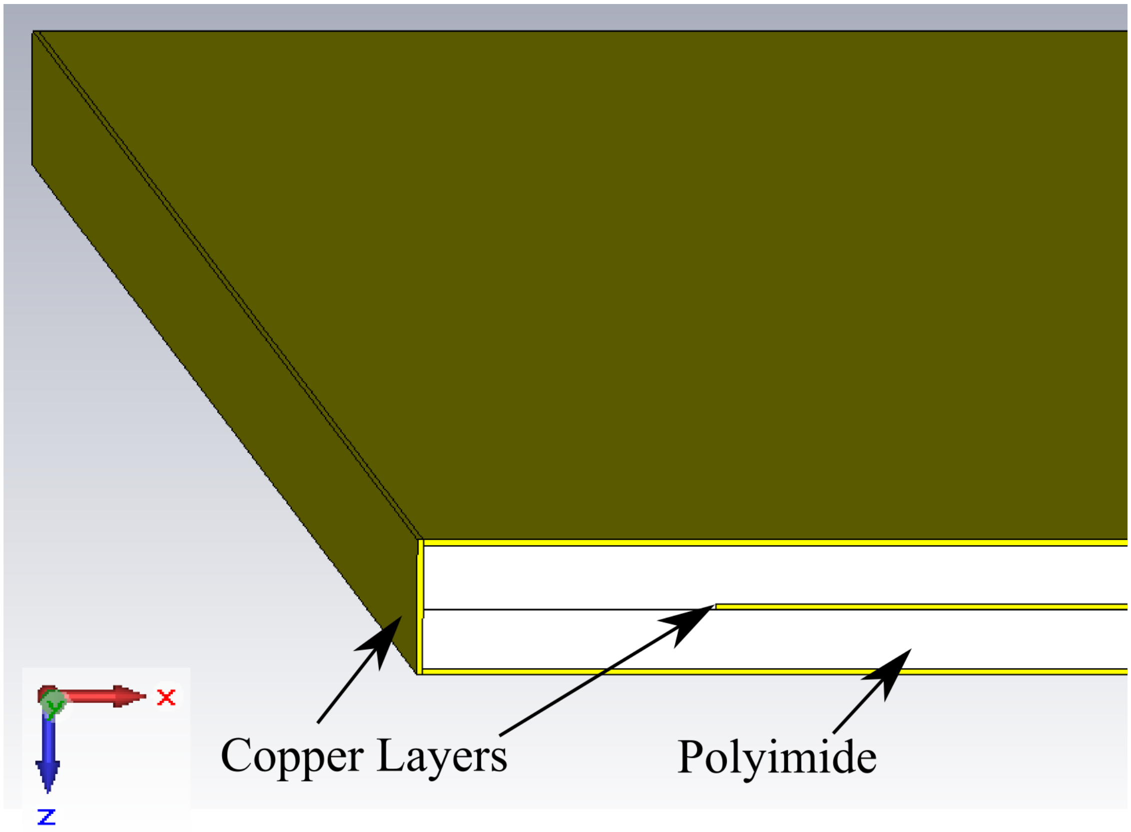

Figure 6.2: The shorted end of the simulated Blumlein.

change from the positive to negative polarity of the voltage indicates that the Blumlein configuration is more sensitive to timing issues when used to accelerate particles, as small timing offsets would create a large difference in the energy imparted to the particles.

Figure 6.5 shows the absolute value of the electric field in the XZ cutplane during the pulse at the shorted end of the Blumlein. The conductor that wraps around the end of the line contains the fields which then reflect back up the line. This is in contrast to the triggering end of the transmission line, from which large fields are generated. While the transmission lines create a pulse better suited to particle acceleration, in applications where the rest of the accelerator housing is susceptible to damage from high electric fields, the Blumlein configuration could be useful.

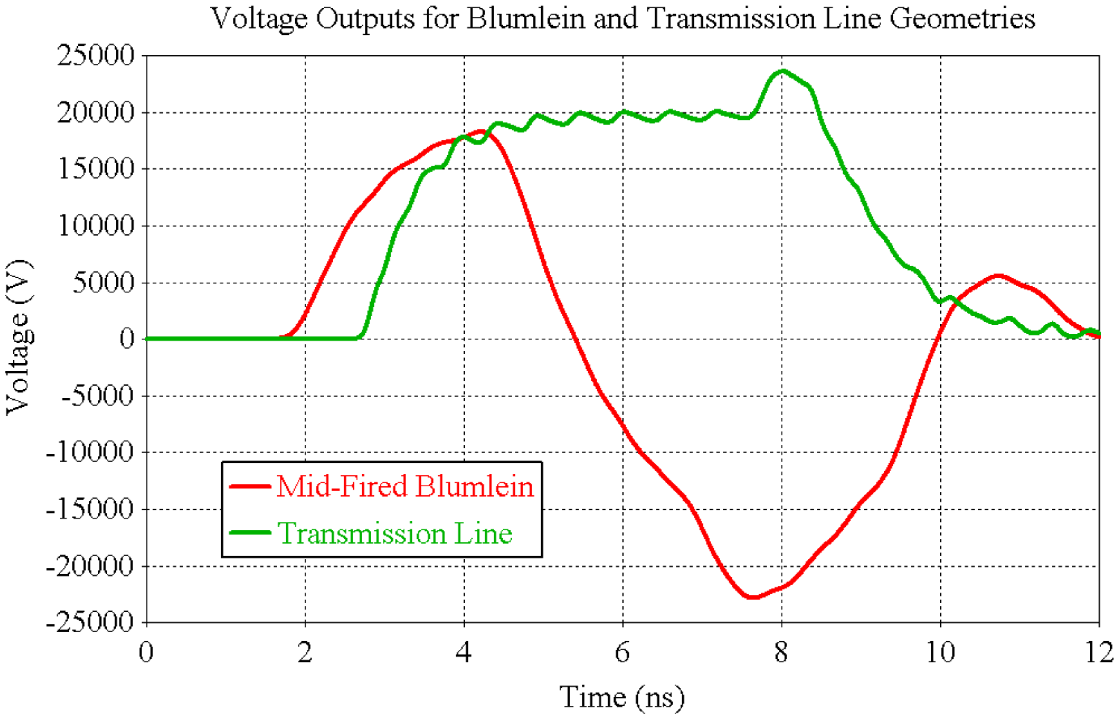

Figure 6.3: Voltage outputs for the Blumlein and transmission line geometries.

### 6.1.2 Zero Integral Pulse (ZIP) Line

Another transmission line variant is the zero integral pulse (ZIP) line. This geometry consists of additional layers of insulating material above and below the line, over which a conductive layer is wrapped around (Figure 6.6). The additional layers create an impedance of half that of the main transmission line segments of the geometry, with a thickness of half of the central insulating layers in accordance with the linear dependence of impedance on thickness shown in Equation 2.3. The purpose of these additional layers is to reduce the parasitic coupling between stacks of lines by essentially closing the field lines as they wrap around the lateral edges of the geometry [79]. The shorted end of the line also prevents the fields from propagating from the non-beam end of the line, similar to the Blumlein geometry.

A ZIP line geometry comparable to the benchmark transmission line was modeled, utilizing copper and polyimide as conductor and insulator materials, respectively. The thickness of the larger insulators was 1 mm to agree with existing simulations, while the thinner lines

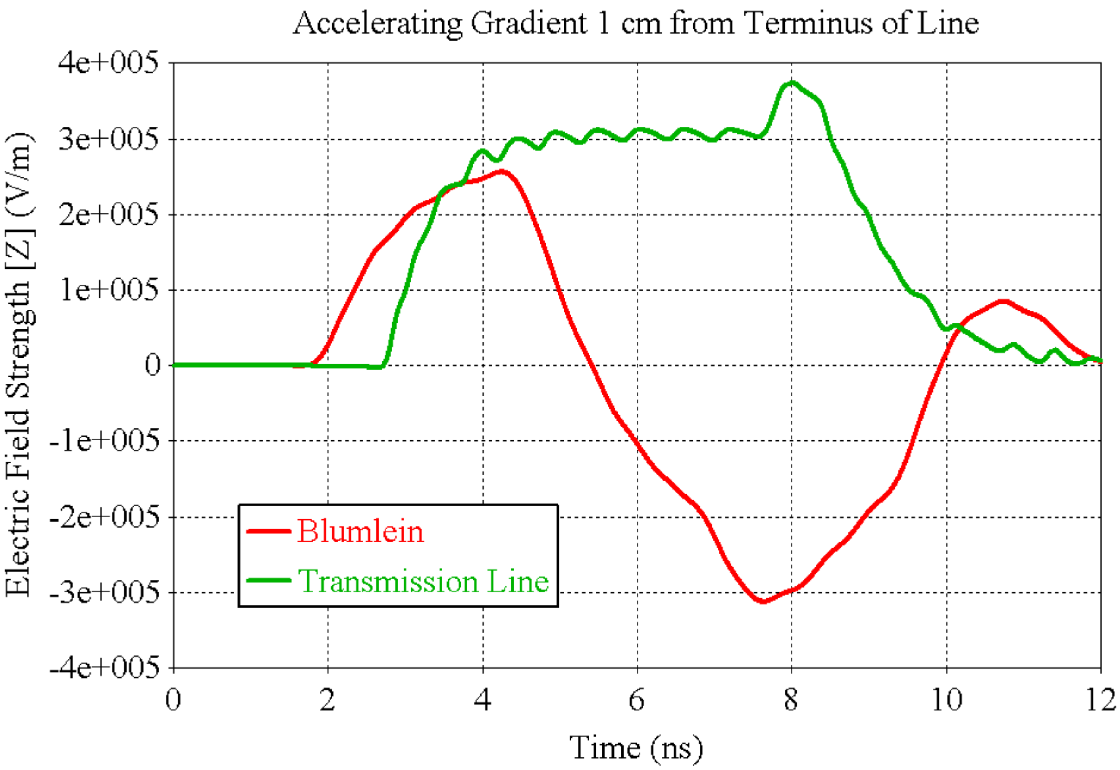

Figure 6.4: Accelerating gradients produced 1 cm from the end of the Blumlein and transmission line geometries. As in the standard transmission line case, the gradient pulse shape is seen to be very similar to the voltage output pulse shape.

were given a thickness of 0.5 mm. The thickness of all the copper layers was set to 0.1 mm. The length of the line was 40 cm, with an additional length of 5 mm at the shorted end of the line where the sub-lines meet. The ZIP line was excited with a 0.5 ns smooth step excitation of 10 kV.

Figure 6.7 shows the voltage output of the ZIP line compared to a standard transmission line and Blumlein of analogous geometries. The polarity of the ZIP line output has been flipped (instead, representing an excitation of -10 kV), as it is the negative secondary pulse that exhibits the voltage doubling effect on the voltage input. The magnitude of voltage output of the secondary pulse is roughly equivalent to that of a standard transmission line. However, the total thickness of the line is larger than that of the other geometries, and the dashed curve represents a pulse scaled down by 34.3% to account for the additional thickness of the line, since the additional layers, shorted at the beam end of the line, do not contribute

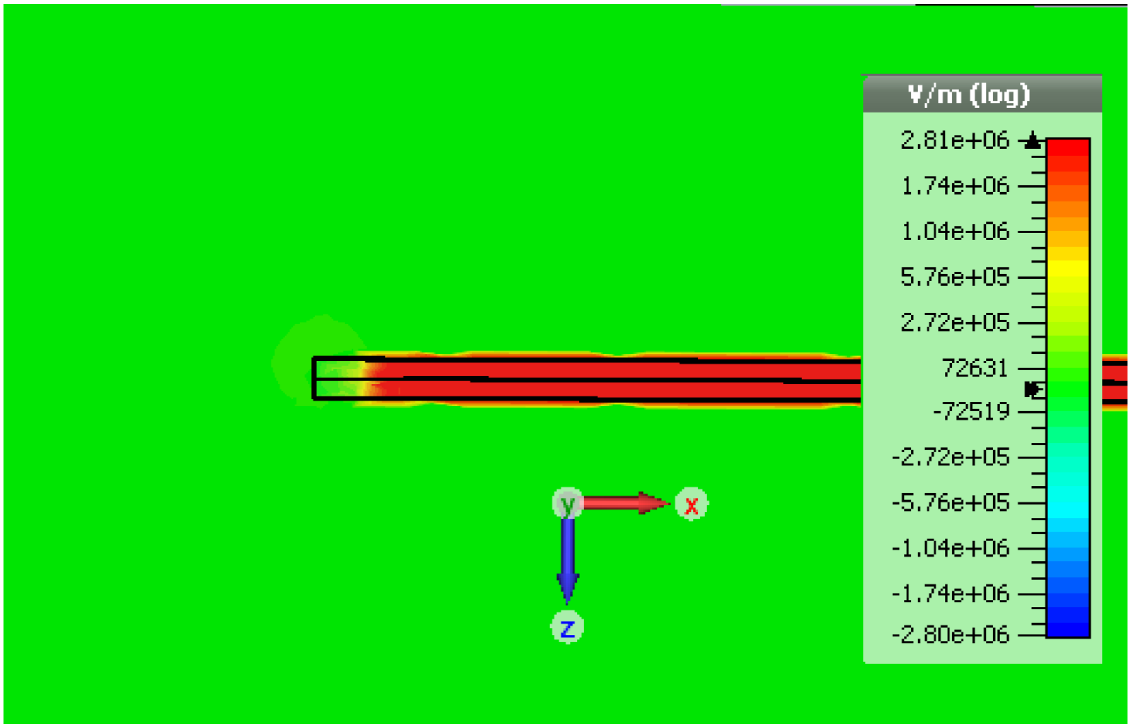

Figure 6.5: Absolute value of the electric field generated at the shorted end of the Blumlein. Note that the fields are contained within the extent of the line.

to the gradient. This loss in gradient per unit length is ultimately comparable to the parasitic losses (described in Chapter 4) that the ZIP line geometry was designed to prevent.

### 6.1.3 Radial Transmission Line

Another embodiment of the DWA could utilize radial transmission lines rather than the the rectangular plate type geometries described until now [80, 81]. Work has been published in the literature on utilizing a radial transmission line geometry excited by several pulser-type voltage inputs [8]. A model of one manifestation of a radial transmission line (used for later simulations in this section) may be seen in Figure 6.8. The benefits of a radial transmission line are that they do not exhibit the line-to-line stacked parasitic effect, as the geometry does not have any lateral edges for the fields to wrap around. An additional benefit is transverse field uniformity. Since the pulsers are located symmetrically around the beam axis, transverse off-axis fields are mostly canceled out.

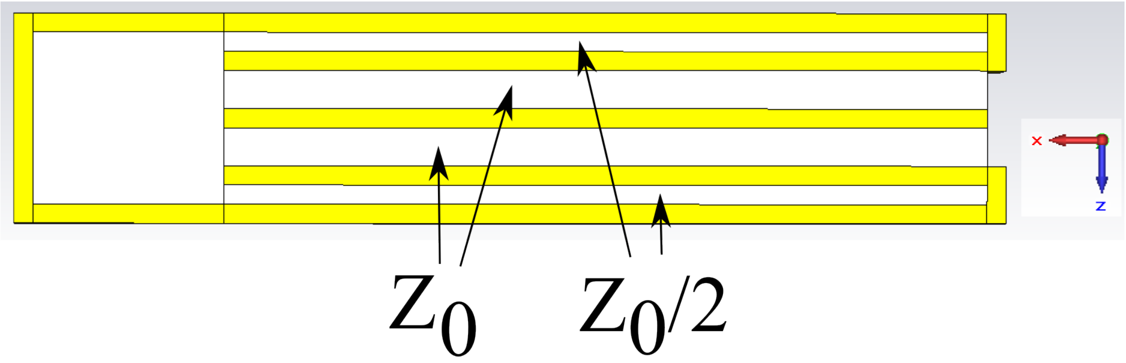

Figure 6.6: A schematic representation of a zero integral pulse (ZIP) line (thickness and length not to scale).

Radial transmission lines have very low impedance and may be constructed to be thicker than the transmission lines previously described. A model of a 1.5 cm thick radial transmission line filled with an insulator of dielectric constant 2.33 was excited by 36 pulser inputs evenly distributed along the outer edge of the line. The inner and outer radii of the line were 1.5 cm and 31 cm, respectively. The pulser type excitation signal (Figure 6.9) possessed a rise time of 200 ps, hold time of 1 ns, fall time of 300 ps, and amplitude of 60 kV. For comparison, a 1.33 cm stack of six matched transmission lines (12 total lines) utilizing the benchmark geometry described in Section 3.1.1 was modeled and excited using identical pulsed inputs on each line, for a total of 12 voltage ports. The lines were separated by 3 cm to agree with the 3 cm diameter inner radius of the radial geometry.

The peak gradients produced at the center of the radial transmission line are shown in Figure 6.10. The peak gradients produced are similar, despite the transmission line stack using more than a factor of 3 fewer pulsers per unit length. The pulse width of the transmission line case is much wider with a pulse width at 90% peak gradient of about a nanosecond, versus a few hundred picoseconds for the pulser case. However, when stacked in larger heights, parasitic effects will reduce the output somewhat, while the radial transmission line is immune to these effects.

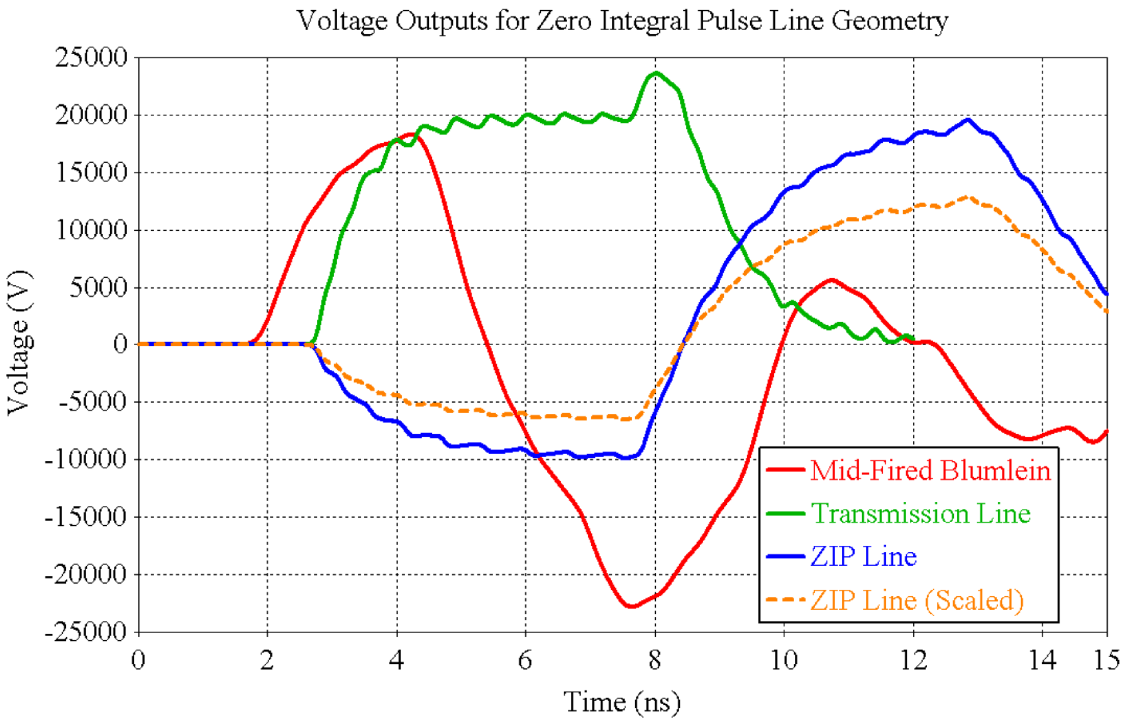

Figure 6.7: Voltage output for a ZIP line, along with those of standard transmission line and Blumlein geometries. The outputs of the ZIP line have been flipped so that the larger pulse is on the positive axis; the actual injection voltage would be -10 kV to produce this pulse. The dashed curve represents the a scaling of the measured voltage output by 65.7% to account for the added thickness of the line.

## 6.2 Methods of Pulse Shaping

One goal of geometry variation is shaping the temporal properties of the pulse. A temporal pulse shape with a gradient that increases in time (Figure 6.11), in a ramp-like shape, has certain beneficial properties. Since a particle bunch has a finite bunch size and energy spread, lagging particles undergo a higher gradient than earlier particles as the pulse increases in time. This may result in more efficient bunching and reduced energy spread. Various methods of pulse shaping are presented below.

### 6.2.1 Multiple Time-staggered Transmission Lines

One method of pulse shaping is by abutting multiple transmission lines of different lengths against the dielectric beam pipe. By choosing the triggering times appropriately, it is possible

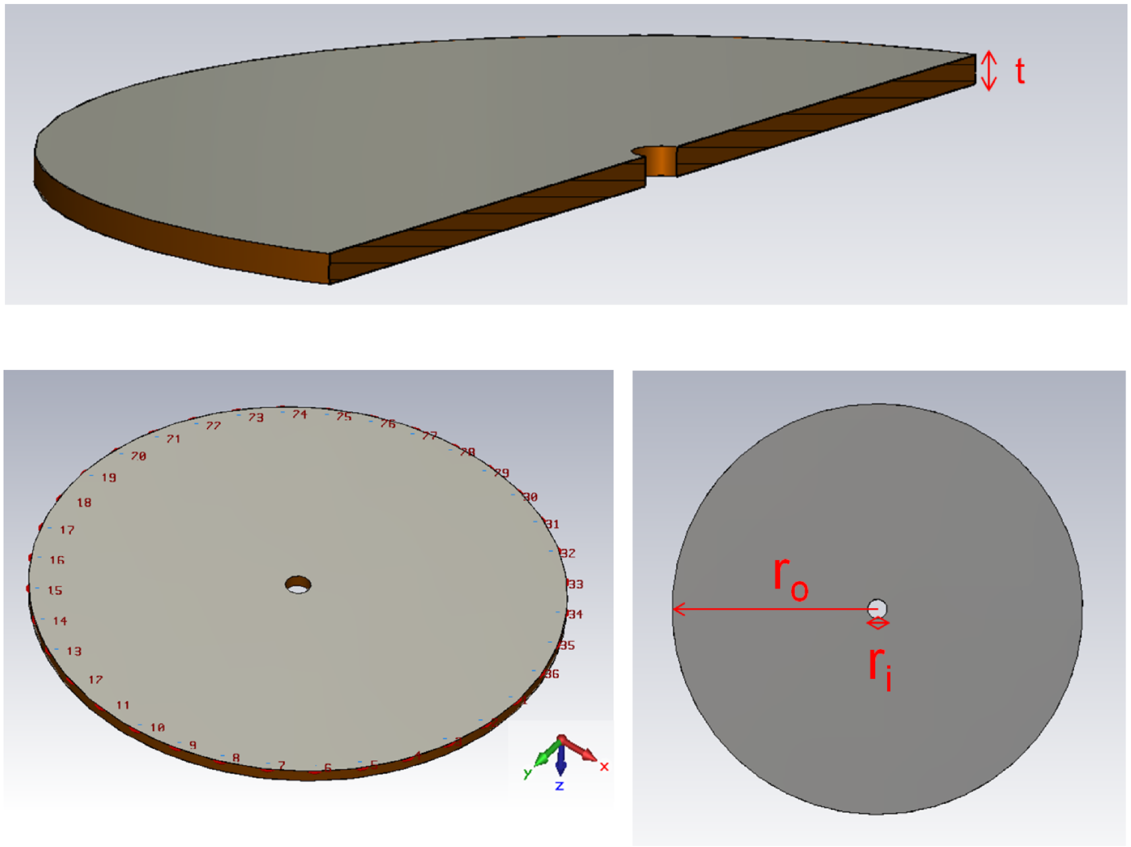

Figure 6.8: A schematic representation of a radial transmission line. The line is excited by multiple ports around the edges of the line.

to create pulses with discrete regions corresponding to the arrival times - for example, a stairstep shaped pulse. Figure 6.12 shows a geometry modeled in the Xfdtd (Remcom, Inc.) software package. The line lengths were chosen to be 2/3 and 1/3 of the reference length of 27 cm with switching times of each line corresponding to their lengths such that a stairstep shaped pulse is created, as enumerated in Table 6.1. The lines were charged by an arbitrary reference voltage and discharged by a closing switch. The expected and simulated output of the multiple line system is shown in Figure 6.13, showing good agreement.

The drawback to this configuration is the additional space required around the beam pipe, so a similar configuration was constructed with five matched transmission lines of various lengths abutted against the beam pipe in a more planar geometry (Figure 6.14 A), reminiscent of concept drawings of a DWA for proton therapy [27]. Line timings were chosen,

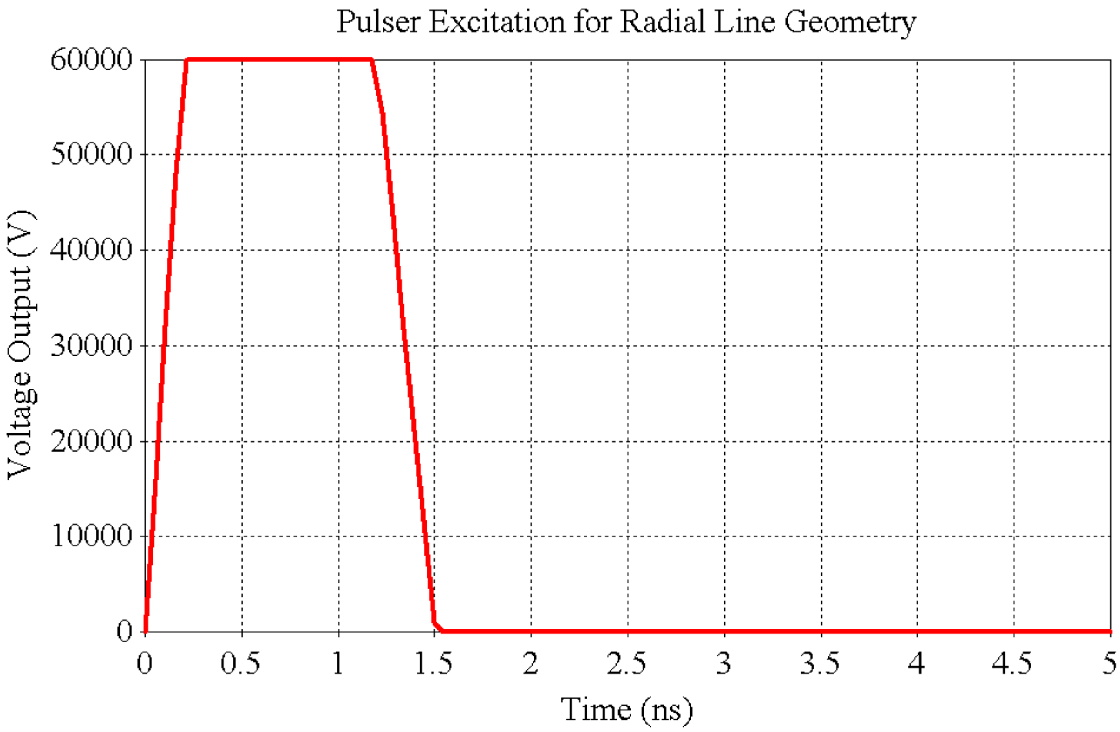

Figure 6.9: The pulsed voltage signal used to excite the radial transmission line.

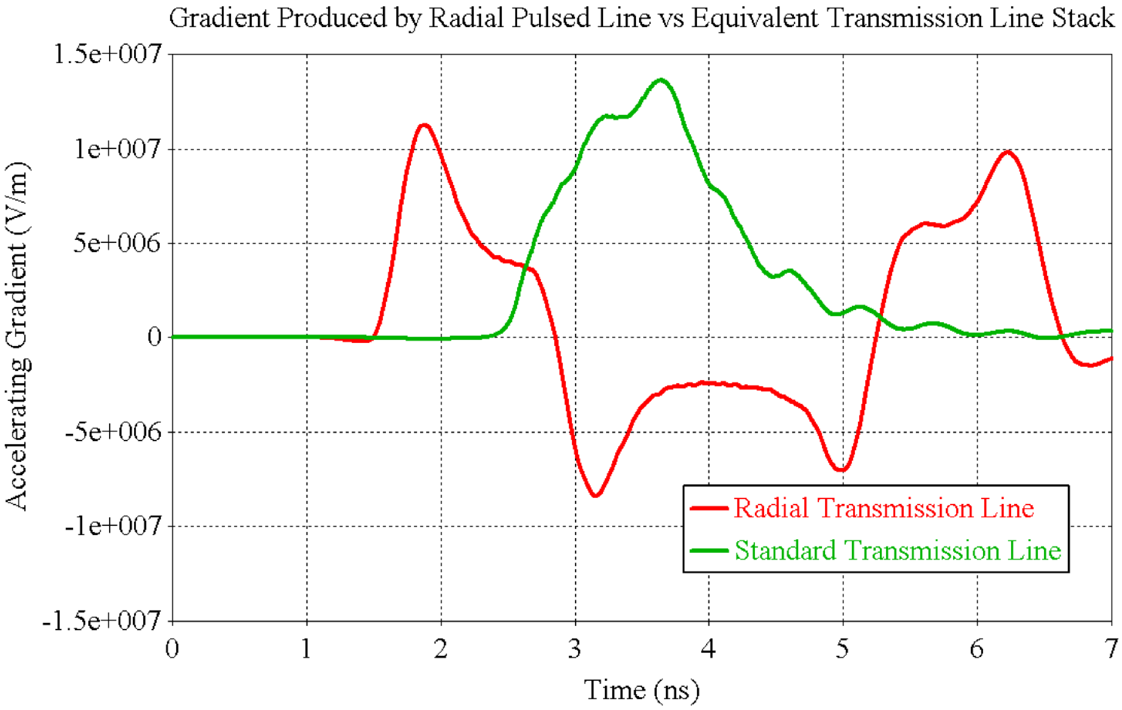

Figure 6.10: Accelerating gradient produced at the center of the radial transmission line geometry and that of an equivalent transmission line stack.

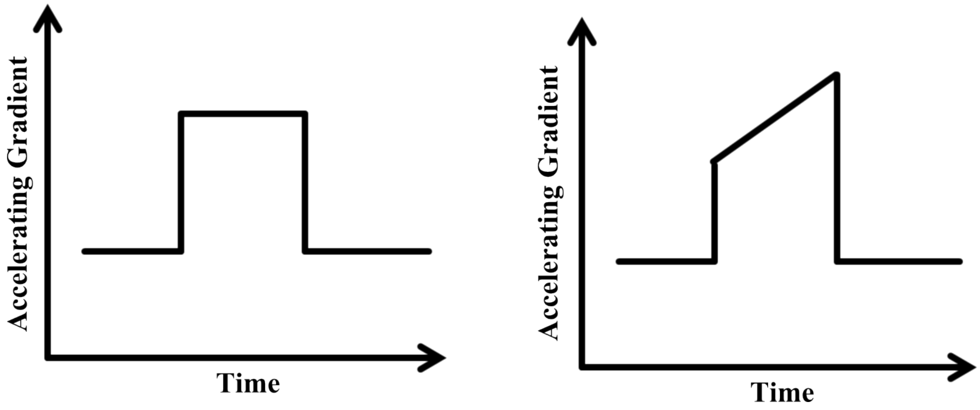

Figure 6.11: Simple schematic of a desireable, ramp shaped pulse.

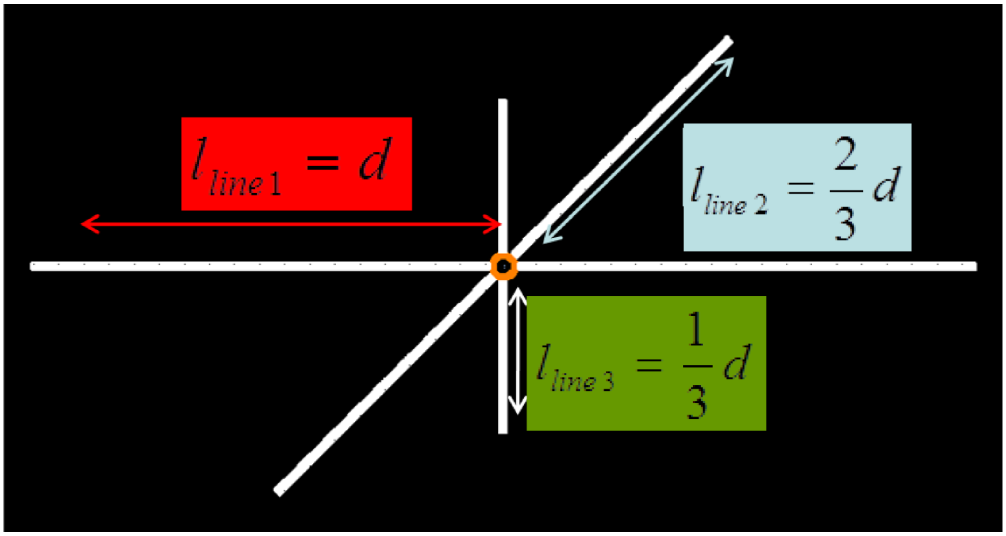

Figure 6.12: Multiple staggered transmission line geometry.

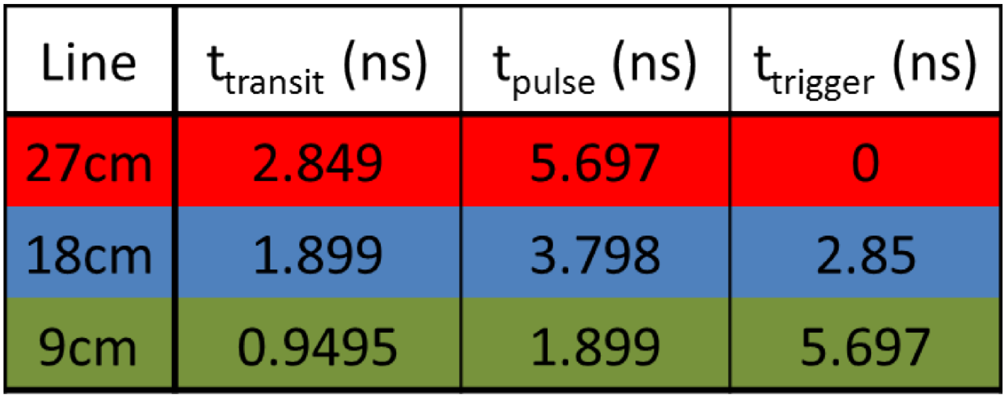

| Line | $t_{transit}$ (ns) | $t_{pulse}$ (ns) | $t_{trigger}$ (ns) |
|---|---|---|---|
| 27cm | 2.849 | 5.697 | 0 |
| 18cm | 1.899 | 3.798 | 2.85 |
| 9cm | 0.9495 | 1.899 | 5.697 |

Table 6.1: Timing values used in staggered line geometry.

Figure 6.13: Expected (top) and simulated (bottom) accelerating gradient for the staggered line geometry.

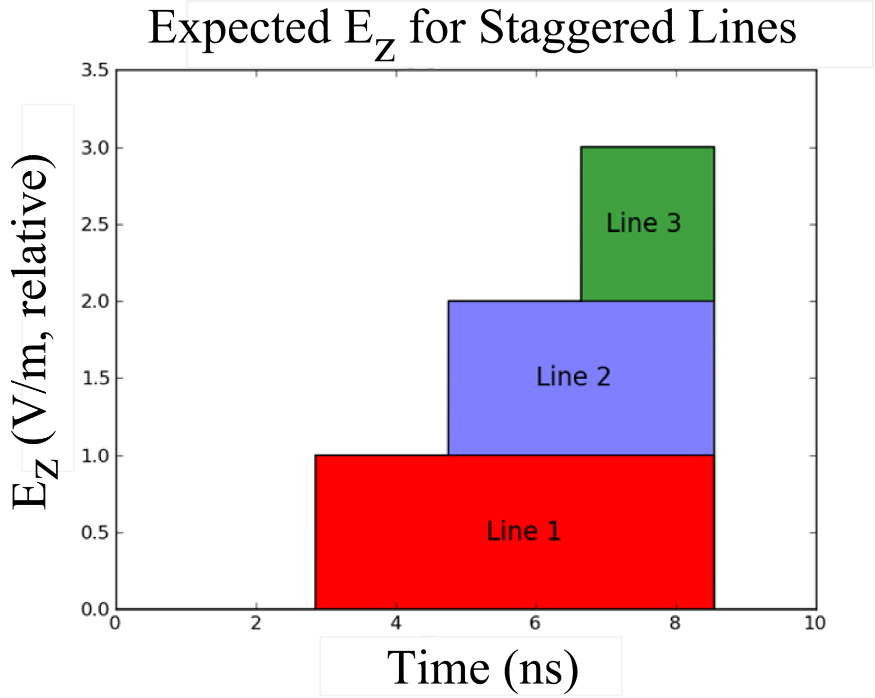

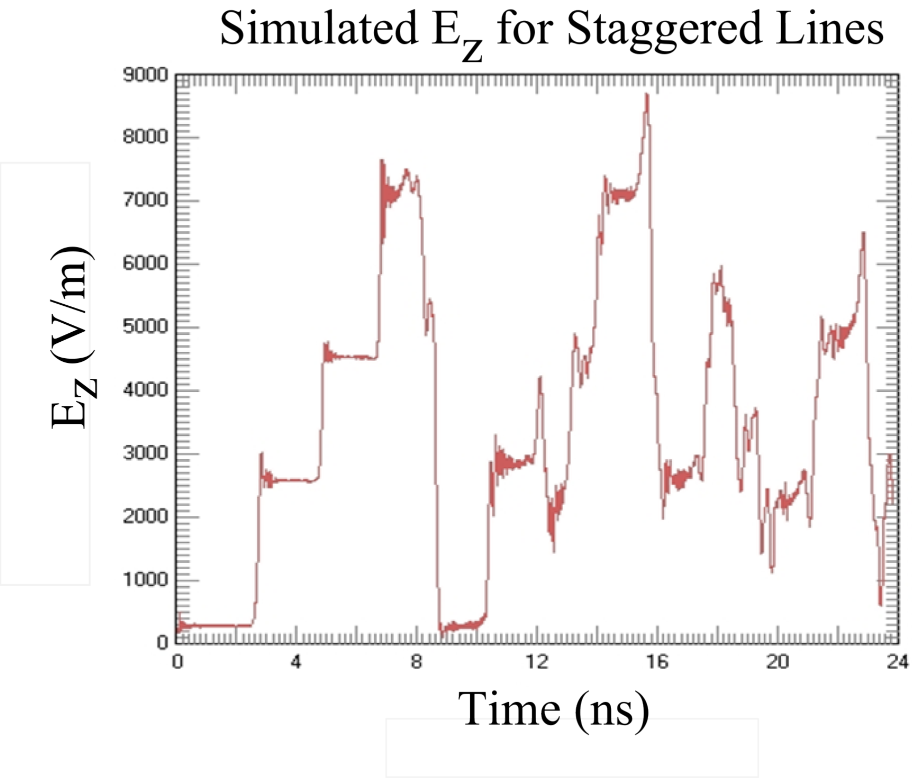

as above, to create a stairstep shaped pulse. The simulated output of this configuration, along with the output of a single line pair that is much wider than the beam pipe and charged with the same voltage, are shown in Figures 6.14 C and D. As can be seen in the figure, this staggered geometry succeeds at shaping the pulse in the discrete, stairstep fashion at the cost of the total integrated field strength. There is, however, a significant drawback - the integrated pulse of the staggered line geometry is significantly lower than that of a single line, making this configuration considerably less efficient for particle acceleration.

### 6.2.2 Dielectric Constant Variation

By constructing the transmission line of insulators with various dielectric constants, you create regions of differing impedance within the line. The internal reflections generated at an interface of the dielectrics create a build up of pulses, as every second reflection creates a wave that propagates in the proper direction (towards the beam pipe). Essentially, the effective length of the line is longer for portions of the pulse undergoing increasing numbers of reflections. As these different portions of the pulse reach the end of the line, they add to the effective gradient, creating a ramp shaped pulse. An early proof of concept simulation of this approach is shown in Figure 6.15.

The drawback to this method is the manufacture of these dielectrics. Each dielectric must be well coupled to adjacent layers, as field enhancement effects at the interfaces due to small voids may create a triple point, lowing the effective dielectric strength. This could be accomplished by methods such as suspending varying concentrations of nanobeads within a single dielectric [82, 79], though the manufacturing process may be difficult, and these materials must still be capable of holding off extremely high electric fields. Another approach would be to continuously vary the dielectric constant, though this would be even harder to manufacture. For these reasons, further investigations of this method were not performed.

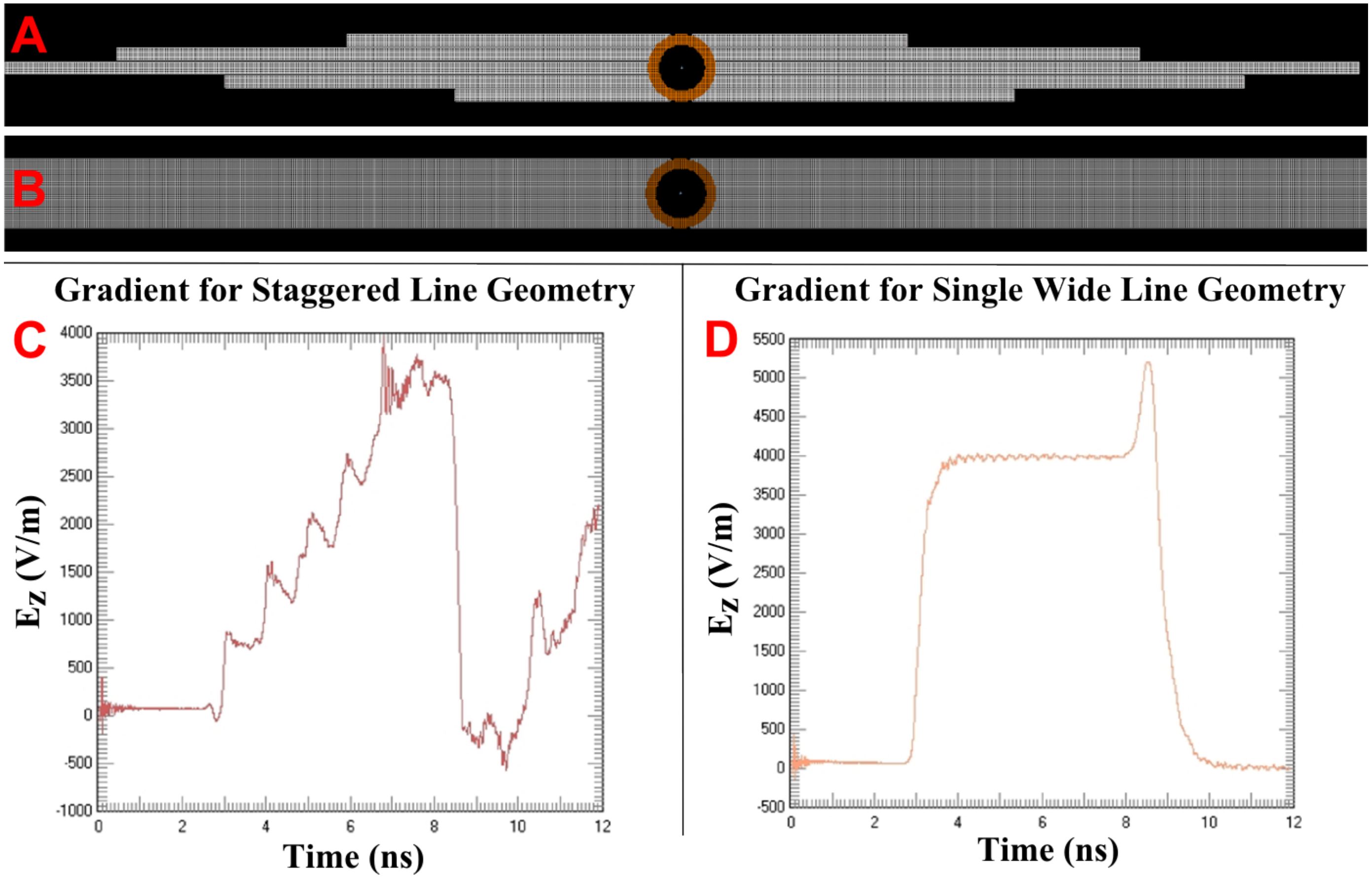

Figure 6.14: A) Geometry of the staggered DWA style geometry. B) Geometry of the reference line geometry. C) Gradient generated by the staggered DWA geometry. D) Gradient generated by the reference line geometry.

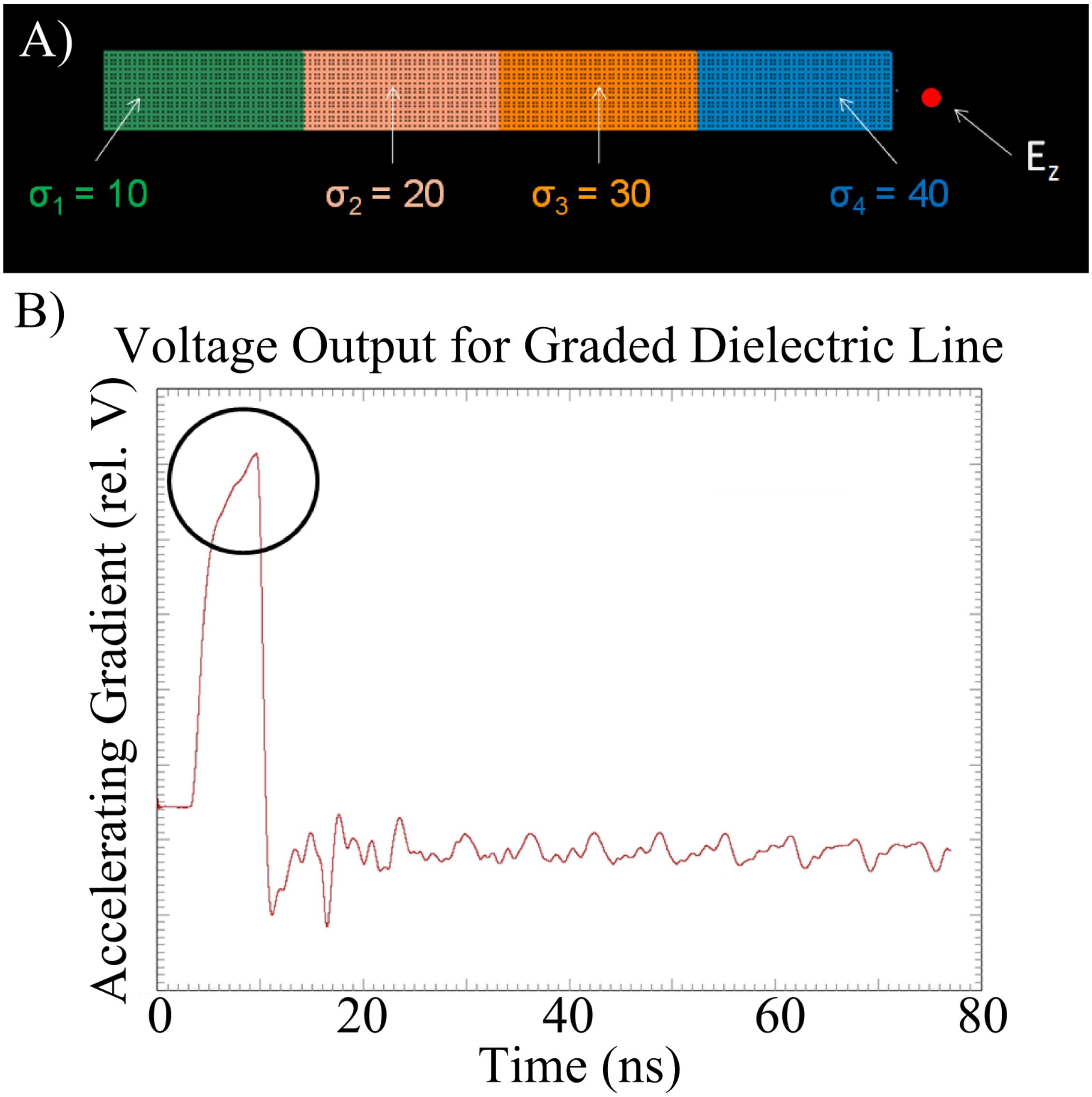

Figure 6.15: (A) Geometry of a graded dielectric transmission line with dielectric constants increasing further from the switching side. (B) Voltage output of a graded dielectric transmission line. This line was terminated with a resistance equal to the characteristic impedance of the line using the average value of the dielectric constant, causing the dampening of pulse reflections.

### 6.2.3 Widened Lines

Another possible method of pulse shaping is by widening the line laterally, along the longer side of the transmission line [83]. Similar to the dielectric constant variation above, the effective path length of the propagating fields is longer for some portions of the voltage pulse, again creating a ramp shaped pulse.

A stack of ten of these widened transmission lines was modeled using a base width $W$ of 10 cm and extra width $W_e$ of 7.5 cm (see Figure 6.16). The thickness of each insulator was 0.5 mm, while the conductors were 0.1 mm thick, giving a total stack thickness of 1.21 cm. The insulator was chosen to be a generic material with a dielectric constant of 10, while the conductor was defined as PEC. A pure insulator beam pipe with a length extending 7 cm above and below the line, outer radius of 1 cm (abutting against the line ends), inner radius of 0.8 cm, and dielectric constant of 10 was incorporated. The line was excited with a 0.5 ns smooth step voltage pulse at 20 keV. A particle source with identical parameters to that defined in Section 5.2.2 was used to inject protons at 2 MeV. An identical model with an extra width of 0 (corresponding to a standard transmission line) was simulated for comparison.

The gradients produced by the widened and standard line geometries are shown in Figure 6.17. The widened lines produce a peak gradient of 17 MeV/m, compared to the 16 MeV/m produced by the standard line, which is a gain of 6.25%. The pulse has a relatively linear ramp shaped voltage increase across its duration, rising at about 1.25 $\frac{MeV}{m \cdot ns}$. The impact of these differences in gradient on the accelerated particle bunch is shown in Figure 6.18. The energy spread, here defined as the difference between the fastest and slowest particles, is 7.4 keV for the standard line vs. 4 keV for the widened line, a reduction of 46%. The average energy gain of the widened line stack was 176 keV vs. 170 keV for the standard stack, a gain of 3.5%. Thus, this geometry, utilizing a temporally ramp shaped gradient, has been demonstrated to significantly reduce the energy spread of accelerated particles while also modestly increasing the energy gain per unit length.

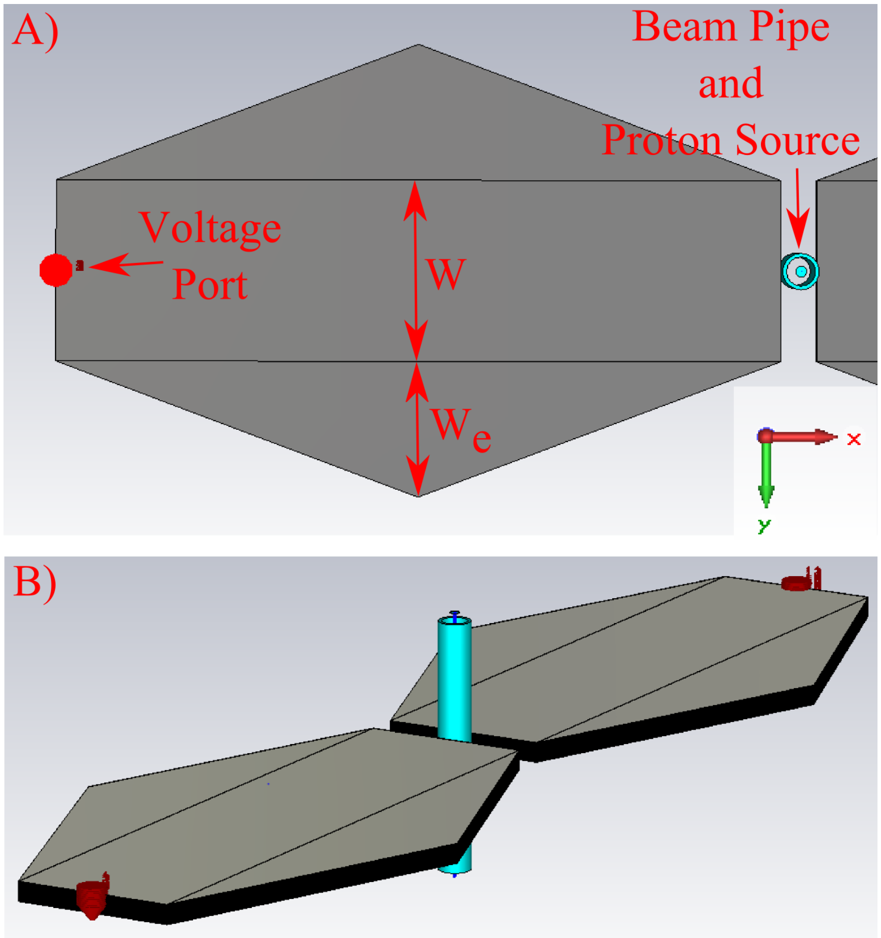

Figure 6.16: A) Top down view of the widened line geometry, with $W_e$ indicating the additional width of the line. B) Perspective view of the 1 cm accelerating stack of widened transmission lines.

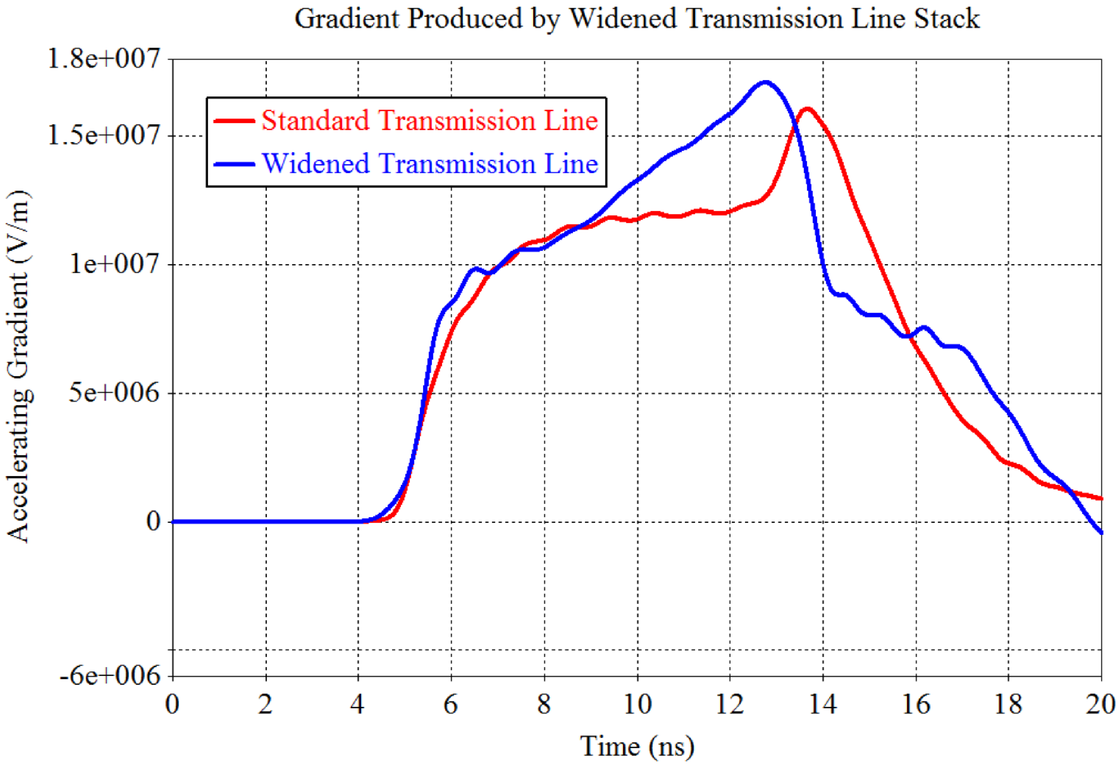

Figure 6.17: Accelerating gradients produced by the widened and standard transmission line stacks. Note the ramp shaped pulse of the widened lines.

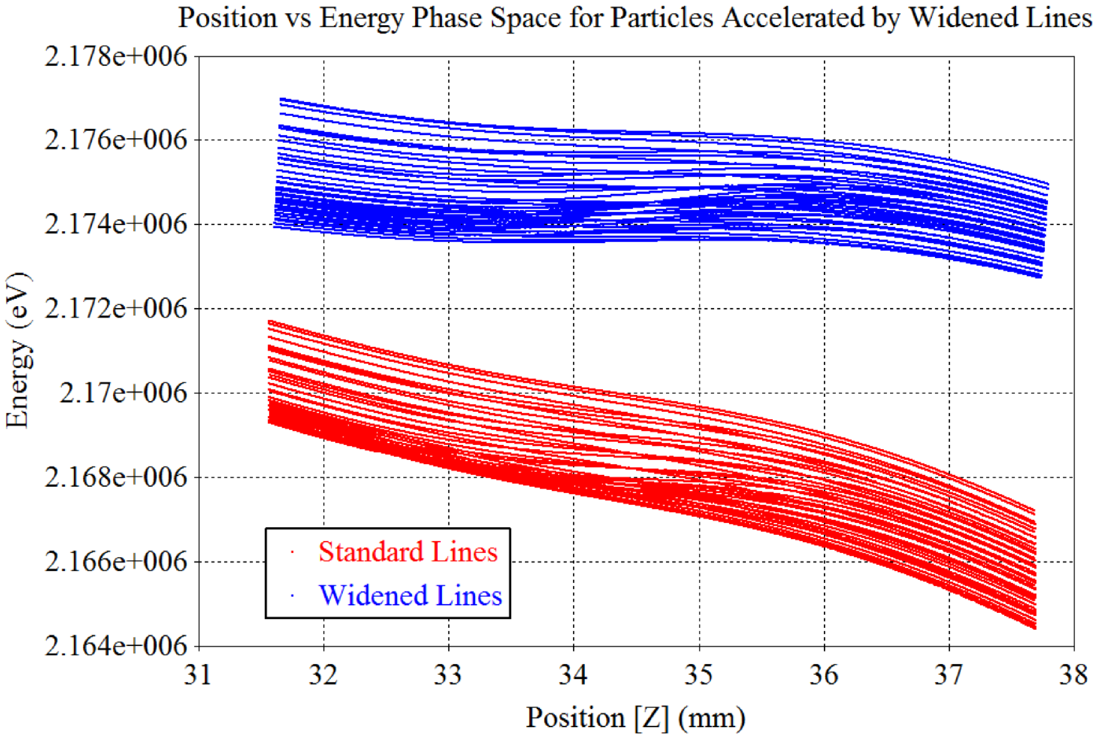

Figure 6.18: Z-position vs. energy phase space for a particle bunch accelerated by widened and standard transmission lines.

### 6.2.4 Double Matched Lines

Another attempt to increase the field at the beam axis was performed by adding a second pair of transmission lines rotated 90 degrees from the first pair (Figure 6.19). In this geometry, the width of the line determines the smallest possible gap between the lines before the lines overlap, which has a large effect on the gradient produced. To illustrate this, various line widths and corresponding gaps were modeled. All of the lines were composed of a generic insulating material with a dielectric constant of 10 and PEC, line lengths of 25 cm, insulator thicknesses of 0.5 cm, and were excited by a 0.5 ns smooth step excitation of 20 kV.

The gradients produced by a doubled pair of matched lines, in comparison with a single pair of lines separated by 1.5 cm and of width much larger than the gap (8 cm), are shown in Figure 6.20. There is a drastic reduction in gradient produced when the larger set of four lines is used, due to the large gap between the lines. The set of four lines with the smaller gap, however, creates a gradient slightly higher than that of the single line pair, with a fast rise time on the pulse due to the narrower line widths. This geometry takes up considerably more space than the single line pair and uses twice as many switches; however, in applications where space is not an issue and a steep rise time is needed, this doubly matched line geometry could have utility.

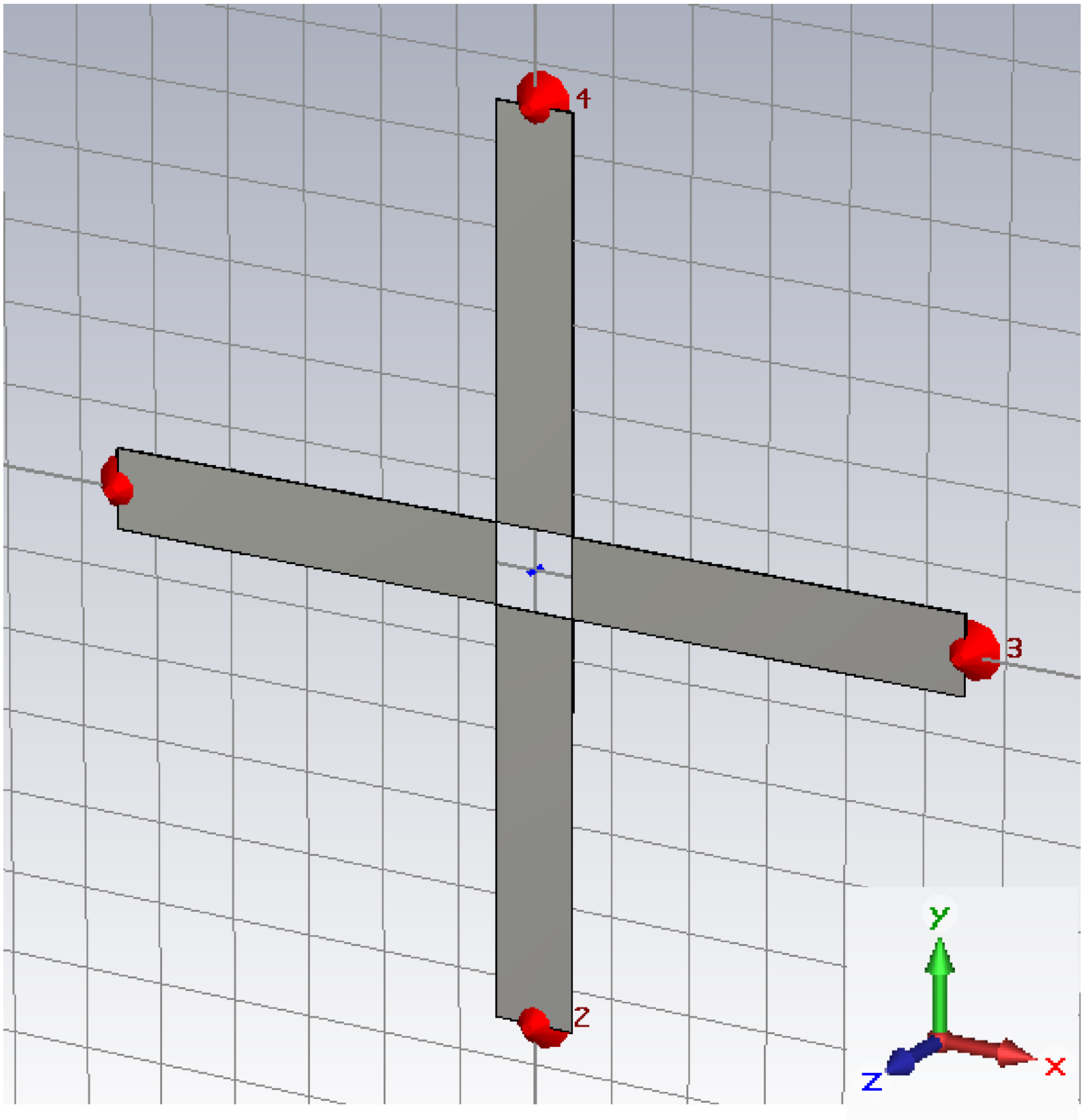

Figure 6.19: Perspective view of a double matched line geometry. The gap between the line ends at the center is determined by their width.

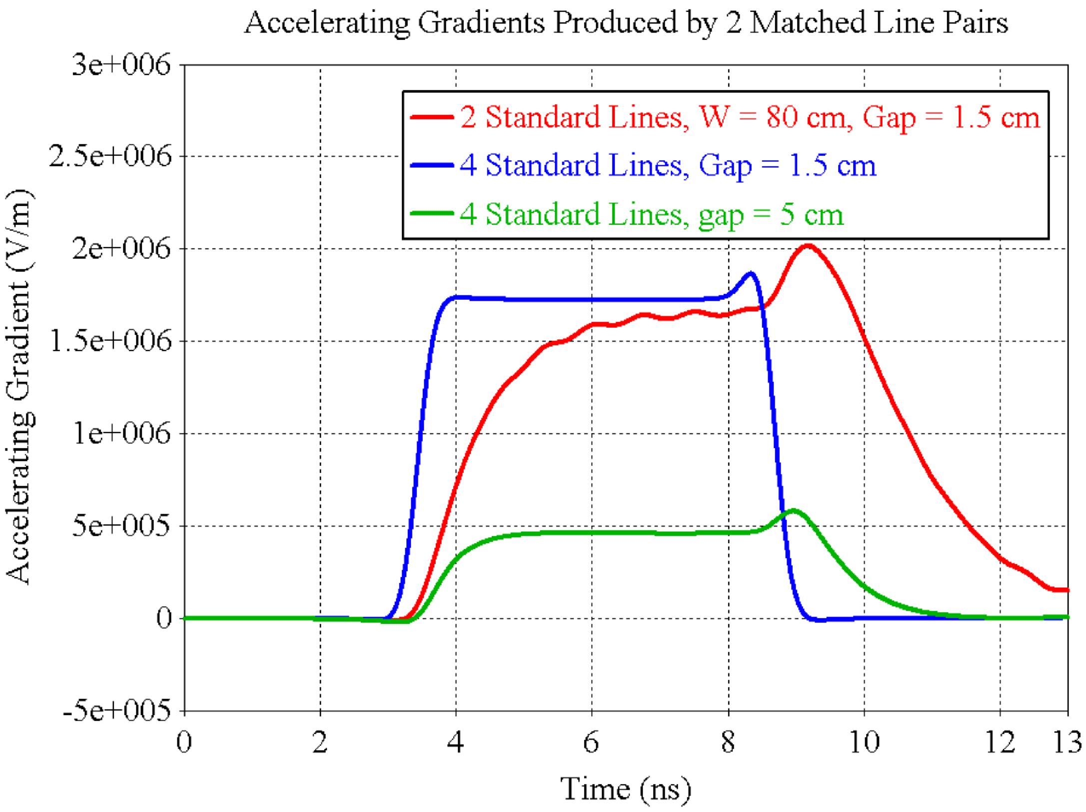

Figure 6.20: Accelerating gradients produced by doubly matched lines of differing widths (and resultant gaps).

# Chapter 7

# Conclusions and Future Work

## 7.1 Conclusions

The goal of this work was to well characterize the various components of the dielectric wall accelerator and the numerous geometric and electrical variations of the architecture. A further goal was to develop and evaluate novel variations of the structure in order to improve performance of the device. This was performed through a broad simulation study of the various components of the device; in particular, the transmission line and power sections.

In Chapter 2, the basic components of the DWA architecture were described. Equations governing the behavior of transmission lines were defined for reference throughout the rest of the study. A review of the current published work on various components of the DWA was given, followed by descriptions of existing and forthcoming prototypes. Limitations of current architectures were outlined, including early failure of optical switches and dielectric breakdown within then HGI beam pipe. Other applications of the accelerator were introduced. Methods of transmission line triggering were discussed, including optical switching and pulsed voltage injection utilizing DSRDs. Finally, the electromagnetic simulation methods used throughout the dissertation were explained.

In Chapter 3, a simulation study of individual and matched transmission lines suitable for use in the DWA was presented. The geometric and electronic parameters of the lines were varied to determine their impact on the voltage output and gradients produced. Reference line geometries and excitations were defined for consistent use throughout much of the rest of the dissertation. An analysis of the axial fields produced by single and matched lines was performed, and an axial parasitic effect was shown - this effect later illustrated a significant effect on the behavior of accelerated particles. The HGI beam pipe was included to assess how its presence perturbs the fields, and it was found to aid in directing the fields toward the beam axis, enhancing the magnitude of the gradient. A single transmission line was built and simulated, and the veracity of the simulation method was confirmed.

In Chapter 4, the effects of stacking the transmission lines were studied. Parasitic induced voltages were quantified in stacks of five and 50 benchmark lines, and the deleterious parasitics were found to plateau beyond a certain stack height. In contrast to the parasitics, the presence of neighboring lines was found to influence the propagation of fields in free space, make the fields more forward directed toward the beam axis, and enhance the gradient, offsetting the induced parasitic voltages. Finally, a study of the off-axis transverse fields was performed in order to assess the likelihood of radial debunching, and the transverse fields were found to alternate in direction above and below a single line and a simultaneous stack. The alternating nature of the fields implied that radial beam stability should be preserved.

In Chapter 5, particle tracking studies were performed on a number of stacked geometries with both closing switch and injected voltage type excitations. A framework was developed for analyzing the behavior of particles within an accelerator structure by utilizing collected phase spaces. The feasibility of a low energy ion injection was shown in the analysis of an accelerator suitable for use in PIXE analysis, though further refinements need to be performed in order to focus and bunch a particle pulse for efficient acceleration. The efficacy of particle acceleration while using pulsers to power the transmission lines was demonstrated, with such a simulated configuration accelerating protons at a gradient of 21.7 MeV/m, with higher gradients possible with further timing optimization.

In Chapter 6, various alternate transmission line geometries were simulated, and the benefits and detriments of each were described. The advantages of using a temporally ramp shaped pulse were described, and several means of achieving such a pulse were attempted. One novel alternate geometry utilizing widened transmission lines was shown to produce a significant reduction in energy spread of an accelerated particle bunch, a modest gain in effective accelerating gradient, and no additional voltage injection requirements relative to a standard transmission line.

Ultimately, the DWA is an extremely promising accelerator architecture with significant technical hurdles yet to overcome. The major limiting factor in the current state of the design is switching, and future developments on that front are crucial for the device to reach the target gradient of 100 MeV/m. The capability of the DWA to accelerate other, heavier ions such as carbon make it a potentially very powerful and versatile tool in both radiotherapy and research. This thesis has examined the behavior of the DWA architecture in various geometries and electrical configurations in order to aid optimizing the design and maximize the gradient while maintaining a useful pulse shape for a given voltage input.

## 7.2 Future Work

The work contained in this dissertation leaves open a number of avenues of investigation. Development of the PIXE accelerator model should be continued, with near term goals including a more sophisticated low energy beam transport injection system, improved switching schedule, and powering the system with voltage pulsers. Further study of the radial transmission line geometry is warranted, as their high gradients and immunity to parasitic effects make them potentially very efficient at generating high accelerating gradients. Further investigation into the use of widened transmission lines for acceleration may be performed, including a parametric study of the effects of line widening and alternate widened line shapes (such as a curved line edge). Ultimately, once the most efficient, feasible design is determined, simulated, and optimized, a short scale prototype with a useful low-energy application (such as PIXE) may be constructed. Finally, when gradients nearing 100 MeV/m are achieved in simulation, a full scale system suitable for proton and heavy ion radiotherapy may be designed.

# Bibliography

[1] W. Levin, H. Kooy, J. Loeffler, and T. DeLaney, "Proton beam therapy," *British journal of Cancer*, vol. 93, no. 8, pp. 849–854, 2005.

[2] K. Gall, S. Rosenthal, G. Row, and M. Ahearn, "Inner gantry," Jan. 1 2013. US Patent 8,344,340.

[3] J. G. Leopold, U. Dai, Y. Finkelstein, and E. Weissman, "Optimizing the performance of flat-surface, high-gradient vacuum insulators," *Dielectrics and Electrical Insulation, IEEE Transactions on*, vol. 12, no. 3, pp. 530–536, 2005.

[4] J. Harris, R. Anaya, D. Blackfield, Y. Chen, S. Falabella, S. Hawkins, C. Holmes, A. Paul, S. Sampayan, D. Sanders, *et al.*, "Multilayer high-gradient insulators," *Dielectrics and Electrical Insulation, IEEE Transactions on*, vol. 14, no. 4, pp. 796–802, 2007.

[5] W. Nunnally, D. Sanders, S. Sampayan, and G. Caporaso, "High electric field, high current packaging of sic photo-switches," tech. rep., Lawrence Livermore National Lab., Livermore, CA (United States). Funding organisation: US Department of Energy (United States), 2005.

[6] G. Caporaso, Y. Chen, S. Sampayan, G. Akana, R. Anaya, D. Blackfield, J. Carroll, E. Cook, S. Falabella, G. Guethlein, *et al.*, "Status of the dielectric wall accelerator," in *Proc. 2009 Particle Accelerator Conf. TH3GAI02*, 2009.

[7] V. Efanov, A. Kardo-Sysoev, M. Larionov, I. Tchashnikov, P. Yarin, and A. Kriklenko, "Powerful semiconductor 80 kv nanosecond pulser," in *Pulsed Power Conference, 1997. Digest of Technical Papers. 1997 11th IEEE International*, vol. 2, pp. 985–987, IEEE, 1997.

[8] F. Arntz, A. Kardo-Sysoev, and A. Krasnykh, "Slim, short-pulse technology for high gradient induction accelerators," 2009.

[9] A. Zografos, A. Hening, V. Joshkin, K. Leung, D. Pearson, H. Pearce-Percy, M. Rougieri, Y. Parker, J. Weir, D. Blackfield, *et al.*, "Engineering prototype for a compact medical dielectric wall accelerator," in *AIP Conference Proceedings-American Institute of Physics*, vol. 1412, p. 71, 2011.

[10] J. S. Bredfeldt, *Collagen Alignment Imaging and Analysis for Breast Cancer Classification.* PhD thesis, THE UNIVERSITY OF WISCONSIN-MADISON, 2014.

[11] R. Marklein, “The finite integration technique as a general tool to compute acoustic, electromagnetic, elastodynamic, and coupled wave fields,” *Review of radio science*, vol. 2002, pp. 201–244, 1999.

[12] A. Computer Simulation Technology, *CST Microwave Studio Workflow and Solver Overview*, 2014.

[13] R. R. Wilson *et al.*, “Radiological use of fast protons,” *Radiology*, vol. 47, no. 5, pp. 487–491, 1946.

[14] W. Schlegel, T. Bortfeld, and A.-L. Grosu, *New technologies in radiation oncology.* 2006.

[15] J. Flanz and T. Bortfeld, “Evolution of technology to optimize the delivery of proton therapy: the third generation.,” in *Seminars in radiation oncology*, vol. 23, p. 142, 2013.

[16] E. Pedroni, “Pencil beam scanning,” *Proton and Charged Particle Radiotherapy*, vol. 50, p. 40, 2008.

[17] E. J. Hall, “Intensity-modulated radiation therapy, protons, and the risk of second cancers,” *International Journal of Radiation Oncology* Biology* Physics*, vol. 65, no. 1, pp. 1–7, 2006.

[18] A. Trofimov and T. Bortfeld, “Beam delivery sequencing for intensity modulated proton therapy,” *Physics in medicine and biology*, vol. 48, no. 10, p. 1321, 2003.

[19] A. Lomax, “Intensity modulation methods for proton radiotherapy,” *Physics in medicine and biology*, vol. 44, no. 1, p. 185, 1999.

[20] J. Deasy, D. Shepard, and T. Mackie, “Distal edge tracking: a proposed delivery method for conformal proton therapy using intensity modulation,” *Proceedings XIIth ICCR*, 1997.

[21] R. T. Flynn, S. R. Bowen, S. M. Bentzen, T. R. Mackie, and R. Jeraj, “Intensity-modulated x-ray (imxt) versus proton (impt) therapy for theragnostic hypoxia-based dose painting,” *Physics in medicine and biology*, vol. 53, no. 15, p. 4153, 2008.

[22] M. Steneker, A. Lomax, and U. Schneider, “Intensity modulated photon and proton therapy for the treatment of head and neck tumors,” *Radiotherapy and oncology*, vol. 80, no. 2, pp. 263–267, 2006.

[23] X. Zhang, Y. Li, X. Pan, L. Xiaoqiang, R. Mohan, R. Komaki, J. D. Cox, and J. Y. Chang, “Intensity-modulated proton therapy reduces the dose to normal tissue compared with intensity-modulated radiation therapy or passive scattering proton therapy and enables individualized radical radiotherapy for extensive stage iiib non-small-cell lung cancer: a virtual clinical study,” *International Journal of Radiation Oncology* Biology* Physics*, vol. 77, no. 2, pp. 357–366, 2010.

[24] D. C. Weber, A. V. Trofimov, T. F. Delaney, and T. Bortfeld, "A treatment planning comparison of intensity modulated photon and proton therapy for paraspinal sarcomas," *International Journal of Radiation Oncology* Biology* Physics*, vol. 58, no. 5, pp. 1596–1606, 2004.

[25] M. Jermann, "Hadron therapy patient statistics," 2013.

[26] J. Lundkvist, M. Ekman, S. R. Ericsson, B. Jönsson, and B. Glimelius, "Proton therapy of cancer: potential clinical advantages and cost-effectiveness," *Acta oncologica*, vol. 44, no. 8, pp. 850–861, 2005.

[27] G. Caporaso, T. Mackie, S. Sampayan, Y.-J. Chen, D. Blackfield, J. Harris, S. Hawkins, C. Holmes, S. Nelson, A. Paul, *et al.*, "A compact linac for intensity modulated proton therapy based on a dielectric wall accelerator," *Physica Medica*, vol. 24, no. 2, pp. 98–101, 2008.

[28] H. Owen, D. Holder, J. Alonso, and R. Mackay, "Technologies for delivery of proton and ion beams for radiotherapy," *International Journal of Modern Physics A*, 2014.

[29] E. Fourkal, J. Li, W. Xiong, A. Nahum, and C. Ma, "Intensity modulated radiation therapy using laser-accelerated protons: a monte carlo dosimetric study," *Physics in medicine and biology*, vol. 48, no. 24, p. 3977, 2003.

[30] G. Coutrakon, J. M. Slater, and A. Ghebremedhin, "Design considerations for medical proton accelerators," in *Particle Accelerator Conference, 1999. Proceedings of the 1999*, vol. 1, pp. 11–15, IEEE, 1999.

[31] I. J. Das, V. P. Moskvin, Q. Zhao, C.-W. Cheng, and P. A. Johnstone, "Proton therapy facility planning from a clinical and operational model," *Technology in cancer research & treatment*, pp. tcrt–2012, 2014.

[32] C. Bloch, P. M. Hill, K. L. Chen, A. Saito, and E. E. Klein, "Startup of the kling center for proton therapy," *AIP Conference Proceedings*, vol. 1525, no. 1, pp. 314–318, 2013.

[33] W. Nunnally, "Evaluation of matched blumlein and slow-fast blumlein systems for induction accelerator power systems," tech. rep., Lawrence Livermore National Lab., CA (US), 2002.

[34] G. M. L. Y. E. Jones and L. Young, "Microwave filters, impedance matching networks and coupling structures," *Artech House*, 1964.

[35] W. Nunnally, M. Krogh, C. Williams, F. Allen, D. Trimble, S. Sampayan, and G. Caporaso, "Investigation of vacuum insulator surface dielectric strength with nanosecond pulses," in *Pulsed Power Conference, 2003. Digest of Technical Papers. PPC-2003. 14th IEEE International*, vol. 1, pp. 301–304, IEEE, 2003.

[36] S. Sampayan, P. Vitello, M. Krogh, and J. Elizondo, "Multilayer ultra-high gradient insulator technology," in *Discharges and Electrical Insulation in Vacuum, 1998. Proceedings ISDEIV. XVIIIth International Symposium on*, vol. 2, pp. 740–743, IEEE, 1998.

[37] DuPont, “Summary of properties for kapton polyimide films,” n.d.

[38] F. Davanloo, C. B. Collins, and F. J. Agee, “High-power, repetitive-stacked blumlein pulsers commutated by a single switching element,” *Plasma Science, IEEE Transactions on*, vol. 26, no. 5, pp. 1463–1475, 1998.

[39] H. C. Miller, “Surface flashover of insulators,” *Electrical Insulation, IEEE Transactions on*, vol. 24, no. 5, pp. 765–786, 1989.

[40] J. Harris, R. Anaya, D. Blackfield, Y. Chen, S. Falabella, S. Hawkins, C. Holmes, A. Paul, S. Sampayan, D. Sanders, *et al.*, “High-gradient insulators,” in *Power Modulator Symposium, 2006. Conference Record of the 2006 Twenty-Seventh International*, pp. 55–60, IEEE, 2006.

[41] J. M. Elizondo, “Novel high voltage vacuum surface flashover insulator technology,” in *Pulsed Power Conference, 1993. Digest of Technical Papers., Ninth IEEE International*, vol. 1, p. 257, IEEE, 1993.

[42] G. J. Caporaso, S. E. Sampayan, D. M. Sanders, and J. S. Sullivan, “Optically-initiated silicon carbide high voltage switch,” Feb. 28 2012. US Patent 8,125,089.

[43] M. D. Pocha and R. L. Druce, “35-kv gaas subnanosecond photoconductive switches,” *Electron Devices, IEEE Transactions on*, vol. 37, no. 12, pp. 2486–2492, 1990.

[44] W. Nunnally and M. Mazzola, “Opportunities for employing silicon carbide in high power photo-switches,” in *Pulsed Power Conference, 2003. Digest of Technical Papers. PPC-2003. 14th IEEE International*, vol. 2, pp. 823–826, IEEE, 2003.

[45] G. M. Loubriel, F. J. Zutavern, A. G. Baca, H. Hjalmarson, T. A. Plut, W. D. Helgeson, M. W. O’Malley, M. H. Ruebush, and D. J. Brown, “Photoconductive semiconductor switches,” *Plasma Science, IEEE Transactions on*, vol. 25, no. 2, pp. 124–130, 1997.

[46] J. S. Sullivan, D. M. Sanders, S. A. Hawkins, and S. E. Sampayan, “High voltage photo switch package module,” Feb. 18 2014. US Patent 8,655,125.

[47] G. J. Caporaso, “Photoconductive switch package,” Oct. 22 2013. US Patent 8,563,957.

[48] I. Grekhov, V. Efanov, A. Kardo-Sysoev, and S. Shenderey, “Power drift step recovery diodes (dsrd),” *Solid-State Electronics*, vol. 28, no. 6, pp. 597–599, 1985.

[49] I. Grekhov, A. Kardo-Sysoev, L. Kostina, and S. Shenderey, “High-power subnanosecond switch,” *Electronics Letters*, vol. 17, no. 12, pp. 422–423, 1981.

[50] V. Kozlov, I. Smirnova, S. Moryakova, and A. Kardo-Sysoev, “New generation of drift step recovery diodes (dsrd) for subnanosecond switching and high repetition rate operation,” in *Power Modulator Symposium, 2002 and 2002 High-Voltage Workshop. Conference Record of the Twenty-Fifth International*, pp. 441–444, IEEE, 2002.

[51] I. V. Grekhov and G. A. Mesyats, "Physical basis for high-power semiconductor nanosecond opening switches," *Plasma Science, IEEE Transactions on*, vol. 28, no. 5, pp. 1540–1544, 2000.

[52] D. J. Griffiths and R. College, *Introduction to electrodynamics*, vol. 3. Prentice hall Upper Saddle River, NJ, 1999.

[53] F. Cole, P. Livdahl, F. Mills, and L. Teng, "Loma linda medical accelerator project," in *Particle Accelerator Conference, 1989. Accelerator Science and Technology., Proceedings of the 1989 IEEE*, pp. 737–741, IEEE, 1989.

[54] T. Winkelmann, R. Cee, T. Haberer, B. Naas, A. Peters, S. Scheloske, and H. I.-T. C. HIT, "Experience at the ion beam therapy center (hit) with 2 years of continuous ecr ion source operation," *Proceed. ECRIS*, vol. 8, 2008.

[55] T. Winkelmann, R. Cee, T. Haberer, B. Naas, A. Peters, and J. Schreiner, "Improvements for extending the time between maintenance periods for the heidelberg ion beam therapy center (hit) ion sourcesa)," *Review of Scientific Instruments*, vol. 85, no. 2, p. 02A951, 2014.

[56] R. Hamm, H. Pearce-Percy, D. Pearson, M. Rougieri, J. Weir, A. Zografos, G. Guethlein, S. Hawkins, S. Falabella, B. Poole, *et al.*, "A single pulse sub-nanosecond proton rfq," in *Proc. AccApp*, vol. 11, 2011.

[57] ICRU, "3 beam delivery and properties," *Journal of the ICRU*, vol. 7, no. 2, pp. 29–48, 2007.

[58] N. Christofilos, R. Hester, W. Lamb, D. Reagan, W. Sherwood, and R. Wright, "High current linear induction accelerator for electrons," *Review of Scientific Instruments*, vol. 35, no. 7, pp. 886–890, 1964.

[59] J. W. Beal, N. Christofilos, and R. Hester, "The astron linear accelerator," *Nuclear Science, IEEE Transactions on*, vol. 16, no. 3, pp. 294–298, 1969.

[60] G. J. Caporaso, "Progress in induction linacs," *arXiv preprint physics/0010011*, 2000.

[61] S. J. Mumby and J. Yuan, "Dielectric properties of fr-4 laminates as a function of thickness and the electrical frequency of the measurement," *Journal of Electronic Materials*, vol. 18, no. 2, pp. 287–292, 1989.

[62] Y. Chen, G. Guethlein, G. Caporaso, S. Sampayan, G. Akana, R. Anaya, D. Anderson, D. Blackfield, J. Carroll, E. Cook, *et al.*, "Compact proton injector and first accelerator system test for compact proton dielectric wall cancer therapy accelerator," in *PAC09 Particle Accelerator Conference Vancouver, Canada*, 2009.

[63] A. Zografos, C. Hettler, Y. Parker, M. Moyers, D. Pearson, V. Joshkin, K. Leung, F. Huang, C. Cohen-Jonathan, M. Rougieri, *et al.*, "Development of the dielectric wall accelerator," 2013.

[64] Z. Jun, Z. Huang, P. Shi-Xiang, R. Hai-Tao, X. Lian-Sheng, W. Wen-Dou, Y. Zhi-Yong, S. Yi, S. Jin-Shui, Z. Lin-Wen, *et al.*, "Beam transport design for a 1 mev prototype dielectric wall accelerator," *Chinese Physics C*, vol. 38, no. 4, p. 047001, 2014.

[65] S. Peng, H. Ren, Y. Xu, T. Zhang, J. Zhao, A. Zhang, Z. Guo, and J. Chen, "Proton injector acceptance tests for a dielectric wall accelerator (dwa): characterisation of advanced injection system of light ions (aisli)," *Nuclear Instruments and Methods in Physics Research Section A: Accelerators, Spectrometers, Detectors and Associated Equipment*, vol. 763, pp. 120–123, 2014.

[66] J. Zhu, L. Xia, Y. Shen, W. Wang, H. Zhang, Y. Liu, S. Chen, W. Wang, J. Shi, L. Zhang, *et al.*, "Preliminary study of proton beam transport in a 10 mev dielectric wall accelerator," 2012.

[67] S. Sampayan, G. Caporaso, Y. Chen, S. Falabella, G. Guethlein, J. Harris, S. Hawkins, C. Holmes, M. Krogh, S. Nelson, *et al.*, "Applications of ultra-compact accelerator technologies for homeland security," *Nuclear Instruments and Methods in Physics Research Section B: Beam Interactions with Materials and Atoms*, vol. 261, no. 1, pp. 281–285, 2007.

[68] S. A. Johansson, J. L. Campbell, and K. G. Malmqvist, *Particle-induced X-ray emission spectrometry (PIXE)*, vol. 133. John Wiley & Sons, 1995.

[69] K. S. Yee *et al.*, "Numerical solution of initial boundary value problems involving maxwells equations in isotropic media," *IEEE Trans. Antennas Propag*, vol. 14, no. 3, pp. 302–307, 1966.

[70] T. Weiland, "A discretization model for the solution of maxwell's equations for six-component fields," *Archiv Elektronik und Uebertragungstechnik*, vol. 31, pp. 116–120, 1977.

[71] M. C. T. Weiland, "Discrete electromagnetism with the finite integration technique," *Progress In Electromagnetics Research*, vol. 32, pp. 65–87, 2001.

[72] E. Ltd., "Material data sheet rexolite 1422," September 2011.

[73] DuPont, "Dupont pyralux ap-plus datasheet," 2009.

[74] I. Quantum Composers, *9530 Series Digital Delay Pulse Generator Datasheet.* Quantum Composers, Inc., 2012.

[75] L. Hector and H. Schultz, "The dielectric constant of air at radiofrequencies," *Journal of Applied Physics*, vol. 7, no. 4, pp. 133–136, 1936.

[76] D. Delle Side, L. Velardi, and V. Nassisi, "Production and acceleration of protons by titanium hydride solid disks via excimer laser ablation," *Applied Surface Science*, vol. 272, pp. 124–127, 2013.

[77] D. Cheng, R. Gough, M. Hoff, R. Keller, M. Leitner, K. Leung, J. Staples, and M. Williams, "Design of the prototype low energy beam transport line for the spallation neutron source," in *Particle Accelerator Conference, 1999. Proceedings of the 1999*, vol. 3, pp. 1958–1960, IEEE, 1999.

[78] A. Haddad and D. F. Warne, *Advances in high voltage engineering*, vol. 40. IET, 2004.

[79] G. J. Caporaso, S. Sampayan, Y.-J. Chen, D. Blackfield, J. Harris, S. Hawkins, C. Holmes, M. Krogh, S. Nelson, W. Nunnally, *et al.*, "High gradient induction accelerator," in *Particle Accelerator Conference, 2007. PAC. IEEE*, pp. 857–861, IEEE, 2007.

[80] G. J. Caporaso, Y.-J. Chen, and S. E. Sampayan, "The dielectric wall accelerator," *Reviews of Accelerator Science and Technology*, vol. 2, no. 01, pp. 253–263, 2009.

[81] G. J. Caporaso, H. C. Kirbie, and S. E. Sampayan, "Dielectric-wall linear accelerator with a high voltage fast rise time switch that includes a pair of electrodes between which are laminated alternating layers of isolated conductors and insulators," Oct. 13 1998. US Patent 5,821,705.

[82] D. Sanders, E. Cook, R. Anaya, L. Wang, S. Sampayan, G. Caporaso, K. Slenes, J. Jacquin, and R. De La Fuente, "Breakdown performance statistics of a nanoparticle composite system," in *Pulsed Power Conference, 2007 16th IEEE International*, vol. 2, pp. 1826–1830, IEEE, 2007.

[83] A. Uselmann and T. Mackie, "Su-et-512: Electromagnetic simulations of the dielectric wall accelerator," *Medical Physics*, vol. 41, no. 6, pp. 345–345, 2014.